KINETICS OF THE ELECTRIC DISCHARGE PUMPED OXYGEN-IODINE LASER

DISSERTATION

Matthew A. Lange, BS, MS

AFIT/DS/ENP/11-S07

DEPARTMENT OF THE AIR FORCE
AIR UNIVERSITY

AIR FORCE INSTITUTE OF TECHNOLOGY

Wright-Patterson Air Force Base, Ohio

AFIT/DS/ENP/11-S07

KINETICS OF THE ELECTRICAL DISCHARGE PUMPED OXYGEN-IODINE LASER

DISSERTATION

Presented to the Faculty
Department of Engineering Physics
Graduate School of Engineering & Management
Air Force Institute of Technology
Air University
Air Education and Training Command
In partial fulfillment of the requirements for
The degree of Doctor of Philosophy

Matthew A. Lange, BS, MS

September 2011

AFIT/DS/ENP/11-S07

KINETICS OF THE ELECTRICAL DISCHARGE PUMPED OXYGEN-IODINE LASER

Matthew A. Lange, BS, MS

Approved:

Glen P. Perram, PhD (Chairman)	Date
LTC John McClory, PhD (Member)	Date
William Bailey, PhD (Member)	Date
William Baker, PhD (Member)	Date

Accepted:

M. U. Thomas Dean, Graduate School of Engineering and Management	Date

AFIT/DS/ENP/11-S07

Abstract

A systematic study of microwave discharges at 2.45 GHz has been performed through the pressure range of sustainable electric discharges in pure oxygen flows of 2 to 10 Torr. A corresponding study of 13.56 MHz has also been performed at pressures of 2, 4, and 7 Torr. Optical emissions from $O_2(a\ ^1\Delta)$, $O_2(b\ ^1\Sigma)$, and O-atoms have been measured from the center of a μ-wave discharge. Discharge residence times from 0.1 to 5 ms have been reported, establishing that gas temperatures arrive at stationary values within the first 0.3 ms upon entering the discharge region. The $O_2(b\ ^1\Sigma)$ emissions, with a spectral resolution of 0.01 nm, have been used to measure the temperature of the gas, which typically reaches a steady-state of 1,200 K. A theoretical description of the gas heating is fit to measured temperatures, which determines that the fraction of discharge energy coupled into gas heating is 17 ± 2%. The yield of $O_2(a\ ^1\Delta)$ comes to steady-state at all pressures within 1 ms of entering the discharge region. The interpretation of the measured $O_2(a\ ^1\Delta)$ yield, using a streamlined, nearly analytic model, cast new light on the kinetics within the electric discharge. The pseudo-first order quenching rate of $O_2(a\ ^1\Delta)$ ranges from 6,000 s^{-1} for μ-wave discharges to 600 s^{-1} for radio frequency (RF) discharges, independent of gas pressure and flow rate. The slower decay rate for the RF discharge corresponds with a considerably lower ionization rate. The observations are consistent with a second order reaction channel that is dependent on both the electron and molecular oxygen ground state concentrations. Destruction of the $O_2(a\ ^1\Delta)$ state by direct impact with electrons or atomic oxygen does not adequately describe the observed behavior of $O_2(a\ ^1\Delta)$. The role of vibrationally excited ground state oxygen is explored and provides a plausible destruction mechanism.

Acknowledgements

I would first like to thank the Air Force Office of Scientific Research for funding the multi-university research initiative that was responsible for supporting this research effort, which was led by the University of Illinois at Urbana-Champaign.

A special thanks goes out to my academic advisor, Dr. Glen Perram. His depth of knowledge and experience in this and other fields continues to surprise me and serve as a guide for every "next step" in my education, especially those steps that I did not even know I needed to make.

A special thanks also goes out to Greg Pitz for being tireless and skillful in the pursuit of experimental data, as well as providing many well-thought out contributions that made data collection and processing much less painful.

I would also like to thank Dr. William Bailey, primarily for his contributions to the development of the simulations used in this work. My first version of the computer model was a far cry from the final manifestation used during my research; the development of which would not have been possible without Dr. Bailey's assistance. Secondly, I would like to thank Dr. Bailey for his willingness to take the time to go back to first principals to explain a topic, along with the deliberate and precise manner in which he effortlessly communicates physics.

Mike Ranft and Greg Smith, the main technicians for the physics laboratories, have been essential to the execution of this research. Without their assistance, I would never have been able to locate a wrench, much less order gas, chemicals, or equipment. Without the help of the technicians, research would move at a much slower pace.

Mike Ray, the glass blower, is a true artist and shows an uncanny ability to make exactly what I needed even when my explanations were less than perfect.

The members of the team at the machine shop have always produced an excellent product in a timely fashion. Special thanks to Jan, Condi, and Boston for helping me with design concepts and deadlines.

There are many family members and friends who have stood by me during my pursuit of a graduate degree. To my mother, sister, cousins, aunts, uncles, friends from GCC, friends from the O, and friends at AFIT, I couldn’t possibly mention you all, but I thank you for everything you’ve done to help me complete this journey.

Matthew A. Lange

Table of Contents

Page

List of Figures

Figure Page

List of Tables

Notation

List of Constants

h	Planck's constant
c	speed of light
h_T	thermal conductance
k_B	Boltzmann constant
k_T	thermal conductivity
l	length of discharge region
$\Delta\varepsilon_a$	transition energy for O_2(a) state
$\Delta\varepsilon_o$	transition energy for O-atom state

List of Acronyms

EOIL	electrically driven oxygen-iodine laser
COIL	chemical oxygen-iodine laser
ABL	airborne laser
SOG	singlet oxygen generator
RotoCOIL	SOG using rotating disk
UIUC	University of Illinois at Urbana-Champaign
RF	Radio frequency, oscillating electric field
EEDF	electron energy distribution function
BolSig+	Boltzmann code
HPGe	high-purity germanium, semiconductor material

List of Rates

$k_{attach}(T_e)$	rate of attachment
$k_{a+}(T_e)$	rate of excitation of a state
$k_{b+}(T_e)$	rate of excitation of b state
$k_{A+}(T_e)$	rate of excitation of A state
$k_{OP+}(T_e)$	rate of excitation of O(^{3}P) state
$k_{OD+}(T_e)$	rate of excitation of O(^{1}D) state
$k_{OS+}(T_e)$	rate of excitation of O(^{1}S) state
$k_{ion}(T_e)$	rate of ionization
$k_{a-}(T_e)$	inverse of excitation rate of a state
$k_{rec}(T_e)$	rate of recombination of electrons and positive ions
k_{wall}	rate or reaction at the wall
k_{O2x}	quenching rate of O_2(a) by O_2(X)
k_{3body}	quenching rate of O_2(a) by three-body reaction
k_{aO}	quenching rate of O_2(a) by O-atoms
k_{aO3}	quenching rate of O_2(a) by ozone
k_e^O	rate of excitation of O-atoms from the ground state to the O(^{3}P) state
k_{de}	rate of dissociation of oxygen to O-atoms one excited to the O(^{3}P) state
k_e^{Ar}	rate of excitation from Ar($1p \rightarrow 2p_1$)

List of Rates

ΣA_O	rate of radiative emission of O(^{3}S)
ΣA_{Ar}	rate of radiative emission of Ar(2p)
k_Q^O	rate of collisional relaxation of O(^{3}P) state by ground state oxygen
k_Q^{Ar}	rate of collisional relaxation of Ar(2p1) state by ground state oxygen
A_{O}	Einstein A coefficient for O-atom
A_{Ar}	Einstein A coefficient for argon
A_{ij}	Einstein A coefficient for transition ij
k_L(E/N)	coefficient relating E/N to deposited energy
k_Y	scaling term for Y_a

List of Variables

Y_a	yield of O_2(a)
$K_{eq}(T)$	equilibrium constant relating Y_a and iodine population inversion
T_g	gas temperature
T_r	rotational temperature
T_e	electron temperature
T_0	temperature at entrance to discharge
T_{ss}	steady-state gas temperature
ε_{avg}	average electron energy
ε	electron energy
f	fraction of energy coupled into the gas heating
f_ε	electron energy distribution
$f_\varepsilon(\varepsilon)$	electron energy distribution showing energy dependence
$\mathrm{E}_{\mathrm{eff}}$	effective electric field
k_{col}	collisional coefficient
ω	frequency of the field oscillations
v_g	velocity of gas flow
$v_g(t)$	time-dependent velocity of gas flow
v_{th}	thermal velocity
ν	frequency of light
$h\nu$	energy of a photon
ρ	gas density
P	pressure
P_{in}	power coupled into the discharge
ξ_{part}	energy per particle
e	the charge on the electron
m	the mass of the electron
E	the electric field
∇_v	the gradient in the velocity reference frame
$C(f)$	the rate of change due to collisions

List of Variables

σ_k	cross-sections of the collisions
N	number density of collision partners in a plasma
$\dot{n}$	flow rate
I_a	intensity of O_2(a) emissions
I_b	intensity of O_2(b) emissions
I_O	intensity of O-atom emissions
I_{Ar}	intensity of argon emissions
C_r	correction factor, including the radiometry of the detection system
C_{Ar}^{O}	number relating I_O/I_{Ar} to $[O]/[O_2(X)]$
t_r^{o}	residence time assuming constant velocity
$t_r^{'}$	pressure normalized residence time
t_r	residence time
γ_O	empirically determined coefficient used in calculation of wall rate
Γ_a	fit parameter
E/N	reduced electric field
${}^{avg}\Gamma_a$	average value of fit parameter
x_k	number density of the collision partners

List of Notations

I	iodine
I*	excited state of atomic iodine
I2	iodine molecule
Cl	chlorine
KCl	potassium chloride
O	atomic oxygen
O^-	negative ion
$[O^-]$	concentration of negative ion
$[O^-]_{ss}$	steady-state concentration of negative ion
O_2^+	positive ion
$\left[O_2^+\right]$	concentration of positive ion
$\left[O_2^+\right]_{ss}$	steady-state concentration of positive ion
O_2^-	negative ion
$\left[O_2^-\right]$	concentration of negative ion
$\left[O_2^-\right]_{ss}$	steady-state concentration of negative ion
O_2	oxygen gas
NO	molecule nitric oxide
NO_2	molecule nitric oxide
Ar	argon

List of Notations

Ar($2p_1$)	argon in excited state
$[O]$	concentration of atomic oxygen
$O_2(X)$	ground state oxygen molecule
$[O_2(X)]$	concentration of ground state oxygen molecule
$[O_2(X)]_{ss}$	steady-state concentration of ground state oxygen molecule
$O_2(a)$	excited a state of oxygen molecule
$[O_2(a)]$	concentration of excited a state of oxygen molecule
$[O_2(a)]_{ss}$	steady-state concentration of excited a state of oxygen molecule
$O_2(b)$	excited b state of oxygen molecule
$[O_2(b)]$	concentration of excited a state of oxygen molecule
$[O_2(b)]_{ss}$	steady-state concentration of excited a state of oxygen molecule
$O_2(v)$	vibrationally excited oxygen molecule
$[O_2(v)]$	concentration of vibrationally excited oxygen molecule
$[O_2(v)]_{ss}$	steady-state concentration of vibrationally excited oxygen molecule
$[O_2]_0$	concentration of oxygen species within the gas
$[e^-]$	concentration of electrons

KINETICS OF THE ELECTRICAL DISCHARGE PUMPED OXYGEN-IODINE LASER

I Introduction

The airborne laser (ABL) is a modified Boeing 747 designed to serve as a missile defense system. The weapon system carried on the ABL is a chemical oxygen-iodine laser (COIL).[1] COIL is a megawatt-class laser that employs the interaction of basic hydrogen peroxide and chlorine gas to reactively generate the first excited state of molecular oxygen, $O_2(a\ ^1\Delta)$.[1,2] The $O_2(a\ ^1\Delta)$ state is then used to collisionally excite the $I(^2P_{1/2})$ excited state of atomic iodine. It is the population inversion between the $I(^2P_{1/2})$ upper energy state and $I(^2P_{3/2})$ ground state that provides the gain in a COIL device.[2] Using a chemical reaction to generate the $O_2(a\ ^1\Delta)$ state of oxygen introduces a limit to the magazine depth of the weapon system and possesses a large logistical tail and significant safety issues associated with the exotic chemistry. In order to alleviate the shortcomings of the COIL system, an electric discharge may be used to populate the $O_2(a\ ^1\Delta)$ state.

An electrically driven oxygen-iodine laser (EOIL) has many advantages. First, it eliminates the logistic tail associated with the COIL chemistry. Second, it has an extended magazine depth. Next, it ffers closed-cycle operation. Finally, it maintains the thermal management and beam quality traits of the COIL.

The yield of $O_2(a\ ^1\Delta)$ produced by a microwave discharge was first reported in 1978 by Bernard and Pchelkin.[2] They obtained yields (the fraction of gas flow in the excited state) of 11%.[2] The $O_2(a\ ^1\Delta)$ yield, Y_a, is defined as:

$$Y_a = \frac{\left[O_2\left(a^1\Delta\right)\right]}{\left[O_2\right]_0} \tag{1.1}$$

where $\left[O_2(a\ ^1\Delta)\right]$ is the concentration of $O_2(a\ ^1\Delta)$ in the gas flow, and $\left[O_2\right]_0$ is the concentration of ground state molecular oxygen entering the discharge region. In a laser medium, there is competition between absorption and stimulated emission of photons. The excited state must reach a yield (percent of population) large enough to produce more stimulated emissions of photons than those absorbed. This yield is defined as the threshold yield. The threshold yield required for lasing in an oxygen-iodine laser is 17% at room temperature, or 293 K. Therefore, using an electric discharge as a source of $O_2(a\ ^1\Delta)$ for an oxygen-iodine laser will require the yield of the $O_2(a\ ^1\Delta)$ within the discharge to increase in order to surpass the threshold yield of the laser.

Recent research into an EOIL device has resulted in output laser powers up to 102 W.[4] In 2004, the University of Illinois at Urbana-Champaign (UIUC) demonstrated the first operation of an EOIL device.[5] In 2005, the maximum $O_2(a\ ^1\Delta)$ yield of 17% was reported without the inclusion of NO_2 in the gas flow.[3] The maximum laser power of this early laser system was 520 mW with a 400 W radio frequency (RF) discharge. In 2008, two parallel 1,000 W discharges were used, and a laser power of 12 W was measured.[4] In 2010, UIUC presented output powers of 102 W for an EOIL device, using a discharge configuration with six 3/4-inch quartz tubes.[6] For an EOIL device to be useful as a laser weapon, the output laser power must be scaled to kilowatts.

The maximum laser power of an EOIL device is constrained by the amount of $O_2(a\ ^1\Delta)$ within the gas flow over the threshold yield. In order to scale an EOIL device to higher powers, either the yield must be increased, or the number density of the gas above threshold must be increased. The number density above threshold yield may be improved by increasing the total yield or the total gas pressure, while maintaining the same yield. The overall yield of the discharge is determined by the nature of the plasma and, therefore, is difficult to change. Increasing the pressure of the oxygen flowing through an electric discharge, while maintaining $O_2(a\ ^1\Delta)$ yields above the laser threshold of 17%, has proved problematic. The pressure dependence of the yield suggests that a second-order reaction is destroying the $O_2(a\ ^1\Delta)$ excited state. Previous studies in the literature have focused primarily on increasing production of $O_2(a\ ^1\Delta)$ and not on completely understanding the destruction of $O_2(a\ ^1\Delta)$ in the discharge.[3-14]

In order to gain a better understanding of what is limiting the $O_2(a\ ^1\Delta)$ yield in the electric discharge, a systematic study is performed of a glow discharge sustained within flowing pure oxygen gas. The chemical kinetics of an EOIL system are studied in order to investigate the dominant mechanism responsible for limiting the yield of $O_2(a\ ^1\Delta)$ as pressure is increased. Studying chemical kinetics within an electric discharge is complicated because of the need to employ diagnostics that do not perturb the plasma. Typical studies used the optical emissions from excited states within the discharge to monitor the excited species populations.[3, 8,15,16] Using optical diagnostics to examine the system is complicated by the variations in gas density due to changes in the gas temperature, as well as contamination of the collected data from emissions of atomic species within the measured frequency range.

In this research, there has been an in-depth investigation of the changes in gas temperature as gas flow rates and gas pressures change, using the emissions of the $O_2(b\ ^1\Sigma)$ state. The $O_2(b\ ^1\Sigma)$ state is the second excited state of molecular oxygen, and the relative intensities of the peaks in the rotational emission spectrum are governed by Boltzmann statistics, allowing for the gas temperature to be extracted. Gas temperatures are reported in a number of studies with errors typically being 10% or higher.[3, 7, 15, 17, 18] Emission intensities are directly related to the number density of emitters, which is then directly related to the gas temperature by the ideal gas law. Uncertainty in the temperature translates directly into uncertainties in the determination of the species' concentrations. Using a high-resolution spectrometer and developing a theoretical description of the heat transfer within the gas flow, a high-precision gas temperature measurement was pursued.

Gas temperature also plays an important role in laser weapon performance. The intent of coupling energy into the gas using the discharge is to populate the $O_2(a\ ^1\Delta)$ state. If this energy is instead coupled into gas heating, it is wasted and must be removed from the gas flow. Also, heavy-heavy particle interactions are typically directly proportional to the temperature of the gas. One such interaction is the quenching of the $O_2(a\ ^1\Delta)$ state by ground state oxygen. The relationship between the excited state of oxygen and excited state of iodine, which is responsible for lasing in oxygen-iodine laser devices, is inversely affected by temperature. This will be discussed further in Section 2.1. It is important to have a precise and complete understanding of the gas temperatures within the electric discharge in order to understand the performance of an EOIL device.

After temperature-driven changes in concentration are removed from the data, the measured $O_2(a\ ^1\Delta)$ emissions may still be affected by optical emissions from other excited states created by the discharge. Within the electric discharge, other excited species are formed, such as O-atoms, and these may emit optically within the same spectral region as the molecular species, $O_2(a\ ^1\Delta)$. When observing the $O_2(a\ ^1\Delta)$ emissions, the spectral radiation from four atomic species is also gathered. The atomic species emit at 1,257 nm, 1,266 nm, 1,280 nm, and 1,299 nm and are in the same spectral region as the $O_2(a\ ^1\Delta)$ excited state, which radiates from 1,250 nm to 1,290 nm. By identifying and removing the optical contributions of the O-atom states from the measured intensities, the $O_2(a\ ^1\Delta)$ concentrations may be studied directly within the discharge. After taking care to report concentrations of emitting species accurately, a kinetic model is included in the analysis to understand the behavior of non-emitting species, such as electrons.

In order to understand the kinetic reactions within the discharge, a computer model is required. The electron density drives the reactions of all other species within the discharge; however, electrons do not have optical signatures [such as $O_2(a\ ^1\Delta)$] that would enable a measurement of their concentration. Therefore, the electron number density is determined by numerically solving the Boltzmann equation and using the results to solve a chemical kinetic package to describe the plasma. There are many computational models accepted within the community. The models include at least 50 reactions and reproduce measured results.[7, 16] However, including such a large number of kinetic pathways makes the determination of key reactions difficult. Therefore, a physically intuitive model is developed within this study that adequately describes the experimental results and gives a clear understanding of the physics involved in the system.

A physically intuitive set of kinetics is included in a computer model and used to extract the behavior of the quenching reaction responsible for limiting the $O_2(a\ ^1\Delta)$ concentration within electric discharges. The model includes the electron density, O-atom density, negative ion density, ground state oxygen density, and density of the $O_2(a\ ^1\Delta)$ excited state of molecular oxygen. This model is shown to accurately describe the discharge and gives a clear understanding of the gas phase kinetics, which is difficult to discern from models that include larger numbers of kinetic pathways. The results of the physically intuitive computer model are used to describe the behavior of the quenching mechanism responsible for limiting the yield of singlet oxygen within RF and μ-wave electric discharges (13.56 MHz and 2.45 GHz, respectively).

The destruction rate of $O_2(a\ ^1\Delta)$ increases by an order of magnitude between the RF and μ-wave electric field frequencies. This drastic change links the destruction mechanism to electron concentrations. The $O_2(a\ ^1\Delta)$ destruction rate extracted from the data is invariant as pressure and velocity of the gas flow through the discharge changes. The role played by electrons as well as atomic oxygen in the destruction of $O_2(a\ ^1\Delta)$ will be explored. Furthermore destruction of $O_2(a\ ^1\Delta)$ by collisions with vibrationally excited oxygen may play an important role in the plasma kinetics.

II Background and Theory

This chapter will present the theory and background relevant to the study of oxygen plasmas, starting with a general discussion of the operation of COIL devices and then the operation of EOIL devices with an emphasis on the advantages and technical challenges of an EOIL device. The optical diagnostics used to measure the change in relative magnitude of the excited species without perturbing the plasma are also discussed. In the case of $O_2(a)$ and $O_2(b)$, the optical signatures involve molecular spectroscopy; its theory is well established and discussed in this chapter. The actinometry technique is used to determine the O-atom concentration within the discharge region. This technique and its associated spectroscopy are also discussed. The temperature of the gas changes as it flows through the plasma region, so a theoretical description of gas heating and cooling is discussed. To improve the understanding of the chemical kinetics occurring within the plasma from changes in the concentrations of measured excited species, a model of the chemical kinetics has been developed and is described in Section 4.6. The rate package used in this model is dependent on the electron energy distribution within the plasma. A preexisting Boltzmann solver, called BolSig+, is used to determine the rate coefficients for the model used in this study. Finally, the current status of research in the area of EOIL development is discussed within the context of power scaling and increasing the yield of $O_2(a)$ in oxygen plasmas.

2.1 Chemical Oxygen-Iodine Laser

The COIL system was first demonstrated in 1977.[19] The electrically excited state of oxygen, $O_2(a)$, is populated by a chemical reaction between chlorine gas and liquid basic hydrogen peroxide. This is a multiphase process governed by the stoichiometry:

$$Cl_2 + H_2O_2 + 2KOH \xrightarrow{k_{COIL}} O_2(a\ ^1\Delta) + 2H_2O + KCl \qquad (2.1)$$

The radiative lifetime of the $O_2(a)$ state is 64 minutes.[20] This excited state is also resistant to collisional deactivation at surfaces.[21] Therefore, once it is created by the chemical reaction, this state will persist for long periods of time. A population inversion between the $O_2(a)$ and $O_2(X)$ is easily achieved; however, the cross-section for the stimulated emission is small. The COIL system uses the near resonant energy transfer from the electrically excited $O_2(a)$ state and atomic iodine $I(^2P_{1/2})$ state to create a population inversion in the iodine.

The $I(^2P_{1/2})$ and $O_2(a)$ excited states are separated by only 0.03 eV, allowing a very efficient transfer of the energy from the $O_2(a)$ state of oxygen to the iodine lasing state. However, the iodine injected into the gas flow is not atomic; it is in the molecular state. The molecular iodine must be dissociated first before the atomic iodine can be excited. The energetics for the dissociation of molecular iodine are also shown in Figure 2.1 and require the sacrifice of at least two, but typically five, $O_2(a)$ molecules in gas flows of pure $O_2(a)$. For the EOIL system, I_2 is dissociated via many pathways, including collisional dissociation with the $O_2(b)$ state and O-atoms.[3, 22, 23, 24]

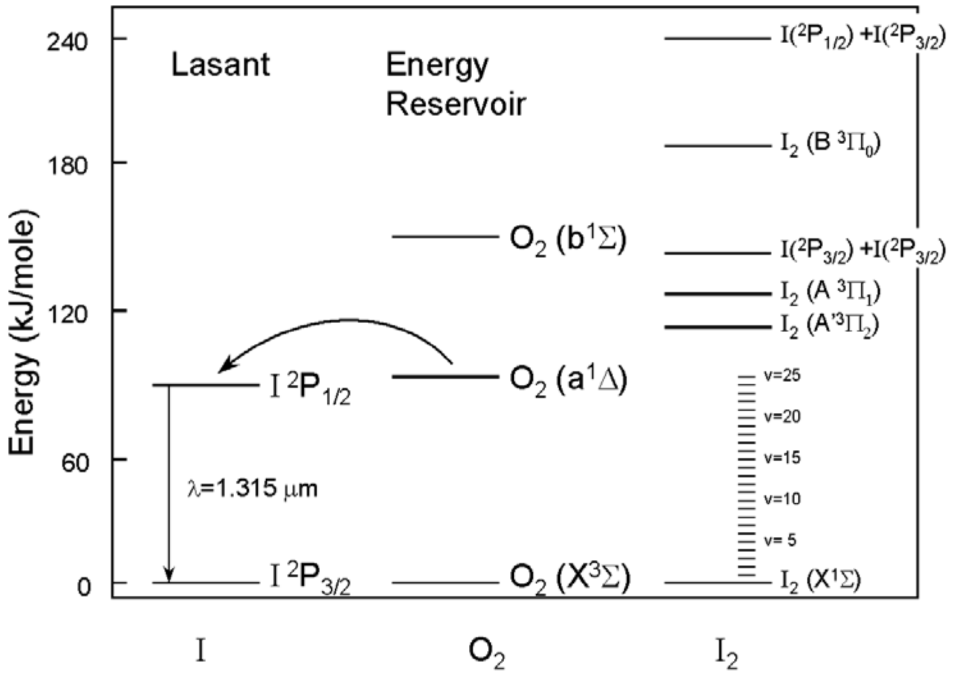

Figure 2.1 Energy level diagram for COIL, illustrating the resonant energy transfer from metastable reservoir *$O_2(a\,^1\Delta)$* to the upper lasing level of atomic iodine $I(^2P_{1/2})$. The energy levels for several key states involved in the dissociation of molecular iodine are also provided.[24]

A schematic for a simple COIL device is shown in Figure 2.2. As is observed in the schematic, the waste water and salt from the chemical reaction is removed from the gas flow. The gas is cooled by supersonic expansion, while iodine is injected into the gas flow. The chemicals are then exhausted from the laser cavity, taking any waste heat with them.

The gain in the system is generated through the population inversion of $I(^2P_{1/2})$ versus the $I(^2P_{3/2})$ state of the iodine atom, which emits at λ = 1.315 μm. The population inversion is attained by energy transfer:

$$O_2(a\,^1\Delta) + I(^2P_{3/2}) \longleftrightarrow O_2(X\,^3\Sigma) + I^*(^2P_{1/2}) \tag{2.2}$$

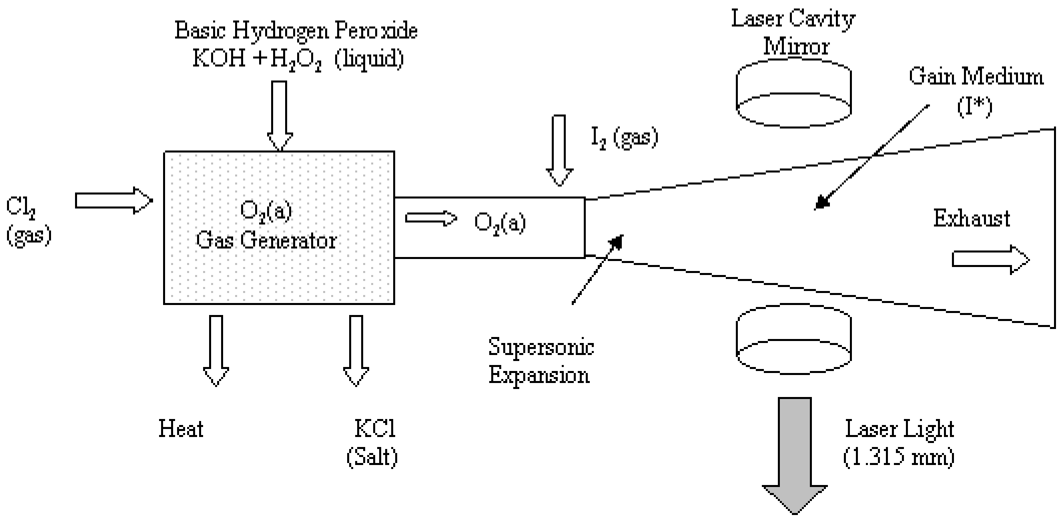

Figure 2.2 Schematic view of chemical oxygen-iodine system, including supersonic expansion of gas (adapted from Carrol).[3]

Assuming that this is the only important kinetic reaction occurring, the steady-state relationship between the excited states and their ground states is:

$$\frac{\left[I\left({}^2P_{1/2}\right)\right]}{\left[I\left({}^2P_{3/2}\right)\right]} = K_{eq}(T_g)\frac{\left[O_2\left(a^1\Delta\right)\right]}{\left[O_2\left(X^3\Sigma\right)\right]_0} \tag{2.3}$$

where

$$\left[O_2\left(X^3\Sigma\right)\right]_0 = \left[O_2\left(X^3\Sigma\right)\right] + \left[O_2(v)\right] + \left[O_2\left(a^1\Delta\right)\right] + \left[O_2\left(b^1\Sigma\right)\right] + {}^1\!/_2\left[O\left({}^3P\right)\right] + 1.5\left[O_3\right] \tag{2.4}$$

And, from Perram et al.[20]:

$$K_{eq}(T) \approx 0.75\exp\left({}^{402}\!/_{T_g}\right) \tag{2.5}$$

where T_g is given in Kelvin.

The ratio of $I({}^2P_{1/2})/I({}^2P_{3/2})$ is directly related to the yield of the $O_2(a)$ that results from the singlet oxygen generator (SOG). Note that the equilibrium constant is temperature-dependent. By cooling the gas, the yield, Y_a, required to reach the threshold is decreased. Note that the value of $[O_2]_0$ (used in determining Y_a) in a conventional COIL is $[O_2(X)]+[O_2(a)]$, because the other species do not obtain significant concentrations. The threshold for gain (at T_g = 295 K) is achieved when Y_a is approximately 15%. By virtue of K_{eq}, the threshold yield is reduced to approximately 5% at the point of supersonic expansion by reducing the gas temperature to 160 K. Typical yields from the RotoCOIL SOG used in a COIL are 80%.[26]

2.2 Electric Discharge Pumped Oxygen-Iodine Laser

The primary difference between an EOIL and a conventional COIL system is the SOG. Changing this component introduces limits to yield, temperature issues, and excited species that do not exist in the conventional chemical system and will require adjustments to the laser system. In Figure 2.3, a schematic of a typical EOIL system is shown.

In Figure 2.3, the system exhaust, laser cavity, and supersonic gas expansions are all very similar to those shown for the conventional COIL system. The system's SOG is an electric discharge.

The major differences between a chemistry based SOG and a discharge-based SOG are: (1) Y_a is smaller, approximately 10-15%; (2) gas temperatures within the plasma are much higher, commonly reaching temperatures of 700 K and higher; and (3) a myriad of other excited species, such as O-atoms and vibrationally excited O_2, are formed, possibly limiting the maximum achievable $O_2(a)$ population and reacting with I*, which will reduce the achievable gain within the discharge.[2, 3]

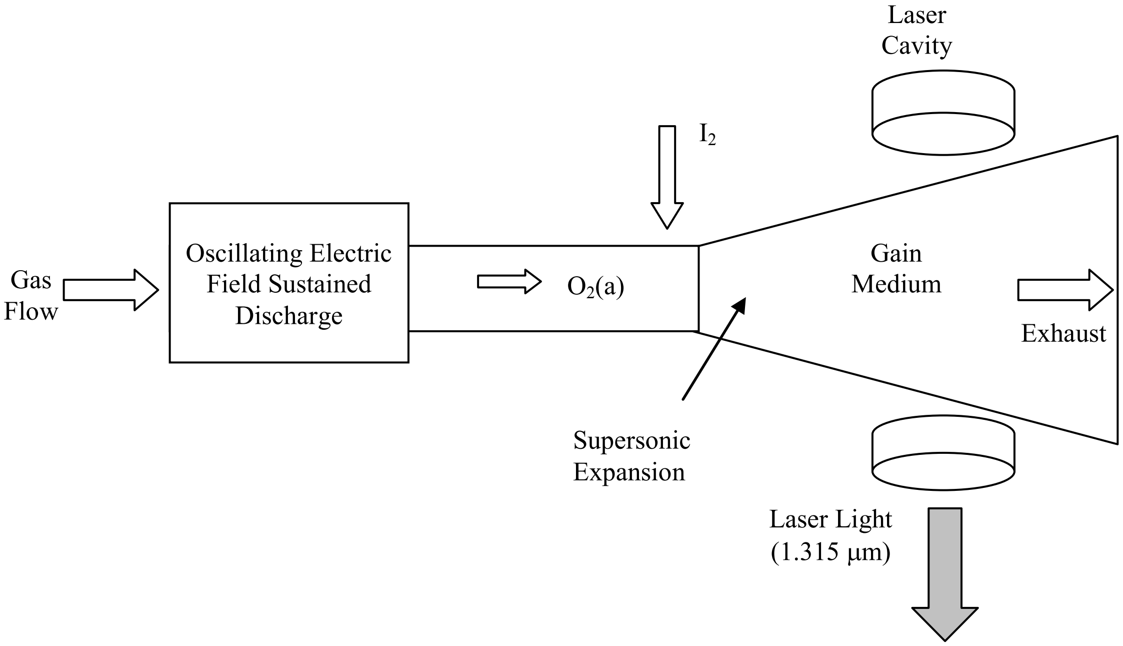

Figure 2.3 Schematic of a typical EOIL system, including a discharge-driven singlet oxygen generator, a supersonic flow to cool the gas before the laser cavity, iodine injection, and the laser cavity itself (adapted from Carrol et al.).[3]

2.3 Calculating Electron Energy Dependent Rates

Gas discharge models require the use of rate coefficients, which are dependent on the electron energy distribution within the plasma, as shown below:

$$k_i(E/N) = \left(\frac{2e}{m}\right)^{1/2} \int_0^{\infty} \sigma_i(\varepsilon)\varepsilon^{1/2} f(\varepsilon; E/N) d\varepsilon \tag{2.6}$$

$k_i(E/N)$ is the rate coefficient of the ith reaction; e is the fundamental charge of an electron; m is the electron mass; $f(\varepsilon; E/N)$ is the electron energy distribution function

(EEDF); ε is the electron energy; $\sigma_i(\varepsilon)$ is the ith electron impact cross-section; *E* is the electric field strength; and *N* is the number density of collision partners. In this work, *N* will be the ground state of molecular oxygen, because, under most conditions, 70% or more of the gas flow remains in the ground state. In plasmas, electrons are accelerated by the electric field and slowed by collisions, so a key parameter of a plasma is the value of *E/N* or the reduced electric field.[27]

The BolSig+ solver provides a steady-state solution of the Boltzmann equation for electrons in a uniform electric field, using the classic two-term expansion.[27] At high values of *E/N* (where most collisions are inelastic) and *f* (the distribution function becomes anisotropic), the two-term approximation will fail. The errors in calculated transport coefficients are acceptable for fluid discharge modeling in the range of most studies.[27] The typical reaction rates for this study are shown in Table 2.1. In this table, the reaction rate for elastic collisions is 5.9×10^{-8} cm^3 s^{-1}, which is much larger than the reaction rates for inelastic interactions of electrons with ground state oxygen. Therefore the conditions of this study are well within the conditions where the two-term expansion is valid.

In general, the EEDF, $f_\varepsilon(\varepsilon) = 2/\sqrt{\pi}\,(k_B T_e)^{-3/2}\,\varepsilon^{1/2}\exp[-\varepsilon/k_B T_e]$, may be calculated from the fundamental collisional cross-section data (of the gases in which the plasma is being sustained) by solving the Boltzmann equation. The average energy of the electrons, ε_{avg}, is the average value of ε using the EEDF[27]:

$$\varepsilon_{avg} = \int_0^\infty \varepsilon f_\varepsilon(\varepsilon) d\varepsilon \qquad (2.7)$$

Table 2.1 Reaction rates for this work. Values calculated at 4 Torr, T_g = 1,185 K, and T_e = 3.2 eV (given in units of $cm^3\ s^{-1}$ with the exception of reaction 24 in units of $cm^6\ s^{-1}$).

Reaction Number, k	Name	Reaction	Reaction Rate Coefficient	Source
1	Elastic Collisions	$e^- + [O_2(X)] \longrightarrow [O_2(X)] + e^-$	$k_{Elas} = 5.9 \times 10^{-8}$	28
2	Dissociative Attachment	$e^- + O_2(X) \xrightarrow{k_{attch}} O^- + O$	$k_{\mathrm{attach}}(\mathrm{T_e}) = 1.9 \times 10^{-11}$	28
3-9	Vibrational Excitation	$e^- + O_2(X) \xrightarrow{k_v} O_2(v) + e^-$	*v = 0.02 to 0.75eV* $= 5.3 \times 10^{-11}$	28
10	Excitation 0.98 eV	$e^- + O_2(X) \xrightarrow{ka+} O_2(a) + e^-$	$k_{\mathrm{a+}}(\mathrm{T_e}) = 4.2 \times 10^{-10}$	28
11	Excitation 1.63 eV	$e^- + O_2(X) \xrightarrow{kb+} O_2(b) + e^-$	$k_{\mathrm{b+}}(\mathrm{T_e}) = 9.9 \times 10^{-11}$	28
12	Excitation 4.50 eV	$e^- + O_2(X) \xrightarrow{k_{A+}} O_2(A,{}^3\Sigma) + e^-$	$k_{\mathrm{A+}}(\mathrm{T_e}) = 1.6 \times 10^{-10}$	28
13	Excitation 6.0 eV	$e^- + O_2(X) \xrightarrow{k_{O+}} O({}^3P) + O({}^3P) + e^-$	$k_{\mathrm{OP+}}(\mathrm{T_e}) = 2.2 \times 10^{-10}$	28
14	Excitation 8.4 eV	$e^- + O_2(X) \xrightarrow{k_{O+}} O({}^3P) + O({}^1D) + e^-$	$k_{\mathrm{OD+}}(\mathrm{T_e})\,) = 2.3 \times 10^{-10}$	28
15	Excitation 9.97 eV	$e^- + O_2(X) \xrightarrow{k_{O+}} O({}^3P) + O({}^1S) + e^-$	$k_{\mathrm{OS+}}(\mathrm{T_e})\,) = 1.7 \times 10^{-13}$	28
16	Ionization 12.06 eV	$e^- + O_2(X) \xrightarrow{k_{ion}} O_2^+ + e^- + e^-$	$k_{\mathrm{ion}}(\mathrm{T_e})\,) = 1.0 \times 10^{-12}$	28
17	Deexcitation 0.98 eV	$e^- + O_2(a) \xrightarrow{k_{a-}} O_2(X) + e^-$	$k_{\mathrm{a-}}(\mathrm{T_e}) = 5.4 \times 10^{-10}$	*Detailed Balance*
18	Recombination	$e^- + O_2^+(X) \xrightarrow{k_{rec}} O({}^3P) + O({}^3P)$	$k_{\mathrm{rec}}(\mathrm{T_e}) = 1.6 \times 10^{-8}$	*20*
19	Atomic Recombination	$O + O + Wall \xrightarrow{k_{wall}} O_2(X)$	$k_{\mathrm{wall}} = 2400$	*20*
20	Detachment	$O^- + O_2(a) \xrightarrow{k_{Ode}} O_3 + e^-$	$k_{Ode} = 3.0 \times 10^{-10} \left(T_g/300\right)^{0.5}$ $= 6.0 \times 10^{-11}$	*20*
21	Ionic Recombination	$O^- + O_2^+(X) \xrightarrow{k_{Orec}} O + O_2(X)$	$k_{Orec} = 2.0 \times 10^{-7} \left(T_g/300\right)^{-1}$ $= 5.1 \times 10^{-8}$	*20*
22	Quenching by $O_2(X)$	$[O_2(a)] + [O_2(X)] \to 2[O_2(X)]$	$k_{O2x} = 3.0 \times 10^{-18} e^{-200/T_g}$ 2.5×10^{-18}	*29*
23	Quenching by O-atoms	$[O] + [O_2(a)] \to O + [O_2(X)]$	$k_{aO} = 2.0 \times 10^{-16}$	*30*
24	Three Body Reaction	$[O] + [O_2(X)] + [O_2(a)] \to [O] + 2[O_2(X)]$	$k_{3body} = 1.0 \times 10^{-32}$	*17*
25	Quenching by Ozone	$[O_3] + [O_2(a)] \to [O_3] + [O_2(X)]$	$k_{aO3} = 2.0 \times 10^{-11} e^{-2840/Tg}$ $= 1.8 \times 10^{-12}$	*29*
26	Electron Interaction	$[e^-] + [O_2(a)] \to [e^-] + All$	$k_{ae} \approx f(\varepsilon_{avg}) \times 10^{-10}$ $= 6.7 \times 10^{-10}$	*Scaled*
27	Vibrationally Excited O_2	$[O_2(v)] + [O_2(a)] \to [O_2(b)] + [O_2(X)]$	$k_v \approx 4 \times 10^{-10}$	*This Work*
28	Pooling	$[O_2(a)] + [O_2(a)] \to [O_2(X)] + [O_2(b)]$	$k_{pool} = 9\ \times 10^{-17}\ e^{(-560/\mathrm{Tg})}$ $= 8.2 \times 10^{-18}$	*30*
29	Quenching of O- by O-atoms	$O^- + M \to O + M + e^-$	$k_{oneg} = 8 \times 10^{-10}$	*31*
30	$O({}^1D)$ quenched $O_2(X)$	$[O({}^1D)] + [O({}^3P)] \to [O({}^3P)] + [O({}^3P)]$	$\mathrm{K_{O1D}} = 8 \times 10^{-12}$	*18*
31	$O({}^1D)$ excites $O_2(a)$	$[O({}^1D)] + [O_2(X)] \to [O({}^3P)] + [O_2(a)]$	$\mathrm{k_{a1D}} = 1.6 \times 10^{-12}\ e^{(-67/\mathrm{Tg})}$ $= 1.5 \times 10^{-12}$	*29*
32	$O({}^1D)$ excites $O_2(b)$	$[O({}^1D)] + [O_2(X)] \to [O({}^3P)] + [O_2(a)]$	$\mathrm{k_{b1D}} = = 2.56 \times 10^{-11}\ e^{(-67/\mathrm{Tg})}$ $= 2.4 \times 10^{-11}$	*29*

Using this definition of average energy, the temperature of the electrons in electron-volts, T_e, is defined as:

$$T_e = \frac{2}{3}\varepsilon_{avg} \tag{2.8}$$

Kinetic rates are calculated from their integral form shown in Equation 2.6 and are dependent on the EEDF. However, using the EEDF is cumbersome, so the electron temperature, as defined above, is used to define the system for the sake of convenience when discussing the plasma's state.[27]

In Table 2.1, all of the reactions used in this study are listed, and approximate values are given. Reactions 1-16 are used in the BolSig+ model to determine the EEDF.[27] Reaction 1 represents the rate of elastic collisions between the oxygen in the gas flow and electrons. Even though the rate coefficient of this reaction is large, the energy exchange between the very light electrons and heavy oxygen molecules is very small. As a result, the reaction does not play a significant role in the energy balance of the plasma. The reaction rates are determined for a plasma maintained at a pressure of 4 Torr, a flow velocity of 20 m/s, and an E-field operating at 2.45 GHz. These particular plasma conditions are relevant to the experimental discussions in Chapter 4. Reactions 17-32 will be used throughout this document, and their approximate values are determined assuming a gas temperature of 1,200 K, which is typical for this study.

For a given gas composition and field frequency, BolSig+ numerically solves the Boltzmann equation to determine the EEDF, referencing tabulated cross-section data. Using the calculated EEDF, the model then numerically integrates to determine the electron energy dependent rate coefficients associated with reactions 1-16. The BolSig+ solver has been cited in over 35 publications and used to determine the EEDF in a variety of gas mixtures, including oxygen, nitrogen, argon, and helium.[27, 32-34] The cross-sections included in Figure 2.4 are inputs to the BolSig+ model. The measurement of these cross-sections was reported by Phelps, 1985.[28] The typical electron temperatures of the discharges studied in this work are approximately 3 eV.

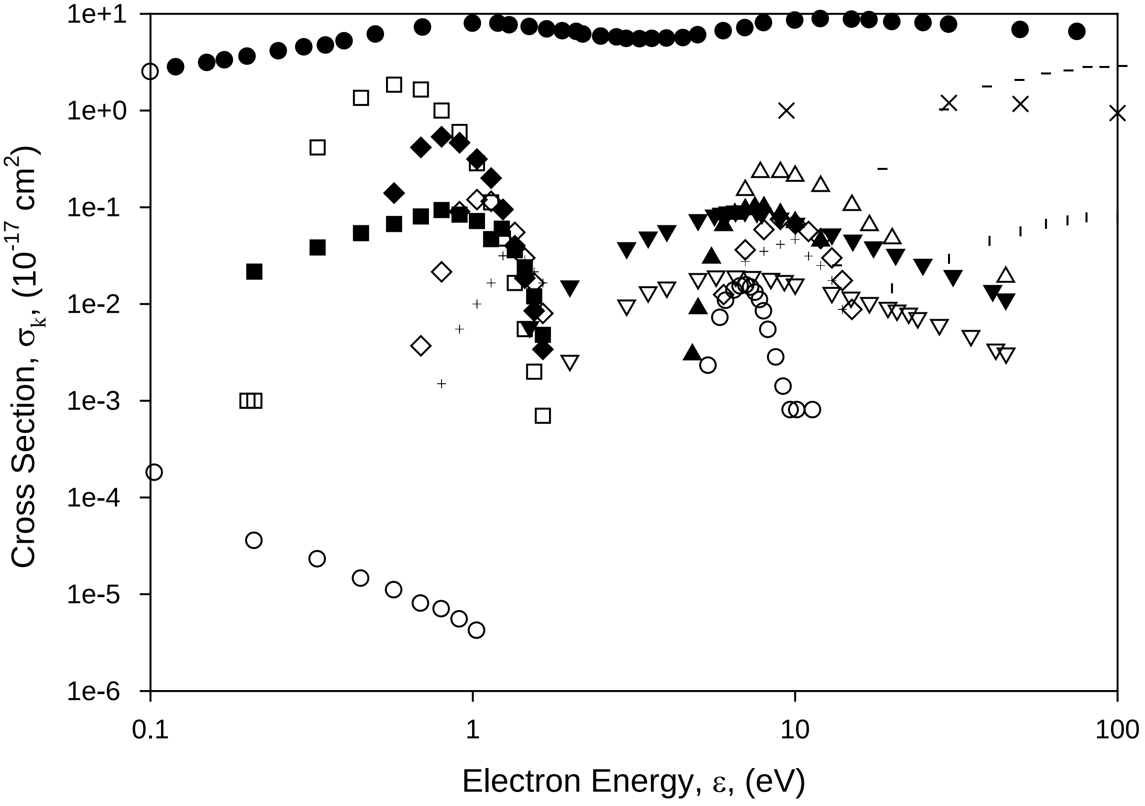

Figure 2.4 Cross-sections for the production of excited states of oxygen included in the BolSig+ model. ● elastic collisions reaction 1; ○ dissociative attachment reaction 2; ■ vibrational excitation 0.02 eV reaction 3; □ vibrational excitation 0.19 eV reactions 4 and 5; ♦ vibrational excitation 0.38 eV reactions 6 and 7; ◊ vibrational excitation 0.57 eV reaction 8; + vibrational excitation 0.75 eV reaction 9; ▼ *$O_2(a)$* production reaction 10; ▽ *$O_2(b)$* production reaction 11; ▲*$O_2(A)$* production reaction 12; △ dissociation reaction 13; X dissociation producing *$O(^1D)$* reaction 14; | dissociation producing *$O(^1S)$* reaction 15; — ionization reaction 16.

Even though the average electron energy is 3 eV, reactions with energy thresholds larger than 3 eV, such as ionization, may have significant rates of production, because the tails of the EEDFs extend into higher energies. Some EEDFs for different E/Ns are shown in Figure 2.5. Typical E/N values for this work range from 80 to 200 Townsend (Td), which is defined as 1 x 10^{-17} V-cm.^{2}

The average E/N values for this study are 55.6 Td, which yields an average electron energy of 3.2 eV. As seen in the 55.6 Td case, there is a significant population of electrons with energies above 5 eV. Because the electron populations with high energies can be large, the probability of exciting high-energy oxygen states in a plasma can also become large.

It is important to note that this energy distribution would be exponential if Boltzmann statistics prevailed. Consequentially, the reduced energy distribution would be linear, on a semi-log plot, Figure 2.5. This difference in the EEDF demonstrates the need for using the BolSig+ model for this study. The rate coefficients in Figures 2.6 and 2.7 are for the reactions included in BolSig+. The shaded areas in these figures are the energy ranges of interest for the two different oscillation frequencies studied in this work. The rate coefficients are calculated by the integration shown in Equation 2.6. In producing Figures 2.6 and 2.7, the BolSig+ code was run over a range of E/N with values from 1 to 250 Td and 1 – 450 Td consecutively.

Introducing an oscillating field changes the EEDF, if the frequency, ω, of the field is fast enough that the field direction changes before the average electron experiences a collision.

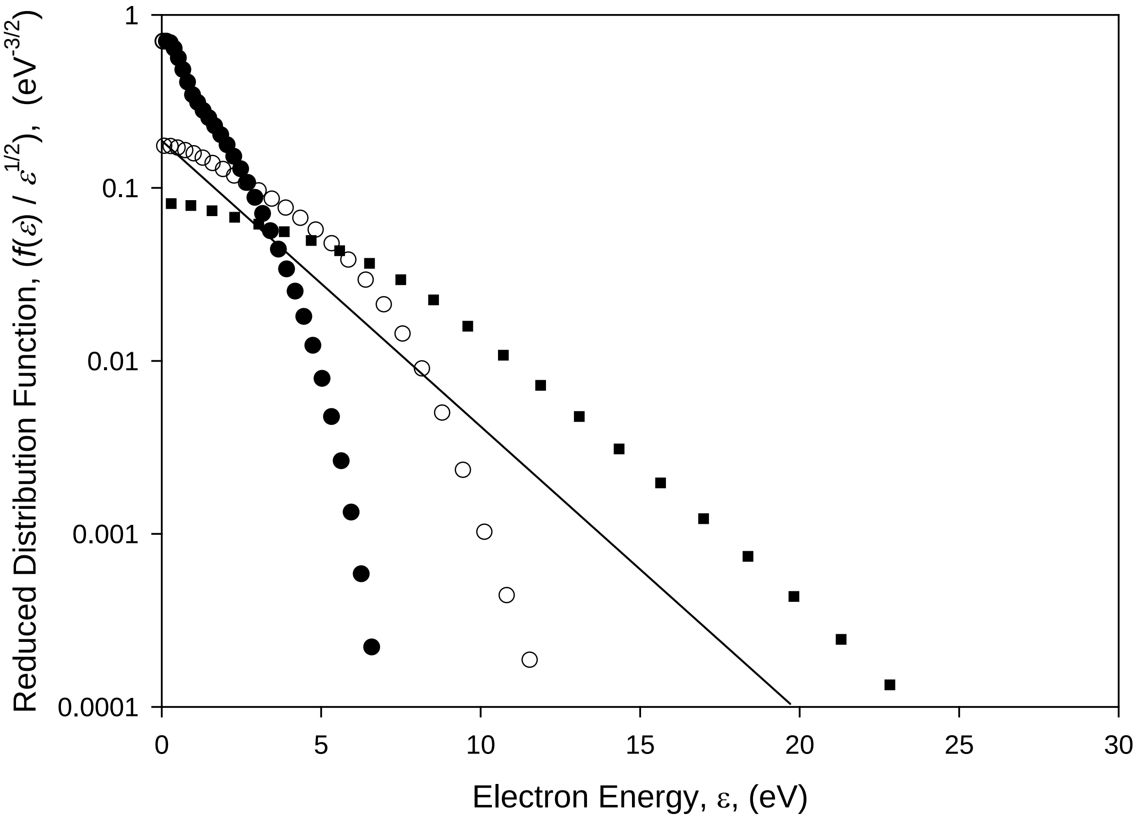

Figure 2.5 Comparison of Maxwellian distribution at *Te* = 3.2 eV, —, to the electron energy distribution functions in oxygen with a μ-wave field with reduced electric field values of ● 10, ○ 55.6, and ■ 200 Td.[27]

The approach to describing oscillating systems is to introduce an effective electric field (E_{eff}) that includes the effects of the field frequency[7] as shown in and MacDonald, 1949[35]:

$$E_{eff} = E\sqrt{\frac{{v_c}^2}{\omega^2 + {v_c}^2}} \tag{2.9}$$

where E is the rms value of the electric field, v_c is the collision frequency, and ω is the radian frequency of the oscillating field.

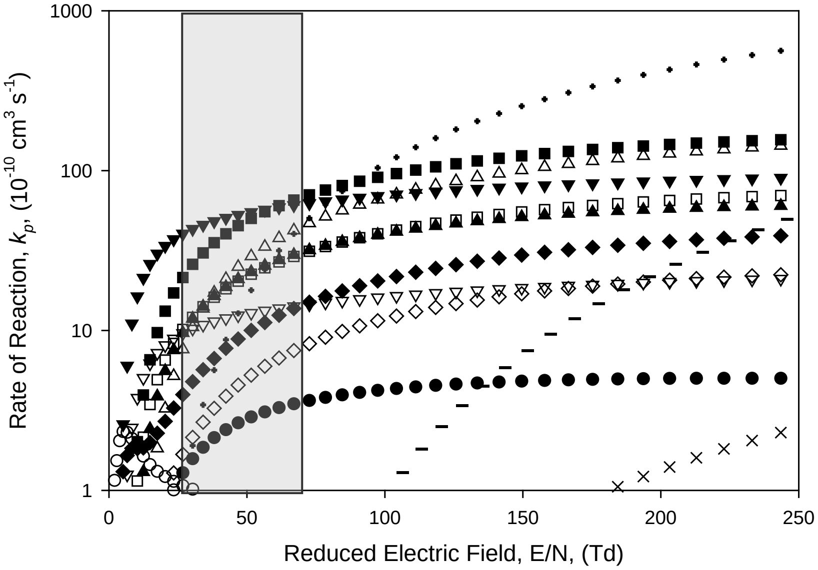

Figure 2.6 The reaction rates as a function of reduced electric field for a pure oxygen discharge and an RF field, 13.56 MHz.[27] ● attachment reaction 2; ○ vibrational excitation 0.02 eV reaction 3; ■ vibrational excitation 0.19 eV reactions 4 and 5; □ vibrational excitation 0.38 eV reactions 6 and 7; ♦ vibrational excitation 0.57 eV reaction 8; ◊ vibrational excitation 0.75 eV reaction 9; ▼ $O_2(a)$ production reaction 10; ▽ $O_2(b)$ production reaction 11; ▲$O_2(A)$ production reaction 12; △ dissociation reaction 13; + dissociation producing $O(^1D)$ reaction 14; X dissociation producing $O(^1S)$ reaction 15; ▬ ionization reaction 16.

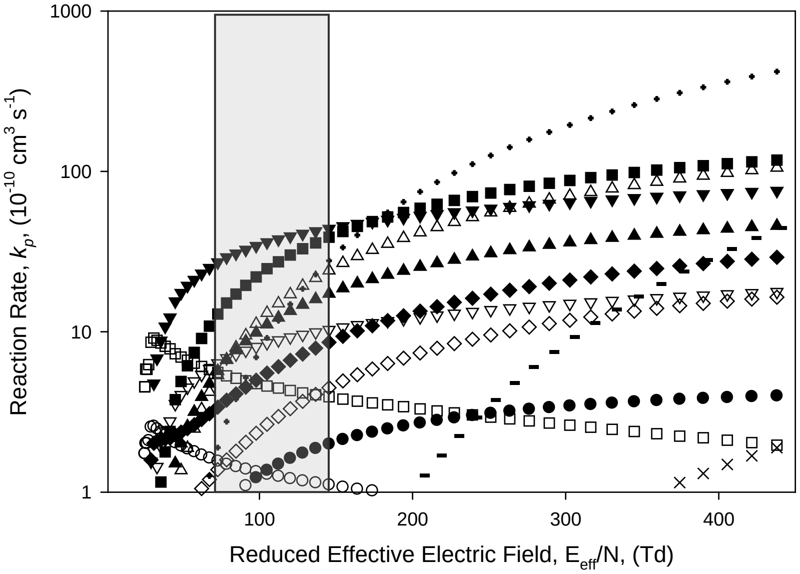

Figure 2.7 The reaction rates as a function of reduced electric field for pure oxygen gas in a μ-wave frequency oscillating field; 2.45 GHz.[27] ● attachment reaction 2; ○ vibrational excitation 0.02 eV reaction 3; ■ vibrational excitation 0.19 eV reactions 4 and 5; □ vibrational excitation 0.38 eV reactions 6 and 7; ♦ vibrational excitation 0.57 eV reaction 8; ◊ vibrational excitation 0.75 eV reaction 9; ▼ $O_2(a)$ production reaction 10; ▽ $O_2(b)$ production reaction 11; ▲$O_2(A)$ production reaction 12; △ dissociation reaction 13; + dissociation producing $O(^1D)$ reaction 14; X dissociation producing $O(^1S)$ reaction 15; ▬ ionization reaction 16.

Note that when ω is sufficiently small in comparison to the collision frequency, the fraction in Equation 2.9 approaches 1, and hence, the effective electric field is equal to the rms value of the electric field.[35, 36] At 7 Torr and above, the collision frequency is large enough that E_{eff} is not sufficiently perturbed from the rms value of the electric field. However, at pressures lower than 7 Torr, the effects become increasingly stronger. In Figure 2.7, the reaction rates are shown for a μ-wave frequency electric field operating at 2.45 GHz in 4 Torr of oxygen. The different ranges of E_{eff}/N for the two different E-field frequencies have a large affect upon the ionization rate and will be discussed further in Section 4.8.

2.4 Energetic Species Monitored within the Discharge

Within an electric discharge, a number of excited species are created. Information on plasma conditions can be extracted from observing the emissions from excited species. The energy levels of most of the monitored species are shown in Figure 2.8. It requires 5.2 eV to dissociate the oxygen molecule into two neutral atoms, 1.6 eV to excite the $O_2(b)$ state, and 0.98 eV to excite the metastable $O_2(a)$ state. Figure 2.8 also shows that the energy of the $O_2^-(X)$ state and O^- state are more energetically stable than the ground state of oxygen.

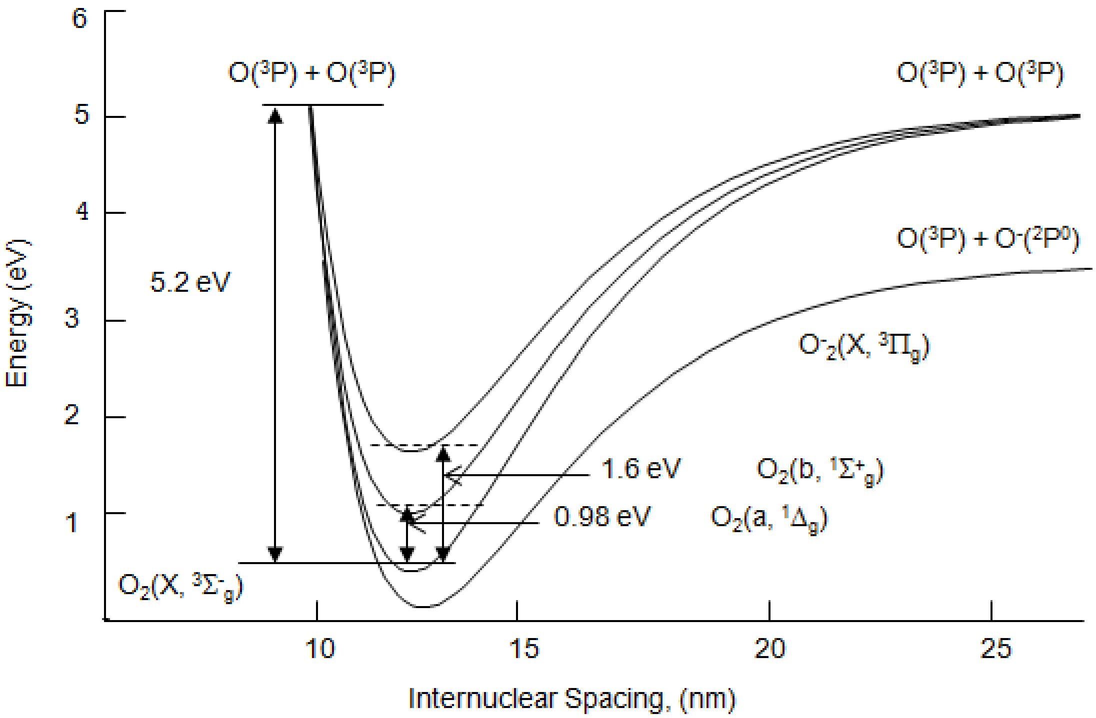

Figure 2.8 Morse potentials representing the energy levels of ground state, $O_2(a)$, $O_2(b)$, and the dissociation energy of the oxygen molecule.

2.4.1 Spectral Emissions from the $O_2(a)$ State

The transition of the singlet oxygen a-state to the ground state of oxygen, $O_2\left(a, {}^1\Delta, v' = 0 \rightarrow X, {}^3\Sigma_g, v'' = 0\right)$, is centered at 1,268 nm and is spin and angular momentum disallowed; however, the transition is magnetic dipole allowed. The spectrum, measured with a 0.33 meter spectrometer, is shown in Figure 4.11, while the possible branches for this system are shown in Figure 2.9.[37] The expected transitions are for ΔK = 0, ±1, ±2. K is the quantum number related to total angular momentum, excluding spin, which becomes a good quantum number under Hund's case b.[37] Hund's case b predicts quantum mechanical energy levels when the spin vector, S, is not strongly coupled to the intra-nuclear axis. Therefore, the possible values of the total angular momentum quantum number, *J*, are from K+S to the absolute value of K-S, in integer steps. The $O_2(a)$ state has an angular momentum quantum number of two, and the spin is equal to zero. The subscript, g, refers to the inversion symmetry of the eigenstate of the energy level.[37]

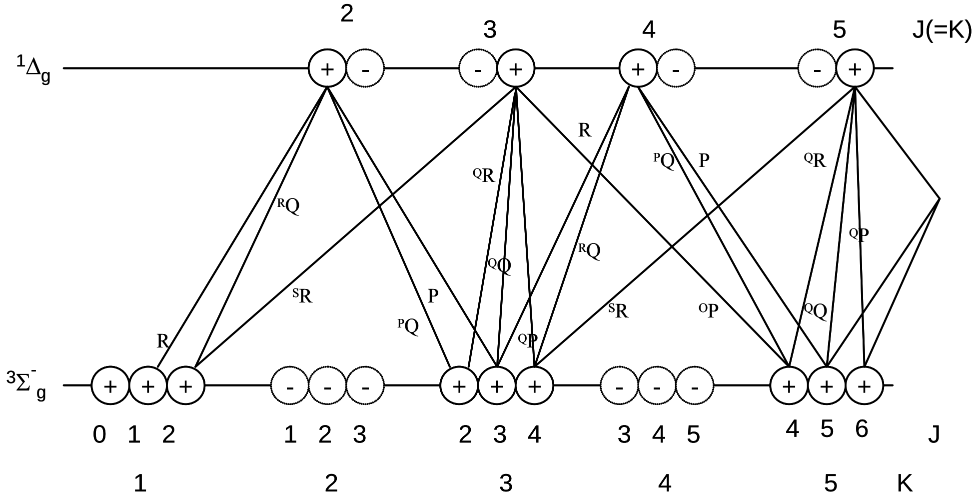

Figure 2.9 Branches of Magnetic Dipole Branches for $O_2(a)$ emissions (adapted from Herzberg).[37]

The $O_2\left(a^1\Delta_g \rightarrow X^3\Sigma_g^1\right)$ transition has a complex and dense rotational structure, with nine rotational branches ($^{\Delta K}\Delta J = {}^OP, {}^PP, {}^PQ, {}^QP, {}^QQ, {}^QR, {}^RR, {}^RQ, {}^SR$).[37] The negative or broken circle transitions are asymmetric states and are absent from the emission spectra due to the zero nuclear spin. The same will be true in the $O_2(b)$ emissions in Figure 2.10.

2.4.2 Spectral Emissions from the $O_2(b)$ State

The emission spectrum for the $O_2(b)$ excited state to the $O_2(X)$ ground state is centered at 762 nm. The total orbital angular momentum is equal to zero for both states involved. The spin of the upper state is zero, while the spin of the ground state is one.

The doublets that appear in the $O_2(b)$ spectra are caused by the close spacing between the ${}^{P}P$ and ${}^{P}Q$ branches (along the P branch side of the spectra) and the ${}^{R}R$ and ${}^{R}Q$ branches (on the R branch side of the spectra).[37] These transitions are shown in Figure 2.10. The intensity of the emission lines, $I_b(J')$ in the ${}^{P}P$ and ${}^{P}Q$ branches, may be used to derive the rotational temperature and are defined as:

$$I_b(J') = CS_{J''}^{J'} N(J') \tag{2.10}$$

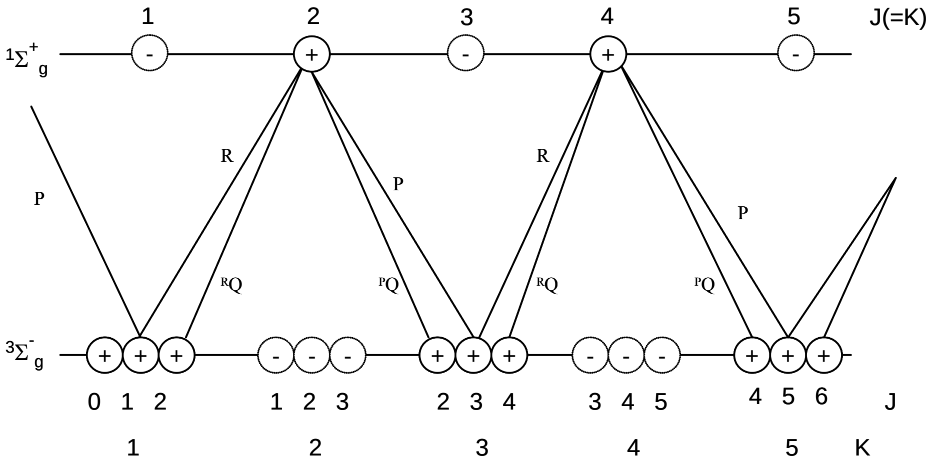

Figure 2.10 Possible branches for the *O₂(b)* emissions to the ground state (adapted from Herzberg).[37]

where

$$\frac{N(J')}{\sum_{J'} N(J')} = \left(\frac{hcB_{v'=0}}{kT_R}\right)(2J'+1)\exp\left(-F(J')hc/kT_R\right) \tag{2.11}$$

and

$$S(J') = rotational\ line\ strength = \begin{cases} (J'+1)/2 & {}^{R}R \\ (J'+.25)/2 & {}^{R}Q \\ (J'-.25)/2 & {}^{P}P \\ (J'+1)/2 & {}^{P}Q \end{cases}. \tag{2.12}$$

$N(J')$ is the concentration of $O_2(b, v'=0, J')$; *v* indicates the vibrationally excited state; *C* is an arbitrary scale factor, including radiometric and detectivity factors; $B_{v'=0} = 1.39138\ cm^{-1}$; $D_{v'=0} = 5.486\times10^{-6}\ cm^{-1}$ [15, 38, 39]; $F(J')$ = rotational energy, which is equal to $B_{v'=0}J'(J'+1) - D_{v'=0}\left(J'(J'+1)\right)^2$; and T_R = rotational temperature. The value of T_R may be extracted from the measurement of the excited states' emissions. This method is used to determine the gas temperature in Chapter 4.

2.5 Heat Transport for a Gas Flow in a Cylindrical Vessel

The velocity of the gas flow is controlled by gas flow controllers. The gas flow controllers measure gas flow in standard cubic centimeters per minute (SCCM). Calculating the gas velocity from the measured SCCM is more or less a unit conversion from SCCM to cm/s. Standard cubic centimeters assume that the gas is at standard temperature and pressure (STP), meaning that pressure is 760 Torr and the gas is at 300 K. A plug flow model is used, ignoring the effects of the wall on the velocity. The validity of this assumption is based on the flow having a Reynolds number of less than 500, which is discussed in greater detail in Appendix A. So, the mapping from SCCM to cm/s is:

$$v_g = \frac{\dot{n}}{NA} = \left(0.0432\right)\frac{\dot{n}T_g}{AP} \tag{2.13}$$

where v_g is the gas velocity; N is the number density of the oxygen in the gas flow determined by the gas pressure and temperature; A is the area of the flow tube; and $\dot{n}$ is the mass flow rate measured in SCCM. The quantities on the right-hand side of Equation 2.13 are all measured quantities; therefore, velocity is a simple calculation. Flow velocities are calculated in Chapter 3.

Using a simple heat transfer model, the fraction of the discharge power coupled to the gas temperature is determined. Also, an experimental determination of the Nusselt number is possible.[40] The Nusselt number will be discussed in greater detail in Chapter 4.

As discussed in Appendix A, the energy equation for gas in a gas flow may be written as[40]:

$$\rho V C_p \frac{dT_g}{dt} = fP_{in} - Sh_T(T_g - T_0) \tag{2.14}$$

P_{in} is the power coupled into the gas; f is the fraction of the power going to gas heating; $S = 2\pi rl$ is the surface area of the cylindrical tube, where the tube radius $r = 0.005$ m and the length of the plasma $l = 0.025$ m; h_T is the heat transfer coefficient, which varies less than 15% in the temperature range of interest; ρ is the mass density of the gas; V is the discharge volume; and $C_p = 1.005$ kJ/(kg K), which is the heat capacity of oxygen.[40]

The pressure in the flow tube was measured along the length of the flow tube and exhibits a less than 1% change in value. Therefore, the gas pressure is assumed to remain constant, and any change in the gas temperature will change the gas density, but not the gas pressure, as governed by the ideal gas law. Expressing the density in terms of pressure and temperature via the ideal gas law, the equation may now be written as:

$$mVC_p \frac{P}{k_B T_g} \frac{dT_g}{dt} = -Sh_T (T_g - T_0) + fP_{in} \tag{2.15}$$

After introducing P_0/P as a unitless scaling term, the pressure-dependent data is collapsed to a single functional form:

$$\frac{1}{T_g} \frac{dT_g}{dt_r^{'}} = -\frac{k_B Sh_T}{P_0 mVC_p} (T_g - T_0) + \frac{k_B fP_{in}}{P_0 mVC_p} \tag{2.16}$$

where k_B is the Boltzmann constant; P is pressure; m is the mass of oxygen; and

$$t_r^{'} = t\left(\frac{P_0}{P}\right) \tag{2.17}$$

is the pressure normalized time of the system.

The solution to Equation 2.16 is:

$$T_g(t_r^{'}) = \frac{T_0 \gamma\ e^{\gamma\ t_r^{'}}}{\left(\beta + T_0 \alpha\ e^{\gamma\ t_r^{'}}\right)} \tag{2.18}$$

where

$$\alpha = \frac{k_B Sh_T}{P_0 mVC_p},\ \ \gamma = T_0 \alpha + \beta \text{, and } \ \beta = \frac{k_B fP_{in}}{P_0 mVC_p} \tag{2.19}$$

If it is assumed that the temperature comes to a steady-state, then a steady-state gas temperature may be introduced to Equation 2.18. So, as $t_r^{'} \to \infty$, $T_g(t_r^{'}) \to T_{ss}$, where T_{ss} is the steady-state temperature of the gas. In this limit, the β term in

Equation 2.18 may be neglected, and T_g may be written as:

$$T_{ss} = \frac{T_0 \gamma\ e^{\gamma\ t_r^{'}}}{T_0 \alpha\ e^{\gamma\ t_r^{'}}} = \frac{\gamma}{\alpha} \tag{2.20}$$

Equation 2.16 may now be rewritten as:

$$\frac{1}{T_g} \frac{dT_g}{dt_r^{'}} = -\alpha(T_g - T_0) + \beta \tag{2.21}$$

And after multiplying both sides of the equation by T_g and including the steady-state temperature defined in Equation 2.20:

$$\frac{1}{T_g} \frac{dT_g}{dt_r^{'}} = \alpha(T_{ss} - T_g) \tag{2.22}$$

Using the new form of the equation, the solution may now be written as:

$$T_g(t_r^{'}) = \frac{T_0 T_{ss}\ e^{\alpha \mathrm{T_{ss}}\ t_r^{'}}}{\left(T_{ss} - T_0\right) + T_0\ e^{\alpha \mathrm{T_{ss}}\ t_r^{'}}} \tag{2.23}$$

This functional form of the time-dependent temperature applies to the temperature profile within the electric discharge discussed in this work. The Nusselt, N_u, number describes the relationship between convective heat transfer and conductive heat transfer. Nusselt values greater than 100 are indicative of turbulent flows. Therefore a value significantly less than 100 is suggestive of a flow operating in the laminar regime. For a cylindrical flow tube[24]:

$$Nu = \frac{h_T D}{k_T} \tag{2.24}$$

where D is the diameter of the flow tube, k_T is the thermal conductivity of the fluid, and h_T is the convective heat transfer coefficient. For all cylindrical flow tubes, the Nusselt number should equal approximately 4.364.[40] This analysis will play an important role in determining the time-dependent temperature of the gas flow.

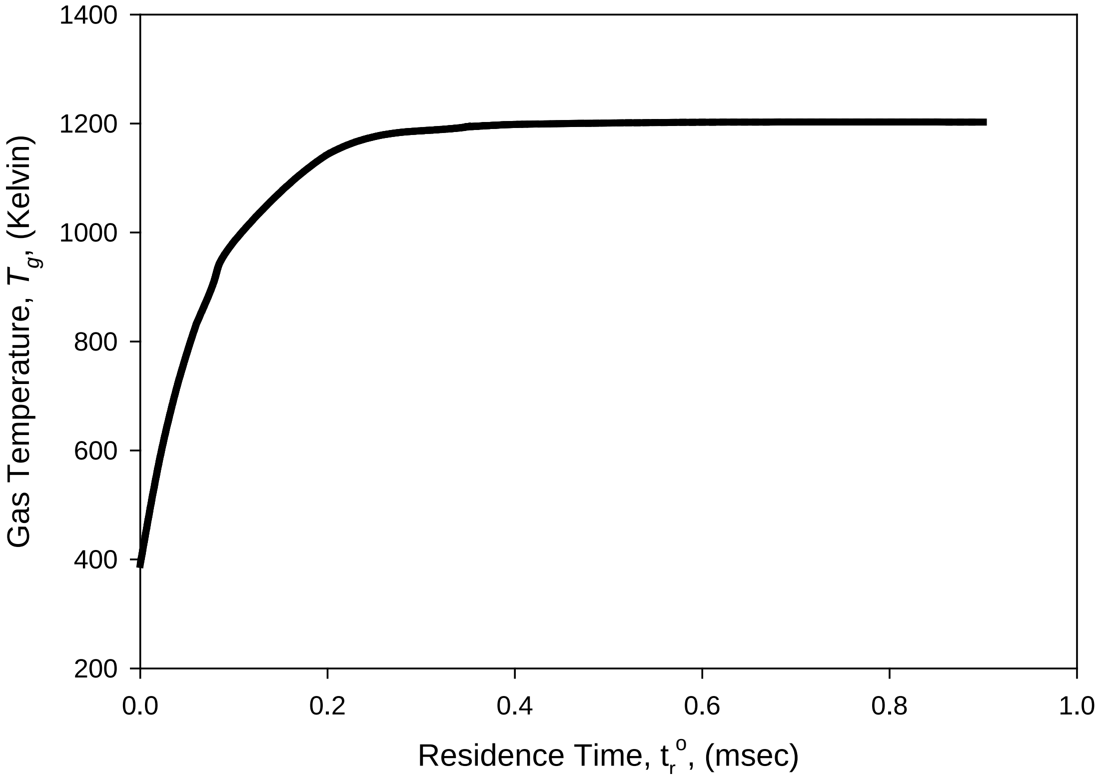

Figure 2.11 Temperature versus residence time.

In Figure 2.11, the functional form of the gas temperature (using Equation 2.18) is shown for oxygen gas flowing in a cylindrical tube and being heated via a capacitively coupled 100 W discharge. The x-axis in Figure 2.11 is the amount of time required for the gas to travel through the discharge region. This amount of time is nominally the length of the discharge divided by the velocity of the gas. Residence time will be discussed in greater detail in Section 4.2. The fraction of power coupled into gas heating is arbitrarily chosen to be 20%. As calculated in Appendix B, a significant amount of power is coupled into the formation of excited states within the gas flow; therefore, all the power does not need to be coupled into gas heating or lost via radiation. There are two important parameters to be extracted from this functional form. First is the initial slope of the curve, which is determined primarily by the strength of the heating term. Second is the steady-state temperature of the gas, which is the balance between the heating term and heat-loss term.

2.6 Determination of O-atom Concentrations Using Actinometry

The actinometry technique uses the emissions from the $O(3s\,^3S \rightarrow 3p\,^3P)$ transition at 844 nm and the $Ar(4s \rightarrow 4p)$ transition at 750 nm to determine the O-atom number density within an oxygen plasma.[41] Energy level diagrams for these two states are shown in Figure 2.12.

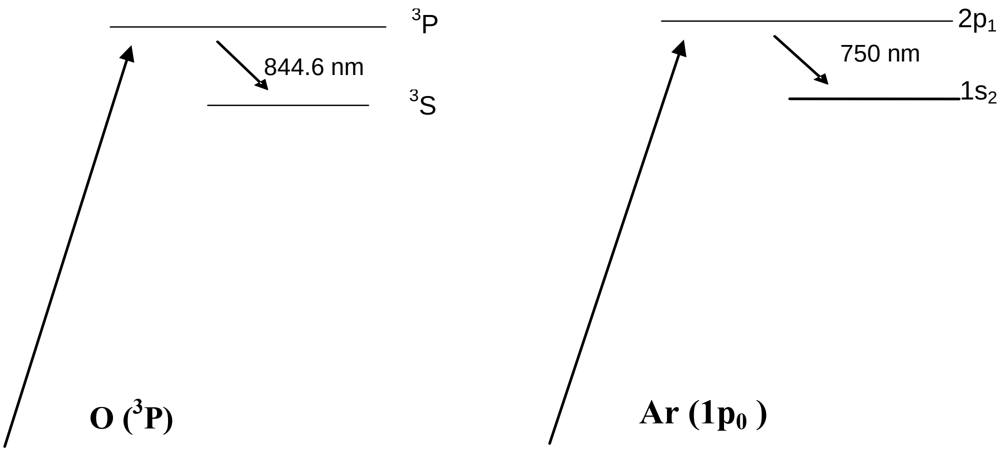

Figure 2.12 Schematic drawing of the energy levels involved in determining the concentration of the ground state oxygen atoms in the actinometery method.

It is assumed that the two main pathways of production of the $O(^3P)$ state are direct excitation by electrons and dissociative excitation, as shown below[38]:

$$\begin{aligned} &e^- + O(2p\ ^3P) \xrightarrow{k_e^O} O(3p\ ^3P) + e^- \\ &e^- + O_2(X,^3\Sigma) \xrightarrow{k_{de}} O(2p\ ^3P) + O(3p\ ^3P) + e^- \end{aligned} \tag{2.25}$$

where k_e^O is the rate coefficient for excitation of O-atoms from the ground state to the $O(^3P)$ state, and k_{de} is the rate coefficient for dissociation of molecular oxygen to two O-atoms [one excited to the $O(^3P)$ state].

It is assumed that the mechanism for excitation of $Ar(2p_1)$ is direct electron impact:

$$e^- + Ar(1p) \xrightarrow{k_e^{Ar}} Ar(2p_1) + e^- \tag{2.26}$$

where k_e^{Ar} is the rate of excitation from $Ar(1p \rightarrow 2p_1)$. As shown in Figure 2.13, the excitation cross-sections for the $Ar(2p_1)$ and $O(^3P)$ states are similar, which allows this method to determine the O-atom population from the argon emissions. The primary loss mechanism for these two excited states is radiative[38]:

$$\begin{aligned} &O(3p\ ^3P) \xrightarrow{\Sigma A_o} O(3s\ ^3S) + hv\ (844.6nm) \\ &Ar(2p1) \xrightarrow{\Sigma A_{Ar}} Ar(2p\ ) + hv\ (750.4nm) \end{aligned} \tag{2.27}$$

where ΣA_O and ΣA_{Ar} are the sum of all the radiative loss rates of the two excited states.

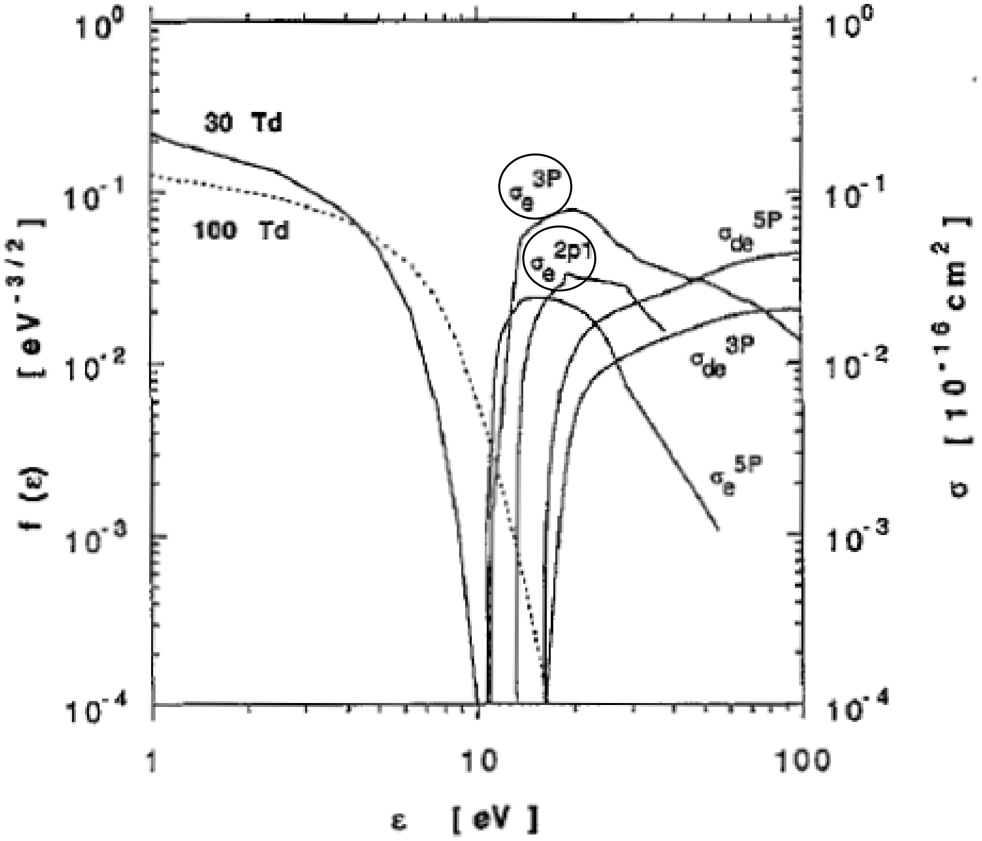

Figure 2.13 Cross-sections for electronic excitation of the O(^{3}P) and Ar(2p$_1$) states and reduced electron energy distribution at 30 and 100 Td.[38] Image taken from Pagnon et al.

Collisional relaxation with the ground state will slightly influence the actinometry results, so these reactions are accounted for in this analysis[38]:

$$\begin{aligned} O(3p\ ^3P) + O_2(X) &\xrightarrow{k_Q^O} O(2p\ ^3P) + O_2(X) \\ Ar(2p1) + O_2(X) &\xrightarrow{k_Q^{Ar}} \mathrm{Ar}(2p) + O_2(X) \end{aligned} \tag{2.28}$$

where k_Q^O is the rate coefficient for collisional relaxation of the $O(^3P)$ state by ground state oxygen, and k_Q^{Ar} is the rate coefficient for collisional relaxation of the $Ar(2p_1)$ state by collision with ground state oxygen. With all of these reactions considered, the intensity of the argon emissions and oxygen atom emissions are[38]:

$$
\begin{aligned}
I_{Ar} &= A_{Ar}\frac{\left[e^{-}\right]hv_{750nm}\left[Ar\right]k_e^{Ar}}{\Sigma A_{Ar}+\left[O_2(X)\right]k_Q^{Ar}} \\
I_O &= A_O\frac{\left[e^{-}\right]hv_{844nm}\left(\left[O\right]k_e^{O}+k_{de}\left[O_2(X)\right]\right)}{\Sigma A_O+\left[O_2(X)\right]k_Q^{O}}
\end{aligned}
\tag{2.29}
$$

where I_{Ar} is the intensity of the argon emissions, I_O is the intensity of the O-atoms, A_{Ar} is the Einstein A coefficient for argon, and A_O is the Einstein A coefficient for O-atoms. Therefore, the ratio of the measured emissions resulting from these two excited state takes the form of:

$$
\frac{I_o}{I_{Ar}}=\frac{hv_{844}A_o}{hv_{750}A_{Ar}}\frac{\left[O_2(X)\right]k_{de}}{\left[Ar\right]k_e^{Ar}}\frac{\Sigma A_{Ar}+\left[O_2(X)\right]k_Q^{Ar}}{\Sigma A_o+\left[O_2(X)\right]k_Q^{O}}
\tag{2.30}
$$

This relationship may also be written as:

$$
\frac{I_o}{I_{Ar}}=\frac{1}{C_{Ar}^{O}}\frac{\left[O\right]}{\left[O_2(X)\right]}
\tag{2.31}
$$

where[38]

$$
C_{Ar}^{O}=\frac{hv_{750}A_{Ar}}{hv_{844}A_O}\left(\frac{\left[O_2(X)\right]k_{de}}{\left[Ar\right]k_e^{Ar}}\right)^{-1}\left(\frac{\Sigma A_{Ar}+\left[O_2(X)\right]k_Q^{Ar}}{\Sigma A_o+\left[O_2(X)\right]k_Q^{O}}\right)^{-1}
\tag{2.32}
$$

From Equation 2.31, it may be seen that the ratio of the measured intensity of the 844 nm line and the 750 nm line is a constant value, C_{Ar}^{O}, multiplied by the ratio of

$[O]/[O_2(X)]$. The constant, as determined by Pagnon,[38] is 2.1 ± 0.15 x 10^{-3} with a 7% uncertainty for a given ratio of $[O]/[O_2(X)]$.[38] The Pagnon results are measured over a pressure range of 0.36 to 2 Torr and a discharge current of 5 to 80 mA.[38] Note that C_{Ar}^{O} is a function of the ratio of argon and molecular oxygen, as well as the E_{eff}/N of the discharge. The ratio of Ar/O_2 in the Pagnon study is 10^{-2}.[38] In this study, the ratio of argon to oxygen is 0.1. Therefore, the value of C_{Ar}^{O} is scaled by an order of magnitude to 2.1 x 10^{-2}, as dictated by the increase of the argon concentration. The determined values of C_{Ar}^{O} have an approximate 20% error associated with them. The actinometry method is well understood and widely applied for the detection of O-atoms in the presence of electrons.[42-54]

2.7 Operational EOIL System

Bernard and Pchelkin explored the production of $O_2(a)$ within an electric discharge in 1978.[2] Using a microwave discharge at 70 W and 450 mTorr, they reported a maximum $O_2(a)$ yield of 11%. This value is short of the 15% threshold for gain at room temperature. Also, work released by Schmiedberger, Takahashi, and Fuji in 2001[13] reports a maximum $O_2(a)$ yield of 30% over the E-field frequency range of 25 to 100 MHz. With a 30% yield, there should be a significant amount of extractable power; however, the reported maximum laser power is approximately 2 μ-watts, which is similar to power levels expected from florescence. The calibrated high-purity germanium (HPGe) detector, which they use to determine the Y_a, does not spectrally resolve the emissions. An unresolved spectrum is susceptible to corruption if there is another emitting species in the detected frequency range. Including emission intensities from other excited species, such as O-atoms, may explain the discrepancy between the reported $O_2(a)$ yield and laser power.

2.7.1 Work at the University of Illinois at Urbana-Champaign

In 2004, UIUC demonstrated the first operation of an EOIL device.[5] A schematic of the system is shown in Figure 2.14. The gas flow is made up of oxygen; helium, which is the carrier gas that comprises 83.55% of the gas flow; and trace amounts of NO in the flow (0.78%). NO and NO_2 are parasitic to O-atoms via a catalytic reaction. Therefore, including NO in the discharge decreases the amount of O-atoms that result from the discharge, while also serving as an electron donor to allow the discharge to be self-sustaining at an E/N of 10 Td. This E/N is ideal for the production of $O_2(a)$, as stated by Stafford and Kushner.[7] Introducing NO_2 in the gas flow downstream of the discharge serves two purposes according to the authors. Primarily NO_2 will further reduce the amount of O-atoms in the gas flow, by the catalytic reaction. Also the addition of a room temperature gas downstream of the discharge will cool the hot effluent from the discharge region. O-atoms quench the excited state of iodine responsible for lasing in the system, so reducing O-atom concentrations increases the steady-state value of the excited iodine state.[7] It is reported that, even though some O-atoms are helpful in dissociating I_2, too many will deactivate I*, which has a detrimental effect on laser performance.[3] In 2005, a maximum $O_2(a)$ yield of 17% was reported without the inclusion of NO_2 into the gas flow.[3] The maximum laser power of the system was 520 mW with an RF discharge coupling 400 W into the discharge. The operating conditions of the laser were a total pressure of 12.9 Torr with oxygen comprising 15.67% of the gas flow or a partial pressure of approximately 2 Torr.

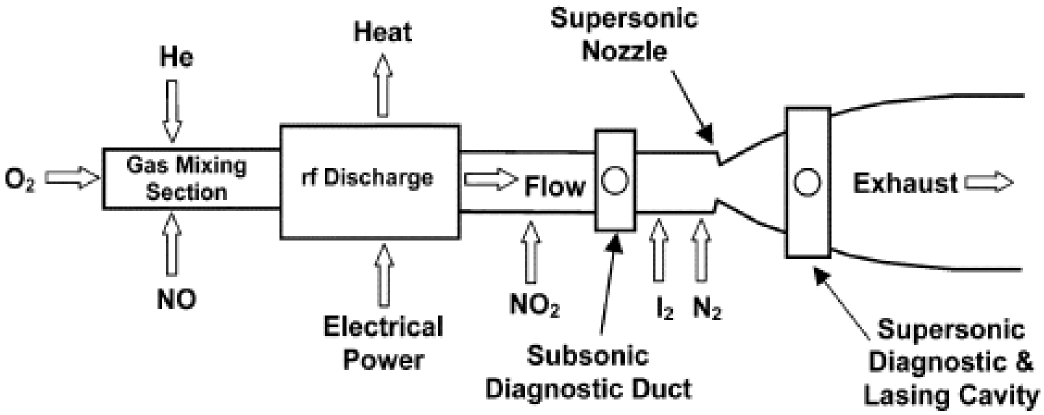

Figure 2.14 Schematic design of an electric discharge pumped oxygen-iodine laser demonstrated by the University of Illinois at Urbana-Champaign. Partial pressure of oxygen was 2 Torr in the flow and 520 mW laser power coupled out of the system. [3]

In January 2008, UIUC applied a 100 W RF discharge to predissociate the I_2 before it was injected into the gas flow.[55] Operating at a total pressure of 300 Torr, a mixture of He:O_2:NO at 50:10:0.05 was passed through a 700 W RF discharge. The pre-dissociation of the I_2 resulted in a gain of 0.067% cm^{-1} and a maximum laser power of 6 W. This report was followed closely by a report in which the primary discharge was changed from a single discharge in a gas flow tube with a radius of 4.9 cm to two flow tubes with radii of 1.6 cm. Each flow tube had power capacitively coupled into it using two 1,000 W RF discharges. Once again, the I_2 was pre-dissociated, using a 100 W RF discharge; the reported gain was 0.17% cm^{-1} with a maximum power of 12 W.[4]

2.7.2 Work by Alan Hill at Kirtland AFB

Alan Hill proposed a method for producing $O_2(a)$ with higher energy efficiency.[55] The major problems with electrically driven SOGs are that self-sustained discharges, operate at reduced electric fields that do not produce $O_2(a)$ efficiently, 20 – 40 Td. Therefore a large portion of the energy coupled into the discharge goes to the creation of excited species which are not $O_2(a)$ and instead result in heating the gas flow. Heating the gas is detrimental to an EOIL system in two ways. First, any power that is coupled into the temperature of the gas is not available for the production of $O_2(a)$. Second, the pooling reaction,

$$\left[O_2(a)\right]+\left[O_2(a)\right]\rightarrow\left[O_2(X)\right]+\left[O_2(b)\right], \tag{2.33}$$

increases exponentially with gas temperature.[7] So, not only is the energy used to heat the gas-wasted power, but it also decreases the amount of $O_2(a)$ created in these systems. It is possible for an outside source of electrons to sustain the discharge. Therefore, the E-field could be held at low levels that are ideal for the production of $O_2(a)$, and this would also keep the gas temperature low. Current results, using pre-ionization by UV radiation, with voltage pulses of ~150 Td, ~10-30 ns pulses at 50,000 pulses s^{-1}, and a DC E/N of ~10 Td promise: (1) singlet oxygen yields of 30%; (2) an electric excitation efficiency of 40%; (3) specific energy loading of 150 kJ/m O_2; and (4) a temperature increase of less than 125 K. Lasing from this system has not been reported yet.[57]

2.7.3 Work at The Ohio State University

Work at The Ohio State University (OSU) is based on using the pulser-sustainer method of maintaining a discharge first proposed by Hill.[58, 56] Typical glow discharges have two drawbacks, which are addressed by using pulser-sustainer systems. One is that the supersonic nozzles employed in EOIL systems require significant gas pressures upstream of the supersonic nozzle. Typical electric discharges in oxygen are not stable at these pressures. Pulser-sustainer methods establish stable discharges at high pressures. Secondly, the optimal E/N for the production of the $O_2(a)$ state is approximately 10 Td, which is significantly less than the E/N in which a typical oxygen discharge is sustainable.[7] By combining high-voltage pulses with a constant field of relatively low voltage, a pulser-sustainer is able to maintain an average E/N around 10 Td.[7] The frequency and power of the sustainer pulse is tailored to keep the discharge stable. In January 2007, OSU demonstrated a peak laser power of 0.28 W, using a pulser-sustainer SOG.[57] The gas flow was 15% O_2/85% He at a discharge pressure of 60 Torr and a discharge power of 1.55 kW. A maximum gain of 0.04% cm^{-1} was reported at the same conditions but at an 80 Torr discharge pressure. In June 2007, OSU implemented UIUC's technique and included NO in the gas flow through the discharge. Maximum laser power was reported at 1.24 W with a gain of 0.049% cm^{-1}.[10] The gas flow was reported as a 15% O_2/He mixture with 190 ppm I_2 and 550 ppm NO at a discharge pressure of 107 Torr and a discharge power of 2.4 kW. Both groups reported an increase in laser power by including NO in the gas flow through the discharge. Because the E/N in pulser-sustainer methods is already ideal for the production of $O_2(a)$, the increase in laser power may be attributed to the reduction in the quenching effect that O-atoms have on the I* density.

2.8 Scaling EOIL System

UIUC has shown that an EOIL will operate at laser powers up to 102.5 W.[64] The next step in the evolution of the EOIL weapon system is to show a path to scaling from 100 W to kW, as well as higher output energy systems. In oxygen-iodine laser systems the extractable power is determined by Y_a, as well as the number of $O_2(a)$ molecules in the system. In order to scale laser power from the current system to a feasible weapon system, the oxygen pressure in the cavity must be increased, while Y_a is held constant or increased. The historic results of this system suggest that accomplishing this power scaling may be problematic.

Figure 2.15 shows the results of both experiments, as well as computer models reported by many different research groups. A large parameter space is explored in these studies, including different buffer gases, E-field frequency oscillations, coupled discharge power, and discharge geometries.[2, 3, 12, 56, 59-63]

The general trend of the measured results shows a decrease in the achievable $O_2(a)$ yield as a function of the partial pressure of oxygen. There are three points shown in Figure 2.14 that break this trend. They are the results of △ Hill,[57] ○ Ionin,[62] and □ Naparitovich.[61] These three values are the result of computer models, implying that there may be a discrepancy between simulated and measured kinetics, which determine the value of $O_2(a)$ that is achievable within an oxygen glow discharge. Understanding this difference is important to determining the feasibility of using an electrically driven SOG within a weapon system.

The research group at UIUC has scaled the output power of an EOIL device by two orders of magnitude since first light was achieved in 2005.[64, 65] A number of different modifications have been made to the lasing system in order to increase output laser power. One significant change made by the research group at UIUC is the number of flow tubes passing through the discharge region. All of the flow tubes are combined after the discharge region before the iodine is injected into the gas flow.

By increasing the number of flow tubes, from one in 2008[55] to six in 2010,[64] the group has increased the volume of the laser resonant cavity, while maintaining a constant gain of approximately 0.26% cm^{-1}. It is of particular note that the number of discharge regions has been scaled, while holding the dimensions of the discharge region constant. This suggests the importance of the surface area to discharge volume and may be linked to gas kinetics governing the concentration of $O_2(a)$ within the discharge.

Recent publications have expressed the need to completely define the chemical kinetics that dominate excited state populations for EOIL devices.[65] Zimmerman et al. published a study on the effects of frequency and discharge geometry upon the discharge effluent.[66] It was found that the conditions favorable for $O_2(a)$ production involve reducing the flow tube diameter, while increasing the residence time to limit the O-atom concentrations.

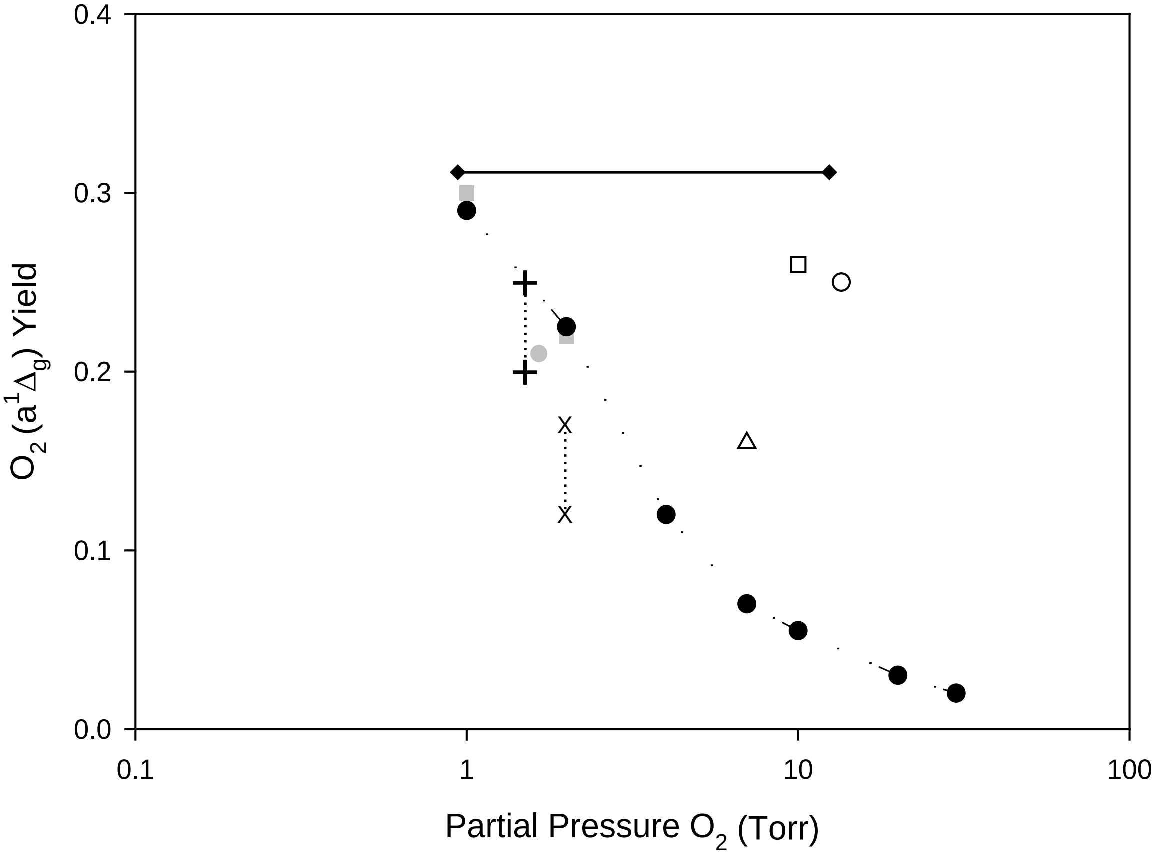

Figure 2.15 ■ Schmiedberg(RF)[12]; △Hill(Controlled Avalanch)[57]; ▲Rakimova(RF)[17]; ○ Ionin[62]; □ Naparitovich[61]; ▼ Pchelkin(1978 MW)[2]; ● Itami(1999 MW)[60]; ■ Savin[63]; x Carrol(RF)[3]; + Rawlins(2005 MW)[59]; ● Rakimova[16]; ◆ super-elastic theoretical limit.[16] Historical plot reporting the results of a number of different groups operating under various different pressures, power frequencies, discharge geometries. Both measured data and simulated data are reported.

By reducing the radius of the flow tubes the surface area to volume ratio of the discharge will be increased. Therefore the concentrations of any excited species that is primarily destroyed by collisions at the wall will be reduced. A paper by Davis et al. [67] discusses power scaling in a 1 to 5 kW supersonic discharge-flow reactor. While coupling 1 to 5 kW of power via a microwave discharge into a gas flow, it was found that the quenching of I* by O-atoms is not fast enough to explain the loss of excited species within the gas flow. This result points to a destruction mechanism which is other than direct collisions with O-atoms. Lee et al. presented a study of catalytically produced

$O_2(a)$ by using the flux of O-atoms that result from the discharge.[68] In this work an iodine oxide catalyst is applied to the walls of the flow tube downstream of the discharge region. Results suggest that the O-atoms created within the discharge region react at the walls producing $O_2(a)$. Other excited species, such as vibrationally or electrically excited O_2 and O_3, may also be involved in the catalysis at the wall.[68] A 2010 publication by Azyazov et al.[69] suggested that the production of vibrationally excited ozone is significant in plasmas with an excess of ground state oxygen. This study argues that including this mechanism renders including the three-body reaction (reaction 24) unnecessary to reproduce measured $\left[O_2(a)\right]$. Recent publications by the EOIL community have established the need for a greater understanding of the governing kinetics involved in EOIL devices to allow scaling to kW laser powers.

III Equipment

The apparatus is designed to study the behavior of an electric discharge-driven SOG. A glow discharge is created by flowing pure oxygen contained in a glass flow tube through an intense electric field. Oscillating electric fields are used at a microwave frequency of 2.45 GHz and a radio frequency of 13.56 MHz. Emissions from the excited states of $O_2(a)$, $O_2(b)$, and various O-atom emissions are used to characterize the discharge. Absolute concentrations of O-atoms are determined using the actinometry technique by comparing O-atom emissions to atomic argon emissions.

3.1 Microwave Discharge

A microwave discharge operating at 2.45 GHz sustains the glow discharge of a pure oxygen gas flow in a Pyrex tube. This apparatus is shown in Figure 3.1.

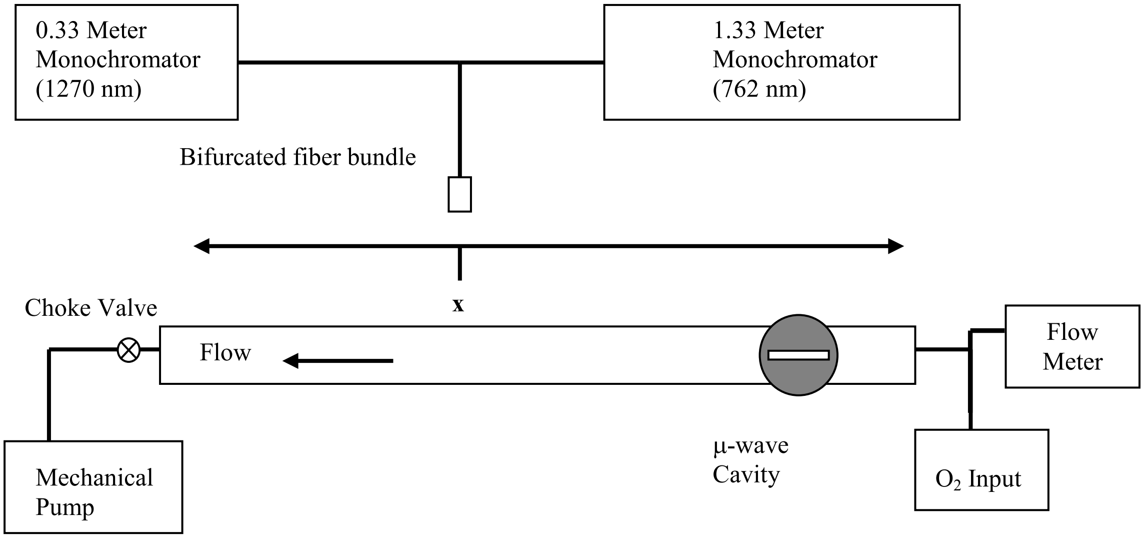

Figure 3.1 Schematic of the glow discharge apparatus.

The flow tube has an outer diameter of 1 cm and an inner diameter of 0.8 cm. With the use of a bifurcated optical bundle, the emissions from both singlet states are collected simultaneously at a given spatial location within the discharge and in the discharge afterglow. The fiber is located at the center of the discharge region and emissions are collected for an integration time of two minutes. The observation region of the collimated optics is approximately one cm in diameter. The discharge region in this study is also one cm in diameter and averages about 3 cm long; therefore, the optics gather light from roughly one third of the discharge region. In order to measure the changes in the excited species as a function of residence time within the discharge the flow velocity of the gas is varied. The emissions are spectrally resolved, and the intensity is determined by summing the emissions for each wavelength range. For the $O_2(b)$ emissions, the wavelength range is 761 nm to 768 nm, and for $O_2(a)$ is 1,240 nm to 1,275 nm. Two spectrometers are employed.

A Roper Scientific InGaAs detector array, attached to a 0.33 meter McPherson spectrometer equipped with a 600 grooves/mm grating blazing at 1,250 nm, is used to observe the emissions from $O_2(a)$ centered at 1,272 nm. The slit width of the monochromator is 250 μm, resulting in a spectral resolution of approximately 1.7 nm. The InGaAs array is cryogenically cooled to approximately -100° C. Also, a Roper Scientific intensified charged-coupled device (CCD) array, attached to a 1.33 meter McPherson spectrometer equipped with a 2,400 grooves/mm grating blazing at 700 nm, is used to observe the $O_2(b)$ emissions centered at 762 nm. The slit width is 10 μm, which yields a resolution of approximately 0.01 nm. The spectral resolution of the emissions allows the removal of interference of other emitting species within the spectral band of the excited state emissions. The total intensity of the emissions is determined by summing the molecular emissions of the appropriate frequency range: 761 to 768 nm for $O_2(b)$ and 1,240 to 1,275 nm for $O_2(a)$.

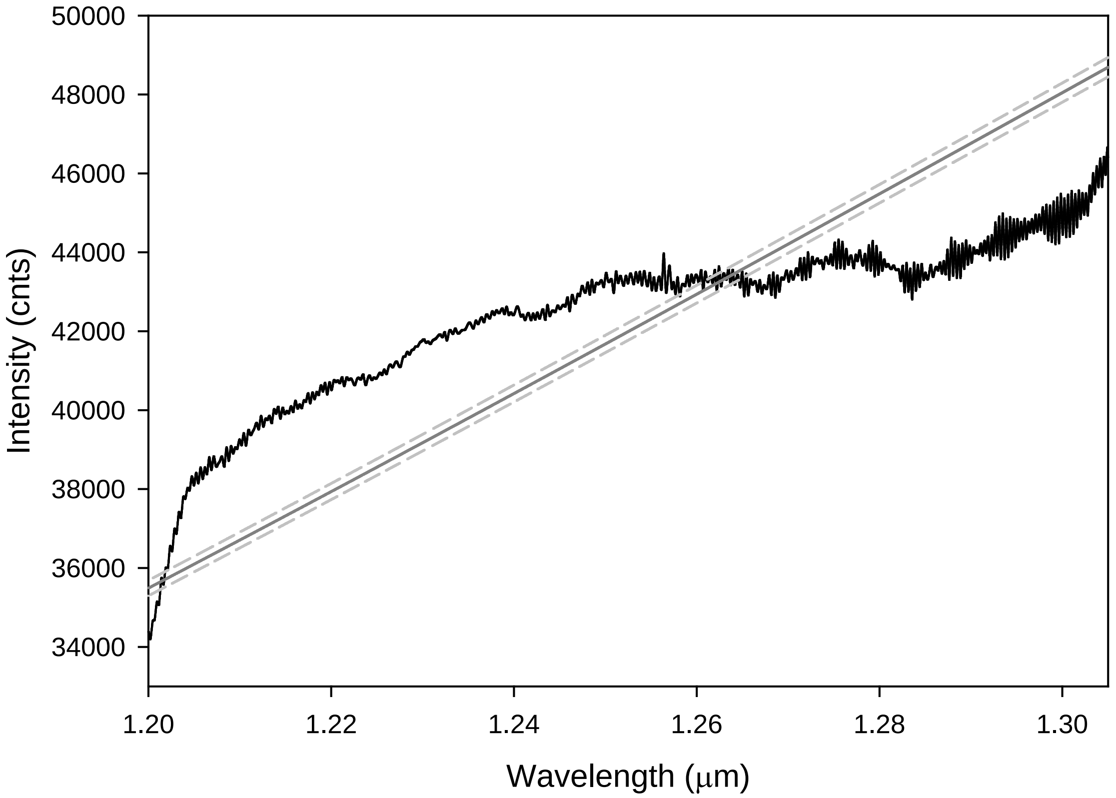

Figure 3.2 Comparison of the (—) theoretical black body ± 1K to the (—) experimental black body.

The detectivity of both detectors is a function of the wavelength of the light being detected. This dependence is determined using a black body light source for calibration. The emissions of a 1,000° K black body are measured and compared to the theoretical intensities. The gratings are positioned to center the desired wavelengths upon the detector arrays. The emissions from the black body, as detected by the InGaAs array, are shown in Figure 3.2.

The theoretical calculation includes an uncertainty of plus or minus 1° K. The ratios of the measured and theoretical values are the detectivity factor, shown in Figure 3.3.

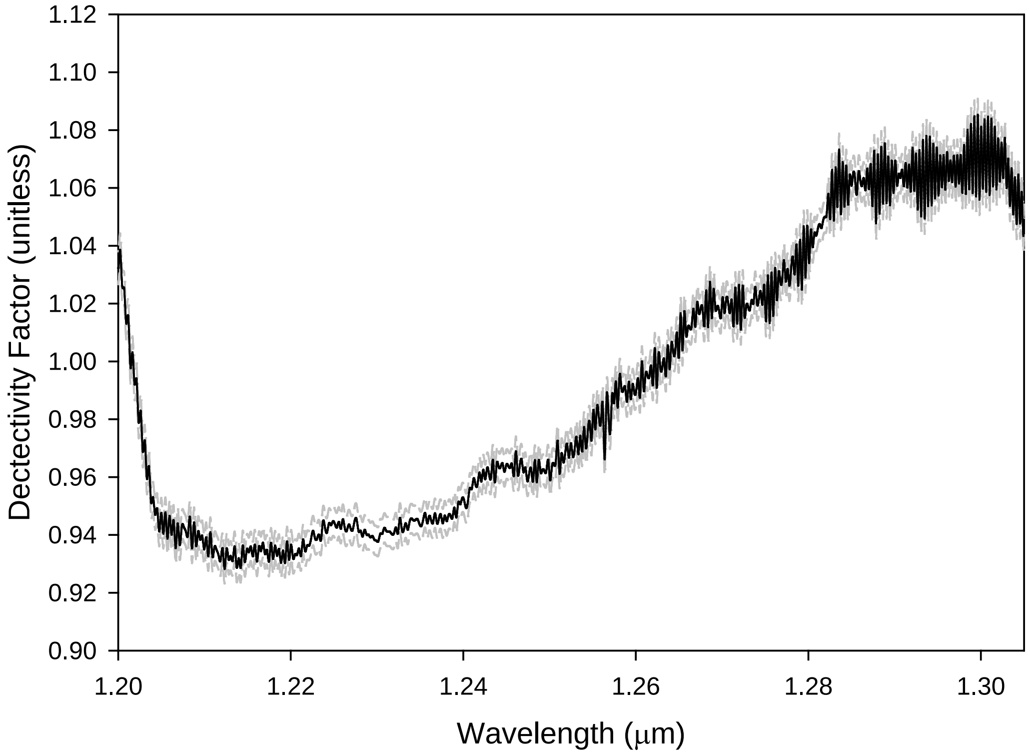

Figure 3.3 The detectivity factor of the InGaAs array used to measure the *$O_2(a)$* emissions from the discharge.

The dark current of the InGaAs array has structure; therefore, it is important to be careful when subtracting the dark current signal from the measured emissions. The dark current is measured over the two-minute integration time and subtracted from the measurements, as shown in Figure 3.4. The pixel-by-pixel change in dark current is not wavelength-dependent and is confirmed to be typical by the manufacturer of the detector array.

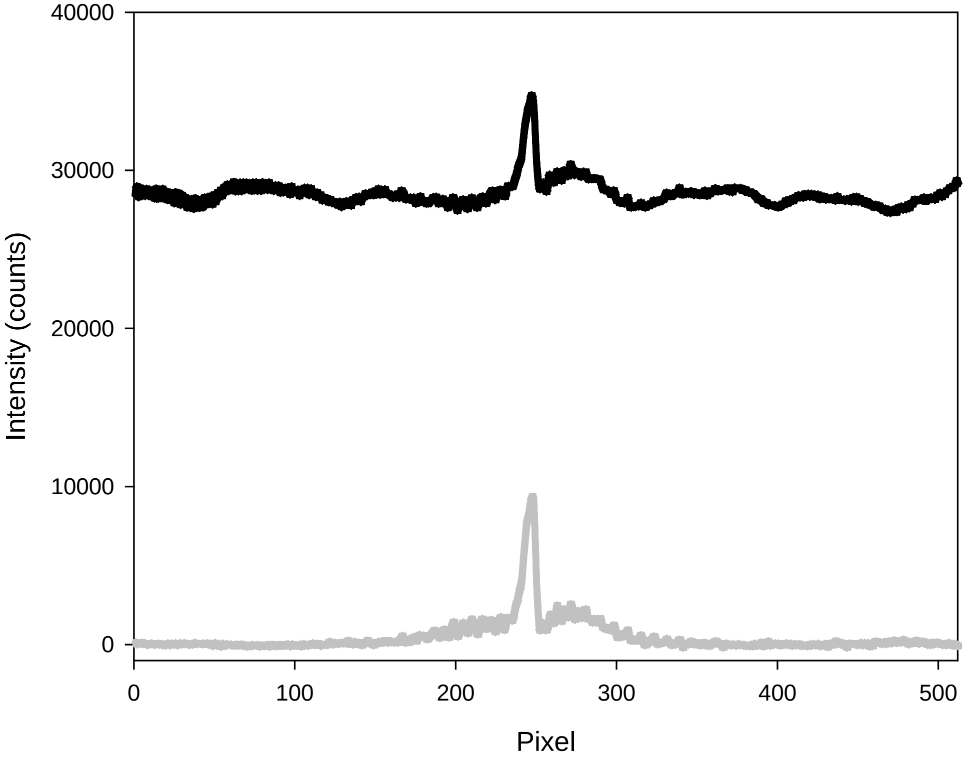

Figure 3.4 Subtraction of dark current from the measured intensity. ▬ raw data ▬ data after background subtraction.

An isolated atomic oxygen peak is used to calibrate the resolution of the spectrometer. In Figure 3.5, the resolution of the system is determined by fitting a sum of Gaussian peaks to the measured emission from the ^5F-^3D atomic emission at 1,257 nm. The asymmetry in the peak is due to a slight misalignment of the detector and grating. The calibration of the pixel number to wavelength is established by the spectrum itself. The fit for the 1.33 meter spectrometer is 0.00717 nm/pixel, and the fit for the 0.33 meter spectrometer is 1.925 nm/pixel.

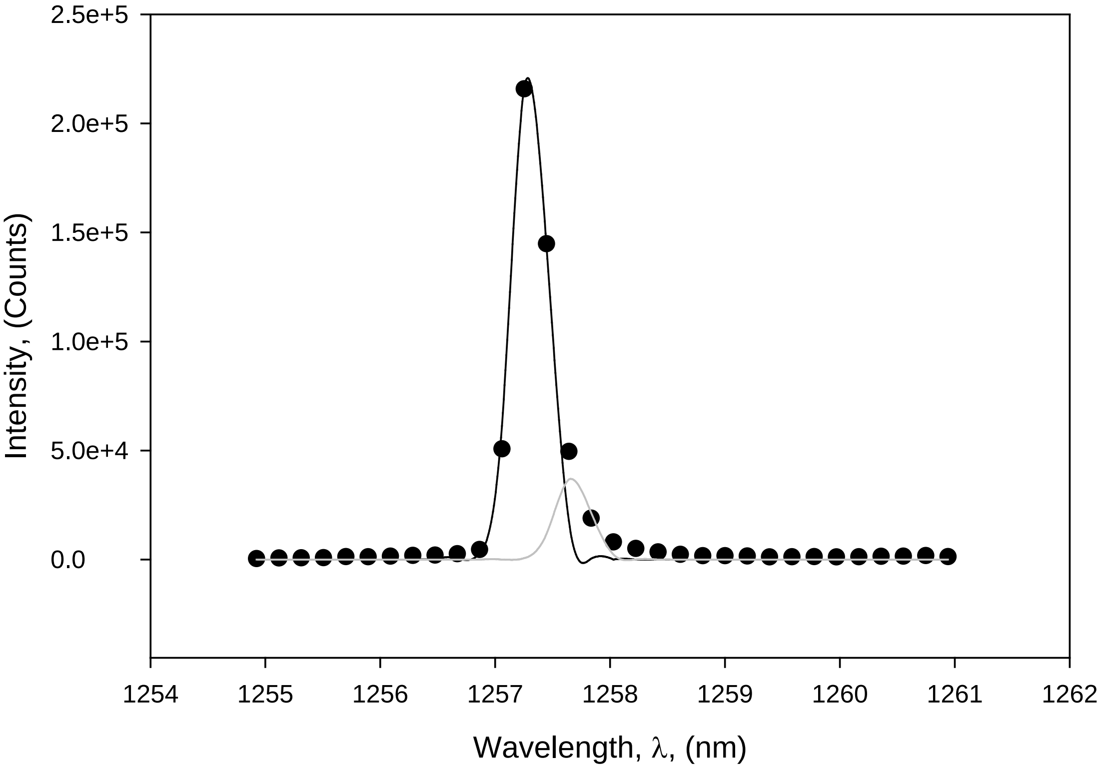

Figure 3.5 The ^5F-^3D atomic emission at 1,257 nm is used to determine the resolution of the 0.33 m monochromator used to monitor *$O_2(a)$* emissions. Resolution is determined to be 0.15 nm. Peak is a sum of two Gaussian peaks.

Emissions from both the $O_2(a,b)$ states are observed simultaneously, using a bifurcated fiber bundle. A 1 cm diameter collimating lens is positioned on the end of the bundle. The acceptance angle of the fiber is 68 degrees. Combined with the aperture stop, this determines a spatial resolution of 0.5 cm. The fiber bundle is positioned perpendicular to the flow tube and mounted on a sliding mount, allowing for parallel displacement along the flow tube. The focusing lens is located 1.5 mm from the edge of the Pyrex flow tube to maximize the spatial resolution.

The physical dimensions of the discharge are determined by the point at which the plasma begins to glow and where it stops glowing. The discharge glow is used as an indication of electron density, and the point at which it terminates indicates the lack of electrons in the gas flow. The length of the discharge plays a role in the power loading as well as the residence time of the gas.

The plasma typically terminates a couple of millimeters outside of the μ-wave cavity; however, at low pressures and flow velocities, the length of the discharge region extends beyond the dimensions of the cavity. The variation in the plasma dimension as a function of mass flow rate is shown in Figure 3.6 for a number of different pressures.

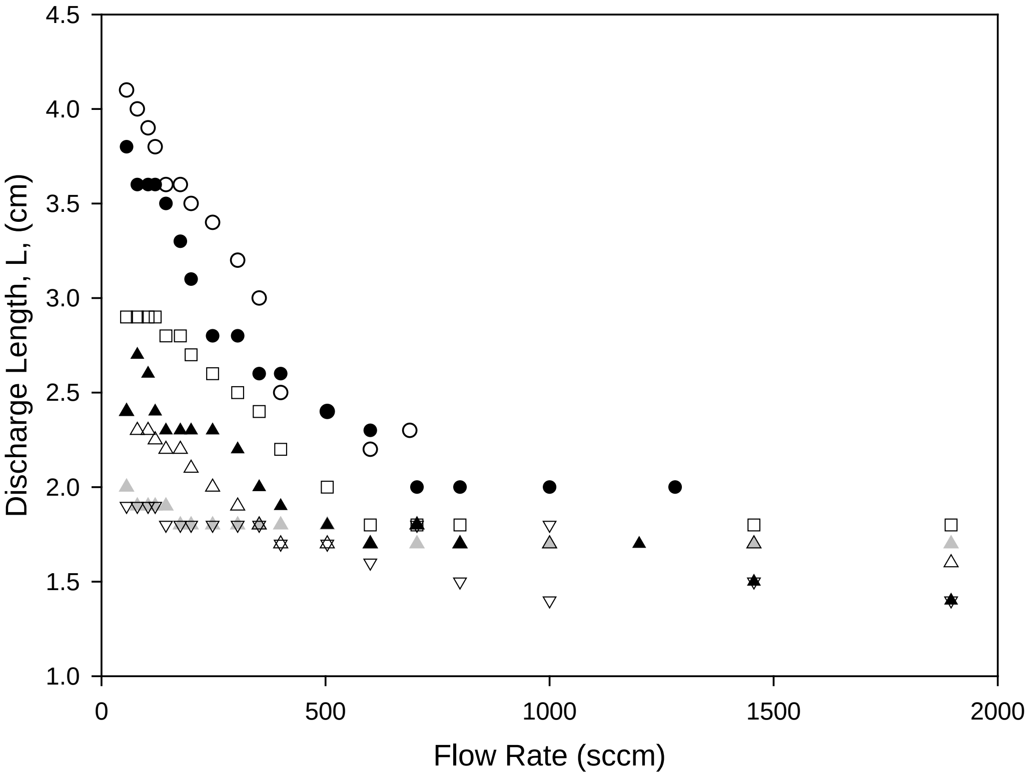

Figure 3.6 The length of the discharge as mass flow rate changes. ○ 2 Torr, ● 3 Torr, ☐ 4 Torr, ▲ 5.2 Torr, △ 6.4 Torr, ▲ 7.5 Torr, ▽ 8.6 Torr.

The flow rate of the input gases is controlled using a Sierra Series 840 Side-Trak Mass Flow Controller calibrated to control nitrogen from 0 to 2,000 SCCM with a resolution of

8 SCCM. For the calculation of residence for the temperature measurements included in this document these pressure and flow rate lengths are used. For the discharge volume calculation included in Chapter 4, an average value for discharge length of 3 cm is used in for calculations throughout this work.

The pressure is measured using an MKS, Model 690A, 10 Torr, Capacitance Manometer. The lowest achievable pressure is less than 1x10^{-3} Torr, which is beyond the range of the head. The vacuum pump is an Alcatel 2063C2 rotary vane pump. An Evenson cavity operating at 2.45 GHz with a range of 0 to 100 W controlled by an Opthos power supply is employed to produce the glow discharge in the gas flow.

Figure 3.7 shows the velocity versus the mass flow rate of the gas at a pressure of 4 Torr.

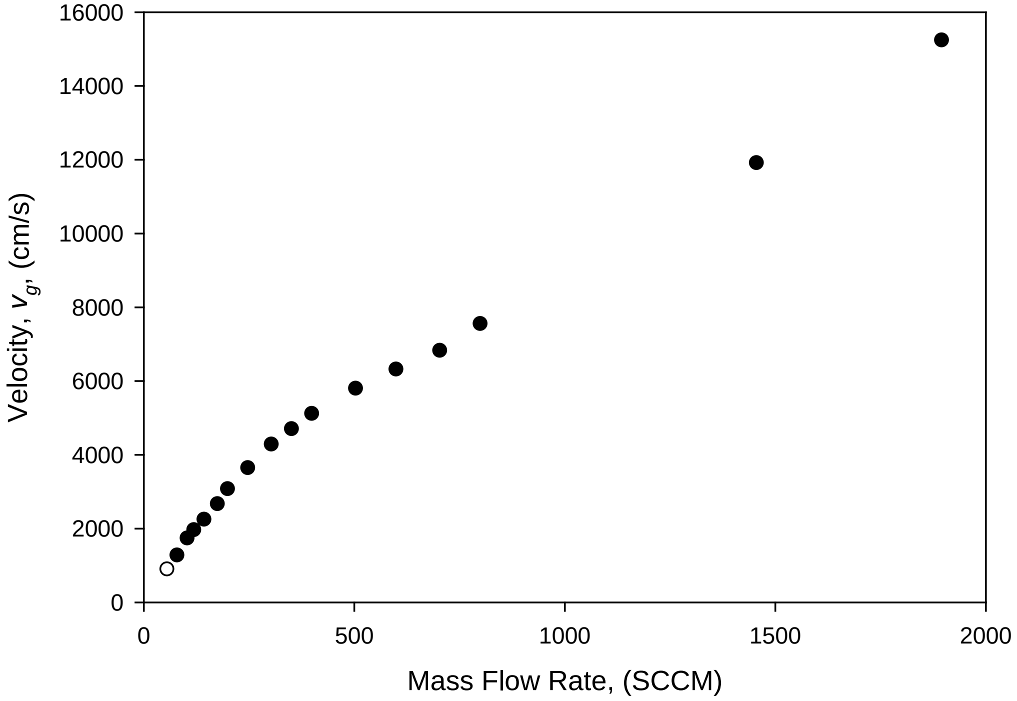

Figure 3.7 Velocity as a function of mass flow rate at 4 Torr.

Figure 3.7 shows that the gas velocity ranges from 800 to 15,000 cm/s, while the mass flow rate ranges from 2 to 2,000 SCCM. The gas flow is adjusted by the throttle valve to maintain a certain pressure (in the case of Figure 3.7, 4 Torr).

3.2 RF Discharge

Using an RF electric field to maintain the electric discharge is very similar to the microwave approach. The field is coupled into the gas by two copper rings positioned 10 cm apart with a width of 1 cm. The RF generator is a Dressler Cesar 1310 operating at 13.56 MHz with a power ranging from 0 to 1,000 W. The RF power generator is matched to the plasma flow tube using a VarioMatch matching network supplied by Dressler. The auto-matching network is calibrated for frequency ranges from 13 to 27 MHz and up to 1 to 1.5 kW, depending on the frequency of the field oscillations. A schematic of the RF discharge experiment is shown in Figure 3.8.

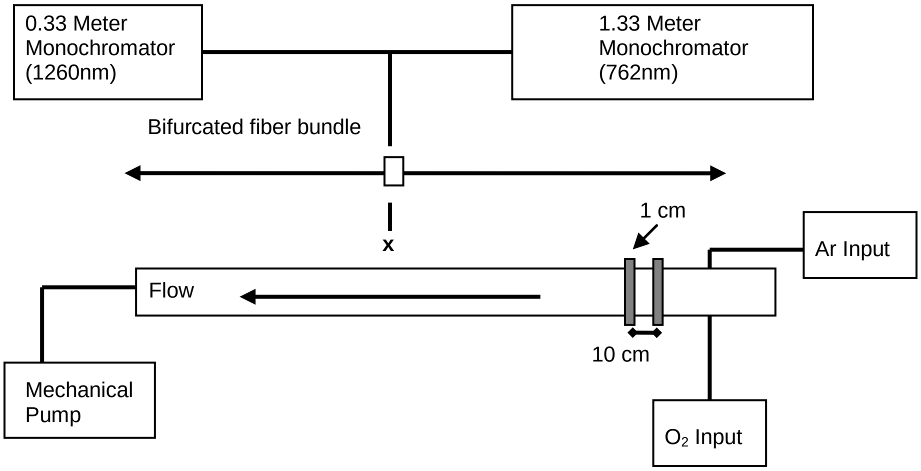

Figure 3.8 Schematic of the RF glow discharge apparatus.

The 1.33 and 0.33 meter monochromators used in the RF experimental apparatus are the same as those used in the microwave experiment. Therefore, their calibration and resolution are measured and performed with the same results as reported in Section 3.1. The argon inserted into the gas flow is used to monitor the O-atom concentrations via the actinometry technique, which was explained in Section 2.6.

IV Results

4.1 $O_2(b)$ Spectrum and Gas Temperature Measurement

The rotational spectra of the $O_2(b^1\Sigma \rightarrow X^3\Sigma)$ (0,0) and (1,1) bands near 762 nm are shown in Figure 4.1. Only the even number J values are observed due to the selection rules discussed in Section 2.4.2. The spectral resolution of the reported $O_2(b)$ emissions is slightly better than the results currently in the literature, which generally have a spectral resolution of 0.04 nm or greater.[15]

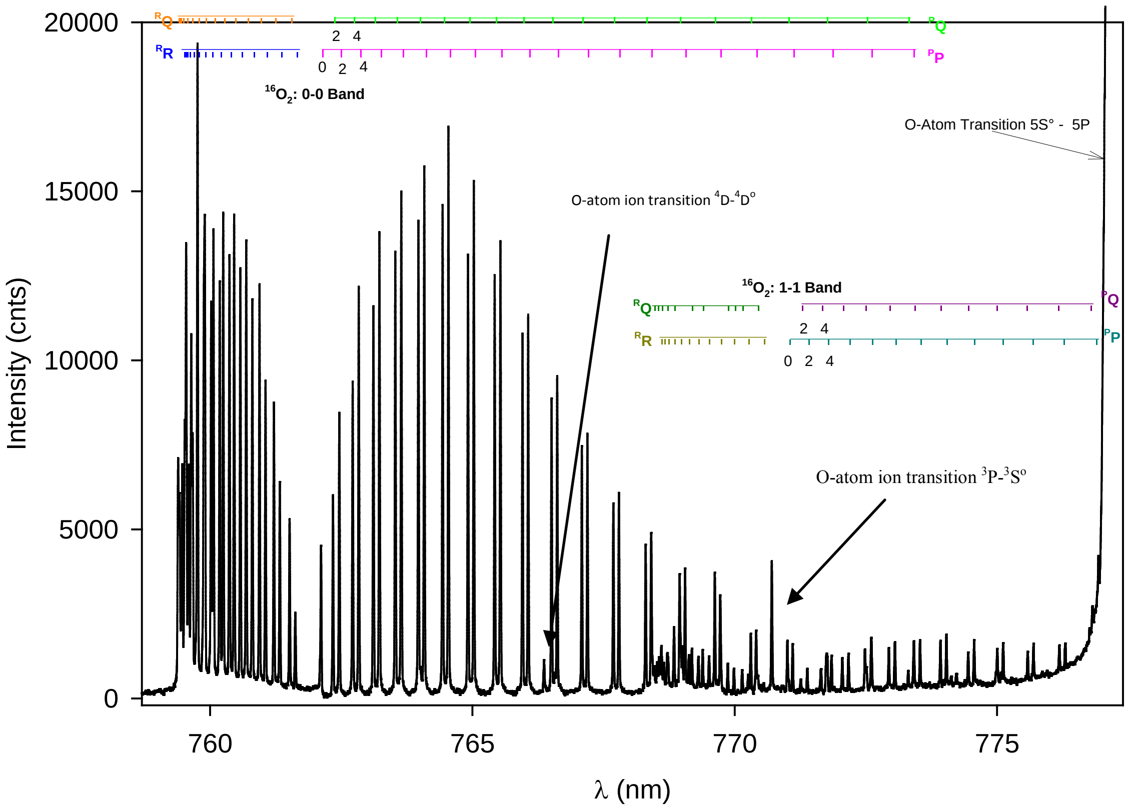

Figure 4.1 The emission spectrum of the $O_2(b)$ excited state, inside the μ-wave discharge, 4 Torr, flow velocity of 20 m/s, measured using the 1.33 meter spectrometer.

This added resolution permits the observation of the atomic emissions from the O-atom ion transition (^4D-$^4D^o$) at 766 nm; O-atom ion transition (^{3}P-^{3}S^o) at 771 nm; and $O_2(b)$ (1-1) band centered at 771 nm. Clear identification of these emissions permits the extraction of their contributions from the measured intensities and results in a greater certainty of the temperature measurements reported in this work.

The ^RQ, ^RR, ^PQ, and ^PP branches are readily observed and assigned in Figure 4.1. The emissions from $O(^5S \rightarrow {}^5P)$ around 777 nm are observed at the far end of this spectrum. The (1-1) emissions centered on 771 nm are also observed. The lifetime of the $O_2(b)$ state is about 1.1 s, allowing the nascent distribution to be collisionally relaxed. Therefore, it is possible to measure the gas temperature by measuring the molecular rotational temperature.

Figure 4.2 illustrates the statistical distribution of emission intensity versus the rotational energy of the excited state. The highly linear nature in Figure 4.2 exhibits the statistical nature of the emissions, arguing that the reported rotational temperatures will be representative of the gas temperature. As discussed in Section 2.4.2, Equation 2.4, the slope of this line is used to extract the rotational temperature of the $O_2(b)$ (0-0) excited state. The intensities are obtained from a fit to the area of a Gaussian lineshape. The reported I_b is the peak intensity of the Gaussian fit, while the width of all the peaks are held constant.

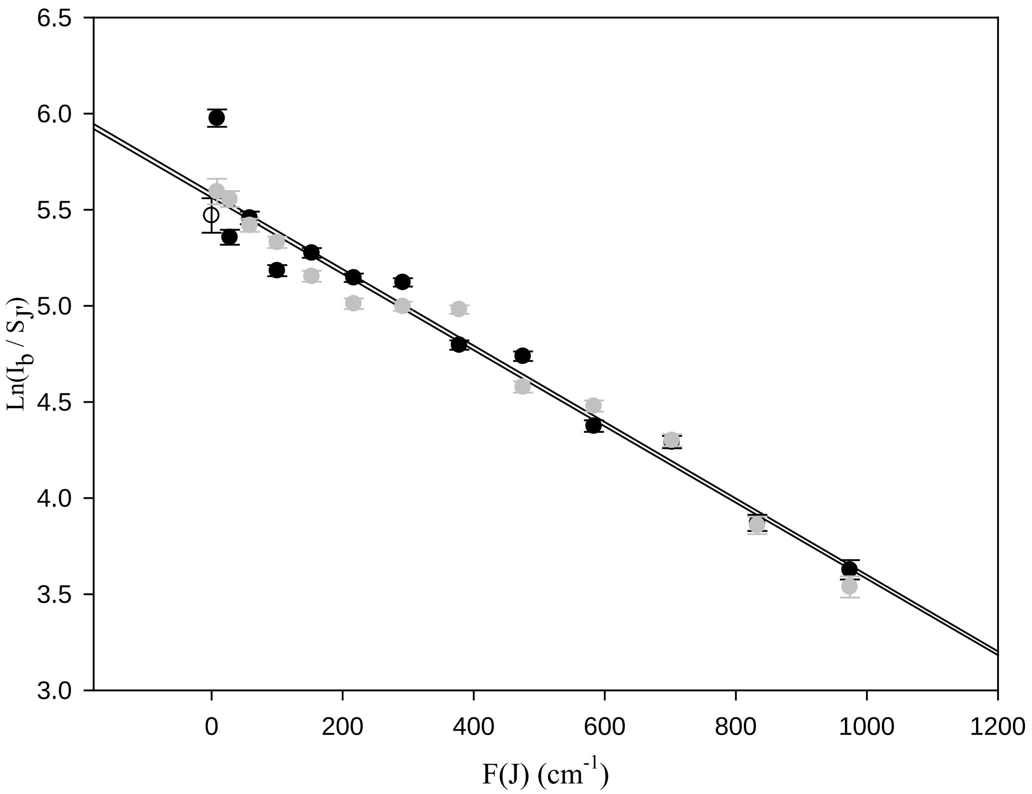

Figure 4.2 Natural log plot of emissions from $O_2(b)$ (0,0) state plotted versus energy used to extract gas temperature from emissions. ● are the ^{P}P branch and ● are the ^{P}Q branch.

The error bounds represent the uncertainties in the fit areas, as generated by the PeakFit program,[86] which is typically 0.01%. Several gas temperatures have been previously reported in the literature,[3, 7, 15, 17, 18, 70, 71] with extracted temperatures of T_g = 400 to 1,300 K and uncertainties of ΔT = 20 to 61 K. The integrated intensity of the $O_2(b\text{-}X)$ (1,1) band of Figure 4.1, relative to the (0,0) band, is 9.2 +/- 0.3 %, corresponding to a vibrational temperature of 896 ± 35 K. Both the ^{P}P and ^{P}Q branches yield similar temperatures; T_g = 720 ▯ 19 and T_g = 721 ▯ 20. Gas temperature plays an important role in emission intensity and is discussed further in Section 4.2.

4.2 Gas Flow Velocity and Residence Time

The gas temperatures, T_g, measured at the midpoint of the discharge as a function of oxygen flow rate and pressure are shown in Figure 4.3. Note the oxygen flow rate may be changed independent of pressure by throttling the pump valve. The measurements reported in Figure 4.3 are for a microwave frequency discharge with a 100% oxygen gas flow.

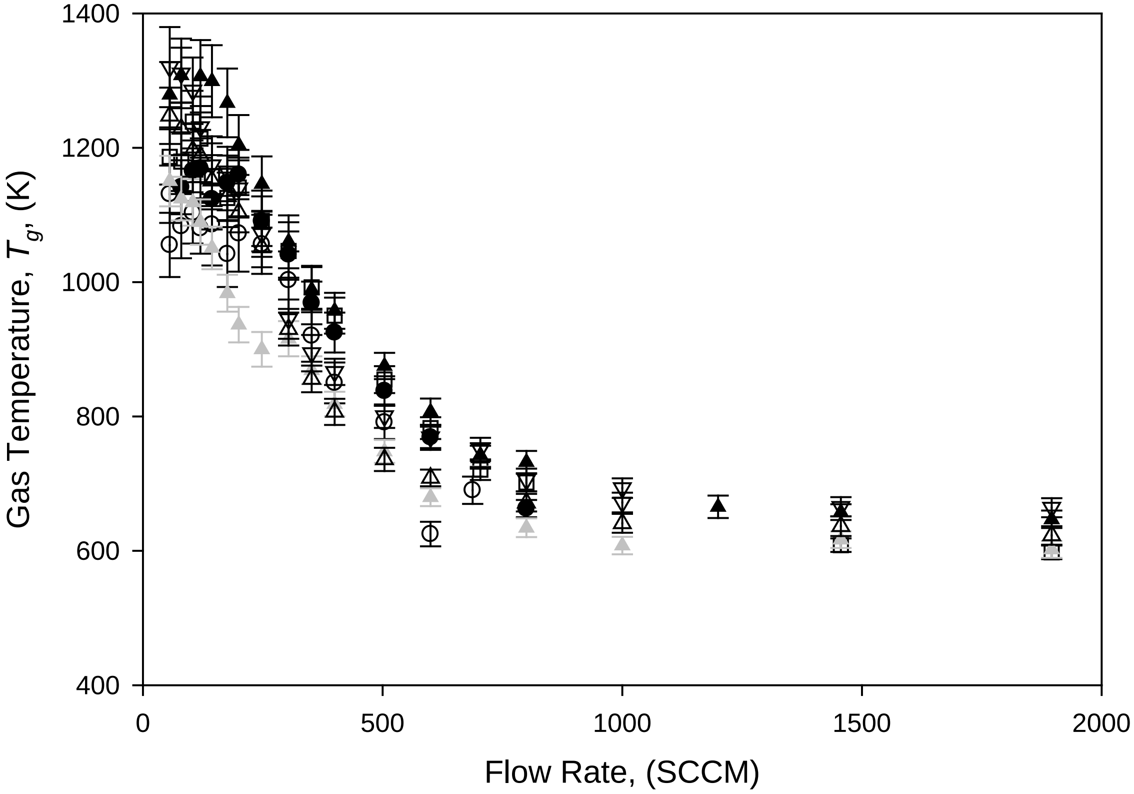

Figure 4.3 Gas temperature as a function of flow rate: ○ 2 Torr, ● 3 Torr, □ 4 Torr, ▲ 5.2 Torr, △ 6.4 Torr, ▲ 7.5 Torr, ▽ 8.6 Torr.

The gas temperature, T_g, decreases significantly from approximately 1,000 K to 600 K as the flow rate increases. However, the gas temperature appears to increase slightly as a function of pressure. As discussed in Section 2.5, flow rate may be converted to a velocity, given the flow tube geometry, gas temperature, and gas pressure. If it is assumed that the velocity of the gas is a constant throughout its travel through the discharge region, the time that the gas spends within the discharge is:

$$\frac{l}{v_g} = t_r^o \tag{4.1}$$

where l is the length of the discharge region, v_g is the velocity of the gas flow, and t_r^o is the amount of time the gas resides within the discharge.

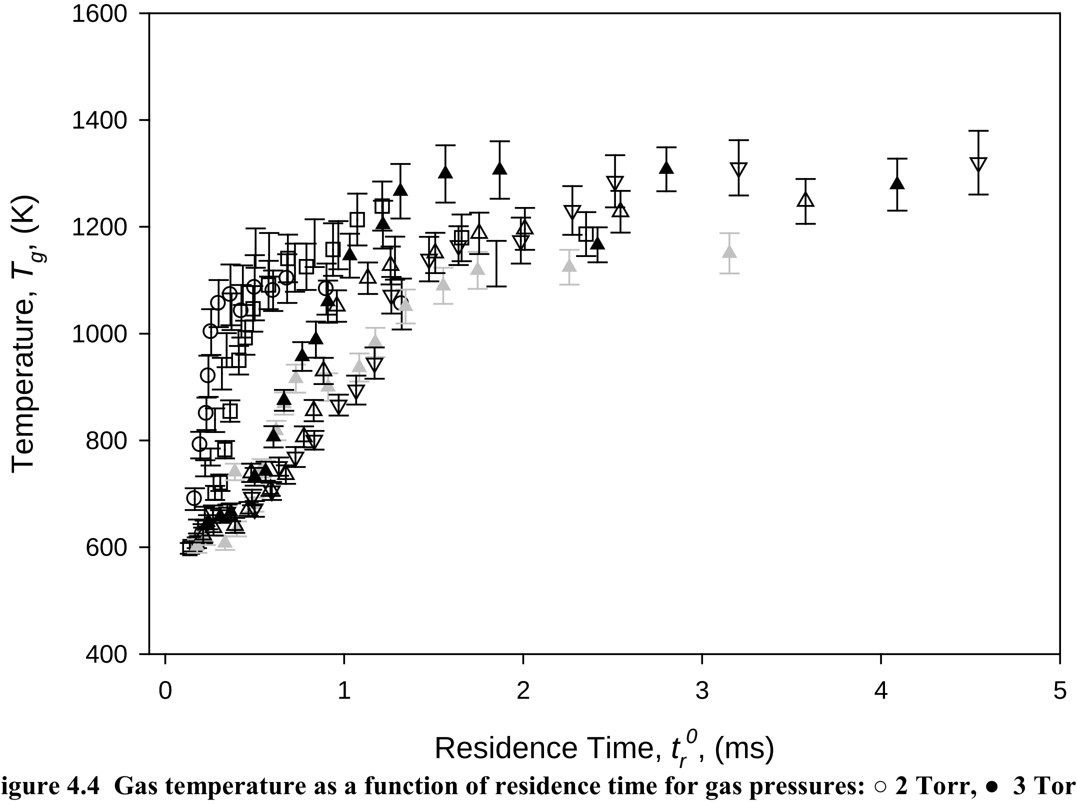

Figure 4.4 Gas temperature as a function of residence time for gas pressures: ○ 2 Torr, ● 3 Torr, ☐ 4 Torr, ▲ 5.2 Torr, △ 6.4 Torr, ▲ 7.5 Torr, ▽ 8.6 Torr.

The validity of the constant velocity assumption is discussed further in Section 4.3.1. The length of the discharge changes at different temperatures and mass flow rates; so, the length is measured in the lab and varies from 2 to 4 cm.

T_g as a function of residence time is shown in Figure 4.4. The gas temperature increases dramatically when the gas enters the discharge, changing from room temperature to 1,200 K in one millisecond. It then comes to a steady-state. As discussed in Section 2.5, it is appropriate to map residence time to a pressure normalized time, $t_r^{'}$, which collapses the pressure dependence of the data. The effect of this mapping is shown in Figure 4.5.

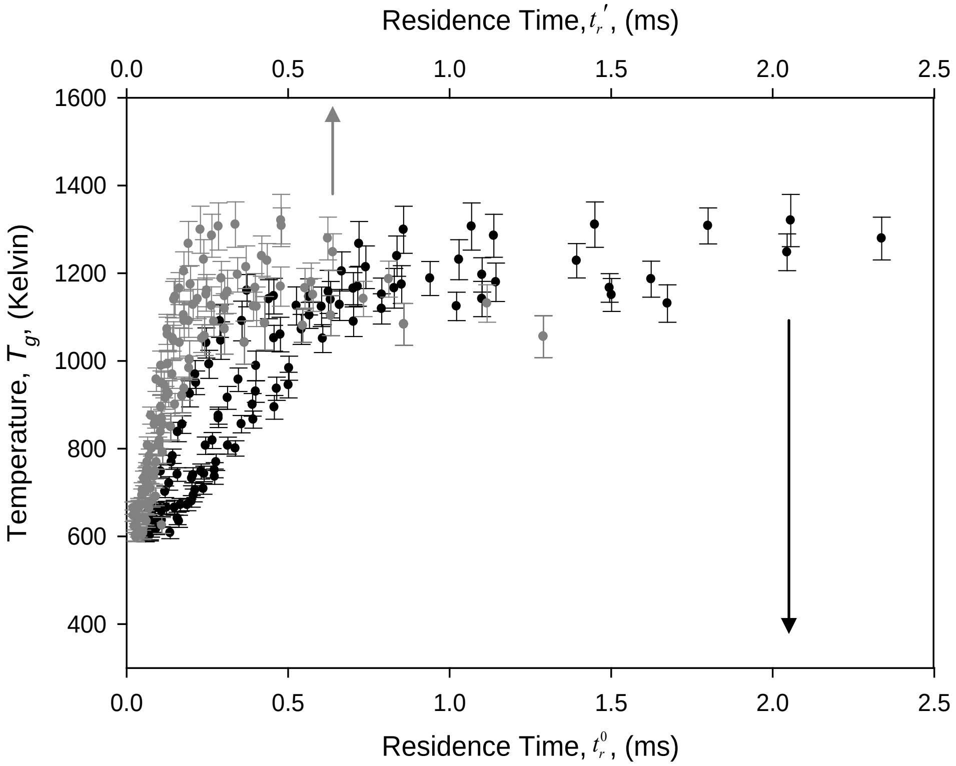

Figure 4.5 The gas temperature as a function of the ● residence time, t_r^0, lower axis and ● pressure normalized time, t_r', upper axis.

The collapse of the temperature profiles using a pressure normalized time argues for using a pressure-independent temperature profile, as derived in Section 2.5, Equation 2.18. This theory is used throughout the remainder of this work. The velocity calculations and, hence, the residence times have been calculated assuming the gas temperature is constant. Using the temperature profile, the effects upon gas velocity and resonance time will now be explored.

4.3 Effects of Time-Dependent Temperature

The pressure gradient in the flow tube is not large enough to affect the number density within the gas flow, < 0.1 Torr m^{-1}. So, the pressure is assumed to be constant along the length of the flow tube. A schematic of a flow tube with a discharge beginning at position x_0 and ending at position x_1 is shown below.

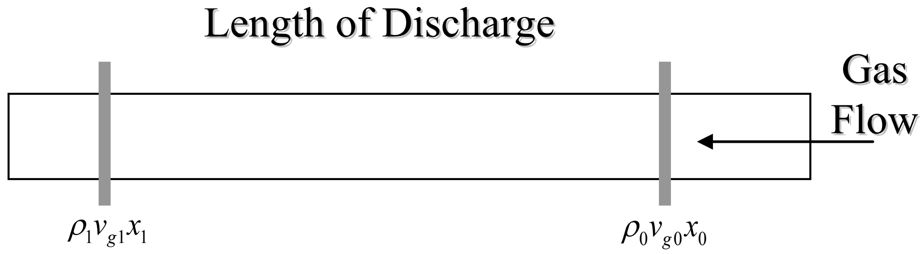

Figure 4.6 Schematic of a gas flow tube with positions 0 and 1 indicated.

According to mass conservation, if the gas density, ρ, changes, then the velocity, v_g, must change. Therefore, when discussing populations as a function of time, the temporal axis is a function of the flow velocity, which is a function of the gas temperature. The relationship between length, flow velocity, and residence time is:

$$\frac{dx}{dt} = v_g(t) \Rightarrow \int_{t_0}^{t_1} v_g(t)dt = \int_{x_0}^{x_1} dx = l \tag{4.2}$$

where l is the length of the discharge region, as defined in Figure 3.6; $v_g(t)$ is the time-dependent gas flow velocity; x_0 is the position at which the gas enters the discharge; x_1 is the point at which the gas exits the discharge; t_0 is the time at which the gas enters the discharge; and t_1 is the time at which the gas exits the discharge. The velocity of the gas is a function of the time-dependent pressure based on the ideal gas law and mass conservation. Starting with the ideal gas law:

$$P = \frac{N}{V} k_B T_g \tag{4.3}$$

where P is pressure, N is the number density, V is the volume, k_B is the Boltzmann constant, and T_g is the gas temperature. Mass conservation law dictates:

$$\rho_1 v_1 = \rho_0 v_0 \tag{4.4}$$

where ρ is the density of the gas. Assuming that pressure is constant along the axis of the flow, manipulation of these two equations shows the time-dependent gas velocity:

$$v(t) = v_0 \frac{T_g(t)}{T_0} \tag{4.5}$$

From Section 2.5, Equation 2.18, the time-dependent temperature is modeled as:

$$T_g(t_r^{'}) = \frac{T_0 \gamma\ e^{\gamma\ t_r^{'}}}{\left(\beta + T_0 \alpha\ e^{\gamma\ t_r^{'}}\right)} \tag{4.6}$$

So,

$$\int_0^{t_r} v(t_r')\,dt_r' = \int_0^{t_r} v_0 \frac{\gamma\, e^{\gamma t_r'}}{\left(\beta + T_0\alpha\, e^{\gamma t_r'}\right)}\, dt_r' = l \tag{4.7}$$

Solving Equation 4.7 for t_r yields:

$$t_r = \frac{1}{\gamma}\ln\left(\beta - \left(T_0\alpha + \beta\right)\, \mathrm{e}^{\alpha\, l/v}\right) \tag{4.8}$$

Note that the solution for the time-dependent temperature, Equation 4.6, is in terms of t_r'.

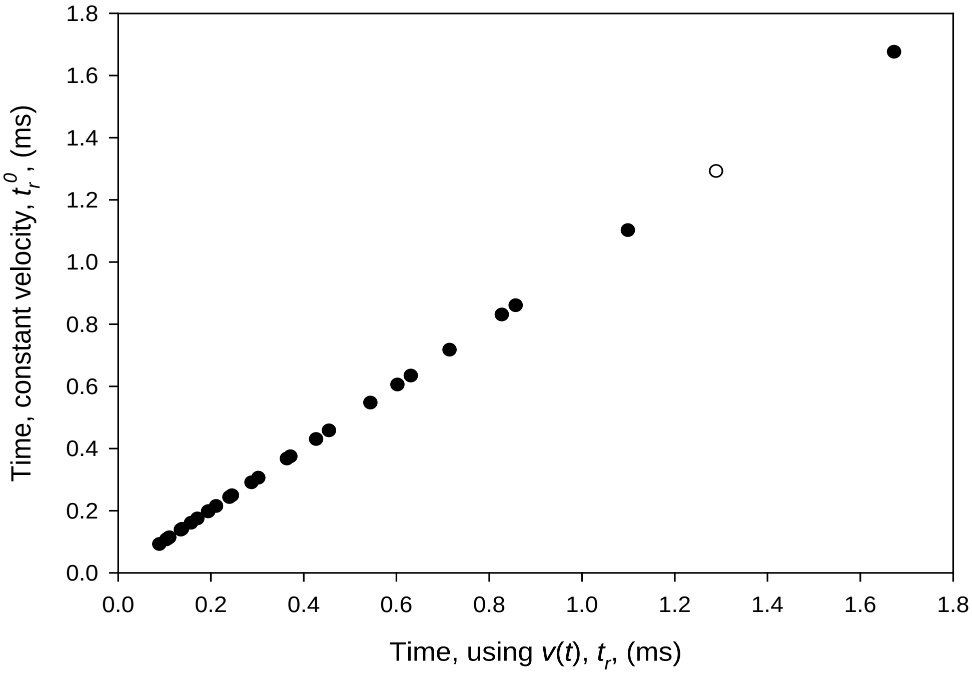

Figure 4.7 Comparison of residence time, defined by Equation 4.1, assuming a constant velocity throughout the discharge region, as opposed to using the time-varying velocity, at P = P_0.

Therefore, pressure normalization is built into the solution of t_r. t_r is the amount of time the gas resides within the discharge region, taking into consideration the time variation of the velocity within the discharge. The effect of time varying temperature on the overall residence time will be explored in the following discussion.

4.3.1 Time Varying Velocity

The velocity of the gas flow changes as the temperature of the gas changes. This change in velocity will affect the amount of time the gas resides within the discharge region. However, gas temperature reaches a steady-state value almost immediately within the discharge region, as shown in Figure 4.5. Because T_g comes to steady-state so quickly, the only period in which the time varying velocity calculation differs from the constant temperature calculation is in the first few milliseconds of the discharge. Therefore, the effect of including the time varying velocity is expected to be small. In Figure 4.7, the residence time is reported using constant and time varying velocities. The linear relationship between these two values shows that the residence time of the gas is virtually unaffected by the velocity change within the gas.

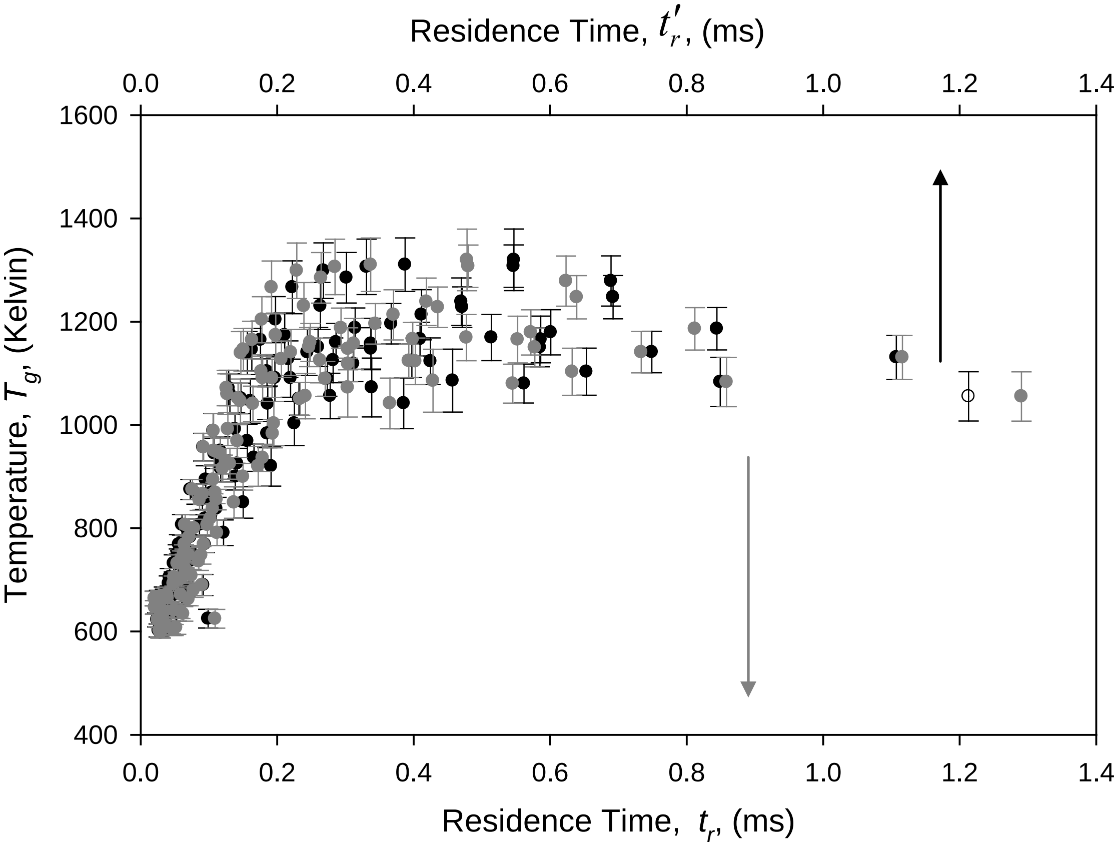

Figure 4.8 Two plots showing the difference in the temperature versus time plot made by including a time-dependent velocity. ● plot using t_r' and ● plot using t_r.

Figure 4.8 shows the gas temperature as a function of both forms of the residence time, t_r and t_r'. As expected, the figure shows very little difference between the two plots. This is because the temperature varying velocity does not have a significant effect upon the residence time of the gas. Even though a change in velocity has a negligible effect on the residence time of the gas, the large temperature change as the gas enters the discharge requires that the gas temperature be well defined.

4.4 Power Loading in Gas Flow

When analyzing plasmas sustained in flowing gases, the temperature of the gas plays an important role. The temperature of the gas changes many important parameters: the kinetic rates, the gas flow velocity, and the number density of the emitters in the gas flow. The intensity of the emissions from the $O_2(a)$ state, I_a, is dependent on the concentration of the excited state $[O_2(a)]$ and, therefore, dependent on T_g, as governed by the ideal gas law. Also, the velocity of the gas flow determines the period of time in which the gas resides within the discharge region, affecting the energy deposited into the gas. The energy deposited into the gas plays a large role in determining the EEDF, which drives reaction rates of all reactions involving electrons. So, an in-depth understanding of the gas temperature in the flow is essential to interpretation of the system kinetics.

As discussed in Section 2.7, the functional form of the time-dependent gas temperature, $T_g(t)$, may be used to determine the value of the heat transfer coefficient of oxygen, h_T, and the fraction of energy coupled into gas heating, f, of the system. Fitting this functional form to the measured temperature data yields values of:

$$\begin{aligned} &T_0 T_{ss} = 6.4\times10^5\ K^2 \\ &\alpha \mathrm{T}_{\mathrm{ss}} = 3900\ s \\ &\left(T_{ss} - T_0\right) = 640\ K \end{aligned} \tag{4.9}$$

for the parameters in Equation 2.24. This system of equations can be solved giving values of:

$$\begin{aligned} &T_0 = 542 \pm 18\ K \\ &\mathrm{T}_{\mathrm{ss}} = 1182 \pm 10\ K \\ &\alpha = 3.3 \pm 0.3\ s \end{aligned} \tag{4.10}$$

for the fit parameters. These results are then used to calculate values for h_T and *f,* as follows. Using Equation 2.14:

$$\rho V C_p \frac{dT_g}{dt} = fP_{in} - Sh_T(T_g - T_0) \tag{4.11}$$

α may be written as:

$$\alpha = \frac{Sh_T}{\rho V C_P} \tag{4.12}$$

The values for this calculation are:

$$C_p = 1{,}005 \text{ J kg}^{-1} \text{ K}^{-1},\ V = 1\ \pi\ r^2 = 2.36 \times 10^{-6}, \tag{4.13}$$

where l = 0.03 m, r = 0. 5 cm.

The density of oxygen is:

$$\rho = (1.41\text{x } 10^3)\ (7.5/760)\ (300/1200) \text{ kg m}^{-3} \tag{4.14}$$

at 7.5 Torr and 1,200 K. The fraction of the energy coupled into the overall gas heating is found from the determination of the value for β*,* where:

$$\beta = \frac{fP_{in}}{\rho V C_P} \tag{4.15}$$

The value of β is determined from the values of T_{ss}, T_0, and α by the relationship:

$$T_{ss} = \frac{T_0\alpha + \beta}{\alpha} \tag{4.16}$$

The power coupled into the gas, P_{in}, is 85 W, and, from Kays and Crawford,[40] k_T = 0.0717 (W m^{-1} K^{-1}). The theoretical model is fit to the measured temperature data, and the following values for h_T and *f* are extracted:

$$
\begin{aligned}
h_T &= 29 \pm 7 \quad (\mathrm{W} \cdot \mathrm{m}^{-2} \cdot \mathrm{K}^{-1}) \\
f &= 17 \pm 2\%
\end{aligned}
\tag{4.17}
$$

From the extracted value of h_T, the Nusselt number, N_u, may be calculated:

$$
Nu = \frac{h_T D}{k_T} = 4.08 \pm 1.05 \tag{4.18}
$$

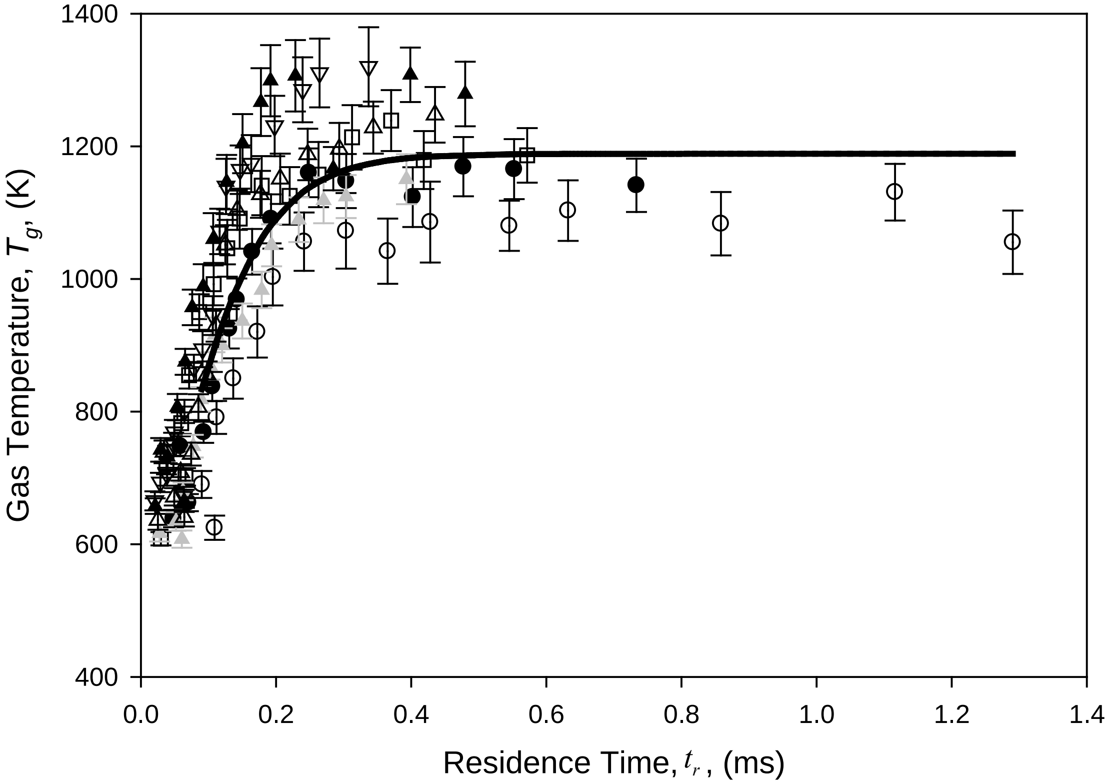

Figure 4.9 Temperature as a function of time in the discharge is governed by power balance of heat coupled into the discharge and heat lost to the wall. Only a fraction of the power is coupled to heat ○ 2 Torr, ● 3 Torr, □ 4 Torr, ▲ 5.2 Torr, △ 6.4 Torr, ▲ 7.5 Torr, ▽ 8.6 Torr, — Theoretical fit.

The expected N_u is 4.364 for cylindrical geometries.[40] This value is well within the error of the determined value. The steady state temperature , $T_{ss} = 1182 \pm 10$, is significantly lower than anticipated if heat transfer to the wall or flow of excited species out of the discharge is not considered. The fit result $f = 0.17 \pm 0.02$ implies most of the discharge power does not raise the gas temperature. The analysis presented in Appendix B indicates that significant power is transferred to the reactor walls via atomic oxygen reactions. The reactor wall requires active cooling with compressed air to prevent glass softening. Indeed, thermal control and surface reactions appear important in most EOIL demonstrations.

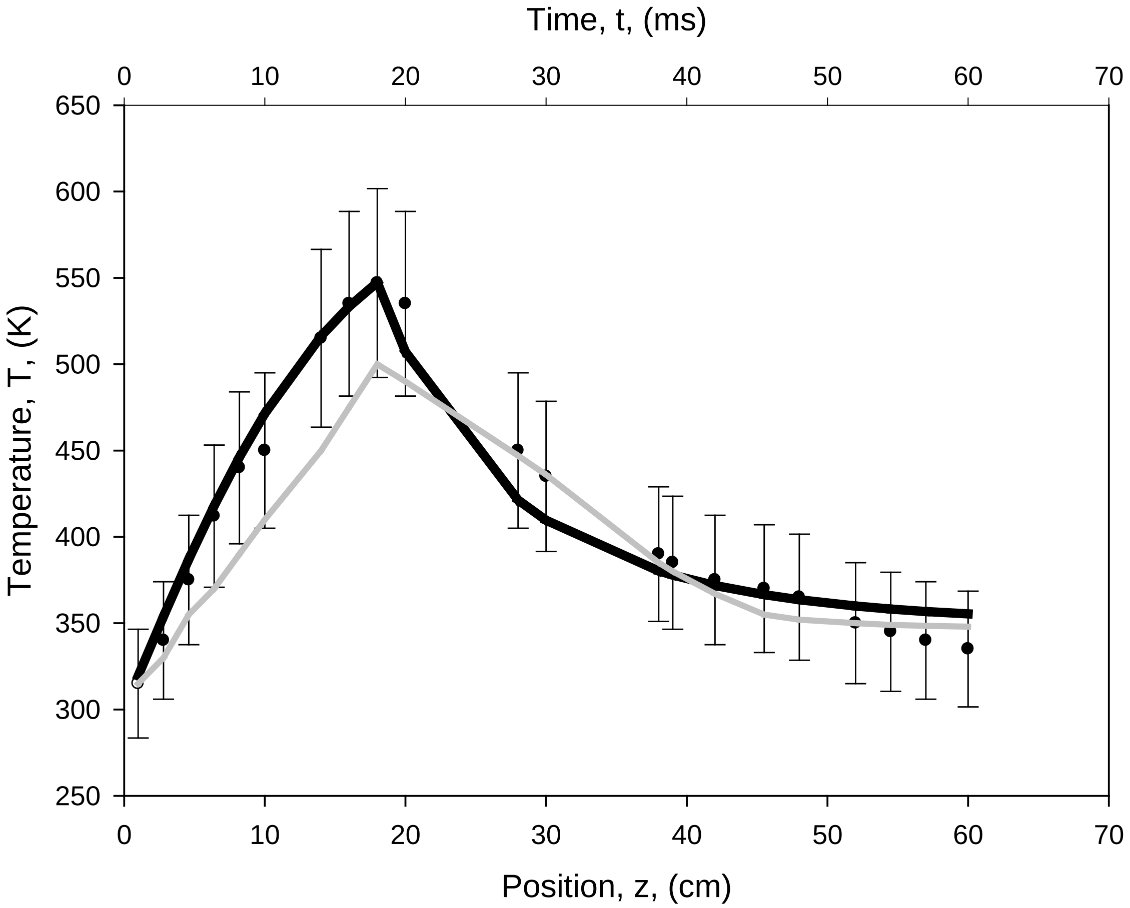

Figure 4.10 ● Measured[7], ▬ Stafford[7], ▬ *Nu* = 4.22 and f = 17%, using equation 2.18 to describe the heat transfer and setting the input power outside of the discharge to zero, the theoretical result is compared to the measured results of Carroll and simulated results of Kushner.

Using the functional form of gas temperature determined in Equation 2.18, values for h_T and f may be extracted from the results reported by Stafford and Kushner.[7] The measured data in Figure 4.10 are the results of an experiment performed by Carroll et al. at UIUC and reported by Stafford and Kushner.[7] The flow tube has a 4.83 cm ID with 265 W of coupled power, via an RF field, into a flow of pure O_2 at 5 mmol/s and the pressure being held at 2 Torr.

The fit of Equation 2.18 to the measurements reported by Stafford is shown in Figure 4.10. From position z = 0 to 20 cm, the gas is within the discharge region; at 20 cm, the discharge power into the system is set to zero, representing the end of the discharge region. The differential equation that describes the decay of temperature without an energy source is a simplification of Equation 2.14:

$$\rho V C_p \frac{dT_g}{dt_r} = -S h_T (T_g - T_0) \tag{4.19}$$

The solution to this differential equation is:

$$T_g(t_r) = T_0 \left(1 + e^{-\frac{h_T S}{C_p \rho V} t_r} \right) \tag{4.20}$$

Therefore, outside of the discharge, the temperature decays exponentially, which is clearly the case in Figure 4.10.

Using a least-squares fitting method inside the discharge region, the values of h_T and f for the UIUC results are fit to data from 0 to 20 cm, resulting in a N_u value of 4.22, which is again very similar to the theoretically expected values of 4.364. It is predicted that only 17% of the power coupled into the gas results in heating. The fraction of power coupled into gas heating in μ-wave discharges and RF discharges is approximately the same for these studies. This is an unexpected observation, because the E-fields are different, and the geometry of the two experiments is different. The fraction of the energy coupled into the gas flow will be discussed later in this work.

4.5 $O_2(a)$Yield

In the COIL, population inversion of the iodine atoms is achieved using the $O_2(a)$ state as an energy reservoir. The quantity of extractable power is determined by the ratio of $[O_2(a)]$ and $\left[O_2(X)\right]$ in the system. Optical monitoring of the emissions from the excited states provides a convenient way to determine number density and not perturb the performance of the SOG. The relationship between number density of the emitting species and the emission intensity is:

$$I_a = C_r A_{ij} N_i \tag{4.21}$$

where I_a is the emission intensity; A_{ij} is the Einstein A coefficient for the transition; N_i is the number density of emitting species in the discharge; and C_r is a factor, including the radiometry of the detection system.

4.5.1 $O_2(a)$ Spectrum and Modeling

The $O_2(a^1\Delta_g \rightarrow X^3\Sigma_g^-)$ spectrum centered near $\lambda = 1.268$ μm has nine rotational branches ($^{\Delta K}\Delta J = {}^{O}P, {}^{P}P, {}^{P}Q, {}^{Q}P, {}^{Q}Q, {}^{Q}R, {}^{R}R, {}^{R}Q, {}^{S}R$), as discussed in Section 2.4.1.[37] The lifetime of the $O_2(a)$ state is 64 minutes, making emission strengths weak.[20] Thus, a spectrometer with lesser spectral resolution than that used for the measurement of $O_2(b)$

is used to increase the throughput and signal to noise ratio. The rotational features are not resolved as they were for the $O_2(b)$ emissions. A typical $O_2(a)$ spectrum measured 5 cm downstream of the discharge is shown in Figure 4.11.

The simulation of the $O_2(a)$ emissions, also shown in Figure 4.11, is a sum of Lorentzian peaks, all with the same width of 0.15 nm and relative intensities governed by a Boltzmann temperature distribution at 600 K.

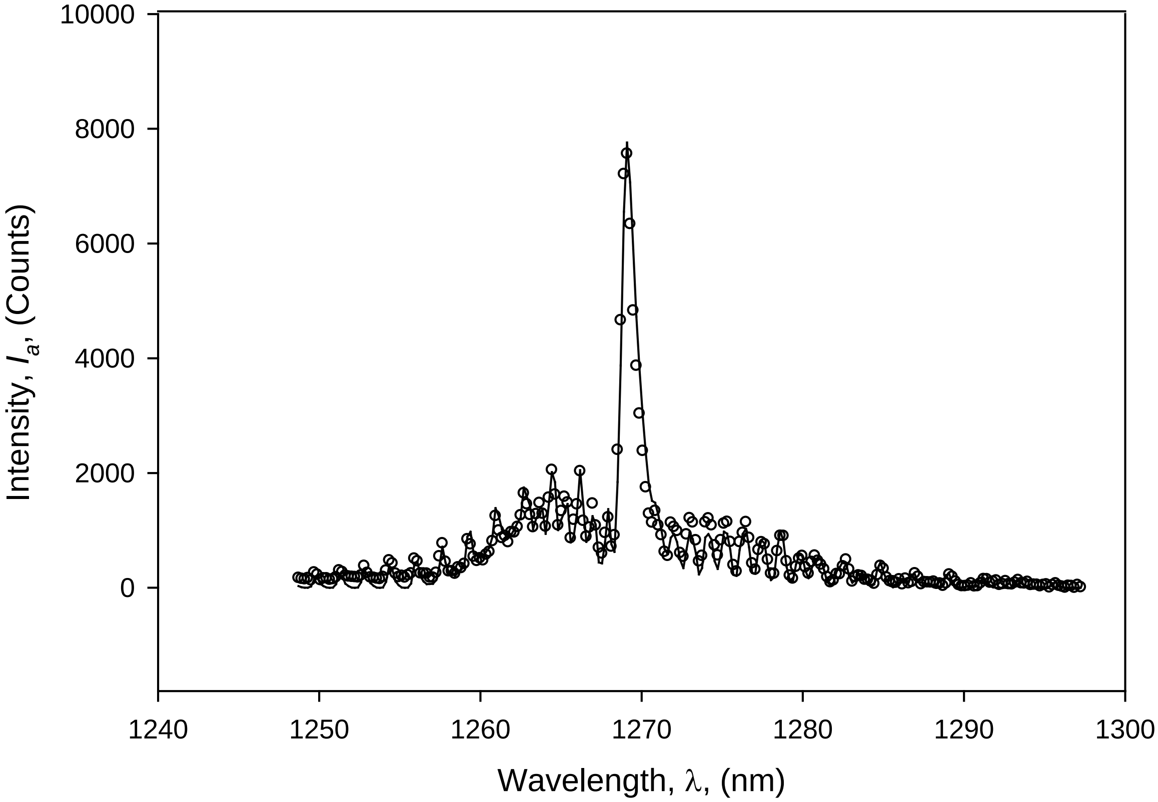

Figure 4.11 Typical *$O_2(a)$* spectra resulting from the discharge and a simulation of the spectra, at 4 Torr, 600 K, and 500 SCCM, 5 cm downstream of the discharge. ○ measured emissions, ▬ simulated emissions.

The temperature is a fit parameter of the model and yields values very similar to the results determined using the $O_2(b)$ emissions in the same position along the flow tube. Peak locations and Einstein A coefficients are extracted from the HITRAN database for the $^{16}O_2$ ($a^1\Delta$-$X^3\Sigma$) (0-0) and ^{16}O-^{18}O ($a^1\Delta$-$X^3\Sigma$) (0-0) transitions. The 1-1 transition is centered on 1,280 nm; therefore, the contribution from this emitting state is included in the simulation. The Einstein A coefficient of the 1-1 transition is assumed to be the same value as the 0-0 transition with the 0-0 line positions scaled by the appropriate energy difference.[37]

Outside of the discharge region, the $O_2(a \rightarrow X)$ spectrum is well isolated from contaminating emissions. A number of excited O-atom states are populated within the discharge, resulting in several atomic oxygen emission lines dominating the spectrum, as shown in Figures 4.12 and 4.13. In Figure 4.12, the strong ^3F – ^3D (1,257 nm) and 1,299 nm lines bracket the $O_2(a \rightarrow X)$ emission. In Figure 4.13, the emissions in the spectral range of 1,266.8 to 1,277 nm are shown to be largely isolated from atomic emissions. The Q-branch structure is still clearly evident. The $\lambda = 1,266.8$ to 1,277 nm region is integrated to provide a relative measure of $O_2(a)$ concentration. The weaker ^3D-^3P and ^3S-^3P lines at 1,265 and 1,278 nm are outside of this integration band. Spectral simulations of the $O_2(a \rightarrow X)$ emission have been developed to assess the dependence of the band shape on rotational temperature.

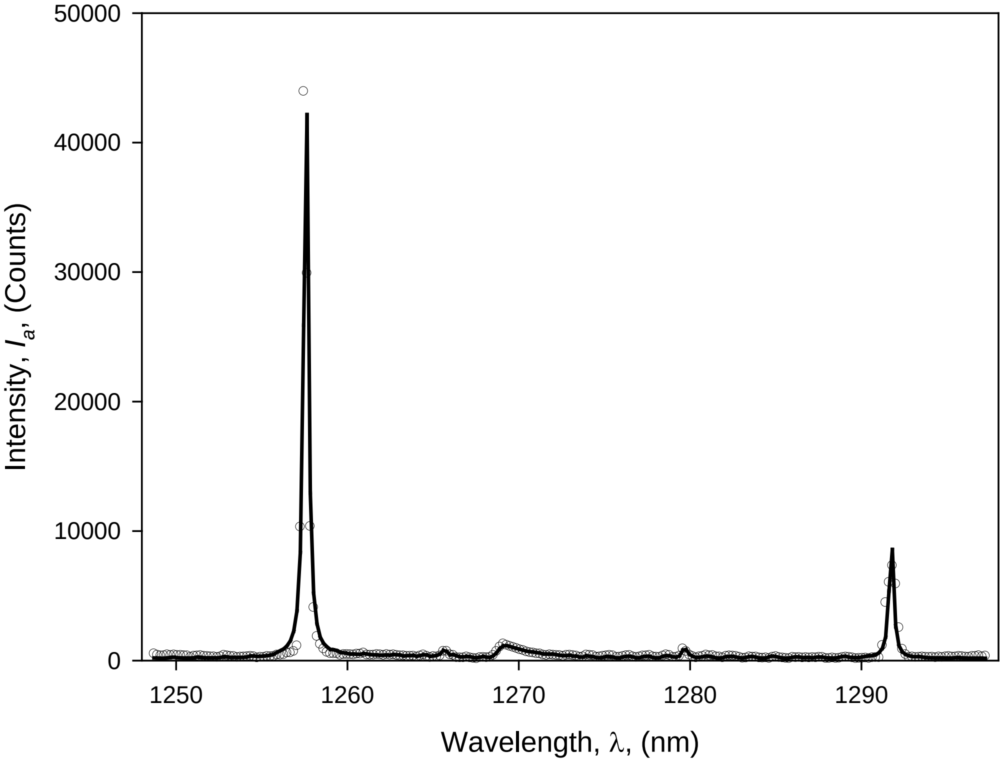

Figure 4.12 Emissions from inside the discharge in the wavelength region of $O_2(a)$, at 4 Torr, and 500 SCCM. ○ measured data, ▬ simulated spectrum.

The gas temperatures inside and downstream of the discharge are significantly different. From the $O_2(a)$ simulation in Figures 4.11 and 4.13, T_g is 600 K 5 cm downstream of the discharge and 1,100 K directly inside the discharge. The temperature determined inside the discharge is in excellent agreement with the 1,200 K determined from the $O_2(b)$ emissions. The possible sources of inaccurate determination of the I_a values extracted from the measured data are the wings of the O-atom emissions. Figure 4.14 will take a closer look at these contributions.

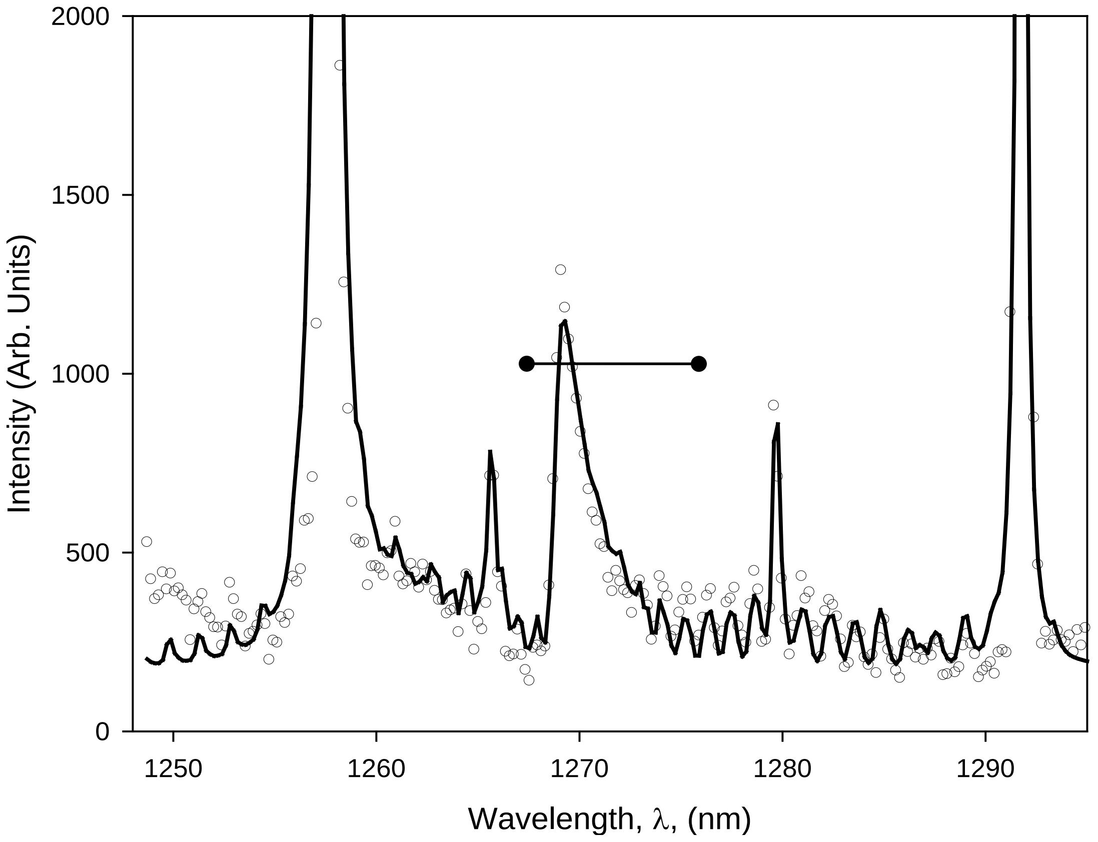

Figure 4.13 Rescaled view of emissions from inside the discharge in the wavelength region of *$O_2(a)$*, at 4 Torr, and 500 SCCM. ○measured data, ▬ simulated spectrum.

Figure 4.14 shows the simulated spectrum with the contribution from the $O_2(a)$ (0-0) transition subtracted from the total spectrum. The remaining signal is made up of the $O_2(a)$ (1-1) transition, as well as the contribution from the O-atom emissions. Summing the remaining signal in the wavelength range of 1,266.8 to 1,277 nm and dividing by the sum of the $O_2(a)$ emissions, it is determined that less than 9% of the signal is made up of emissions not directly linked to the $O_2(a)$ emissions.

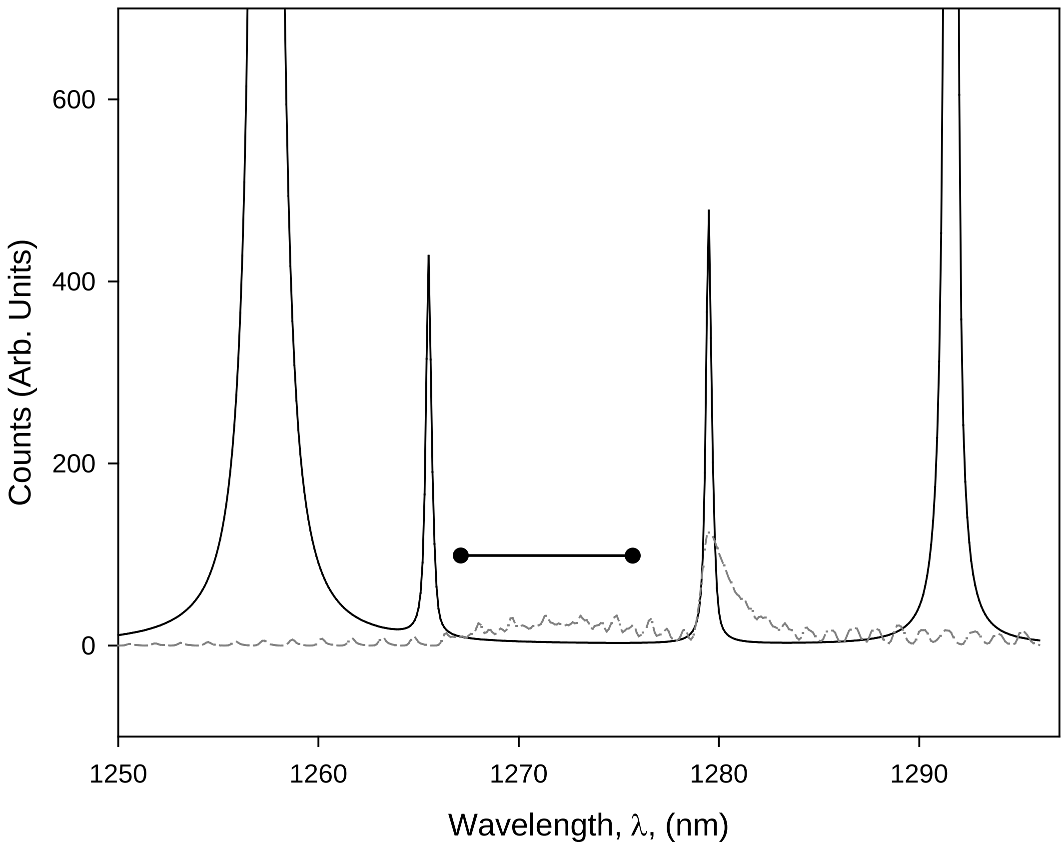

Figure 4.14 Simulation of *$O_2(a)$* with contribution from the (0-0) transition removed. ● simulated spectrum with *$O_2(a)$* (0-0) contribution removed, - - *$O_2(a$*, 1-1), ▬ O-atoms.

Many research groups use $O_2(a)$ detection techniques, which simply include a detector and a band pass filter or very low resolution spectrum analyzers with a bandwidth of 100 nm.[2, 11, 12] These techniques, while sufficient if the detector is an appropriate distance downstream of the discharge, will give erroneous results if the atomic emissions are not included in one's analysis.

4.5.2 $O_2(a)$ Yield Calculation

The intensity of the emissions is dependent on the number of emitters present in the field of observation, as well as the Einstein A coefficient, A_{ij}, of the excited state. The gas is heated significantly within the discharge, and the number density is changed accordingly. Therefore, the change of the emission intensity as a function of temperature must be accounted for if the kinetics are to be extracted from the measurements. Also, collision frequencies are influenced by particle densities.

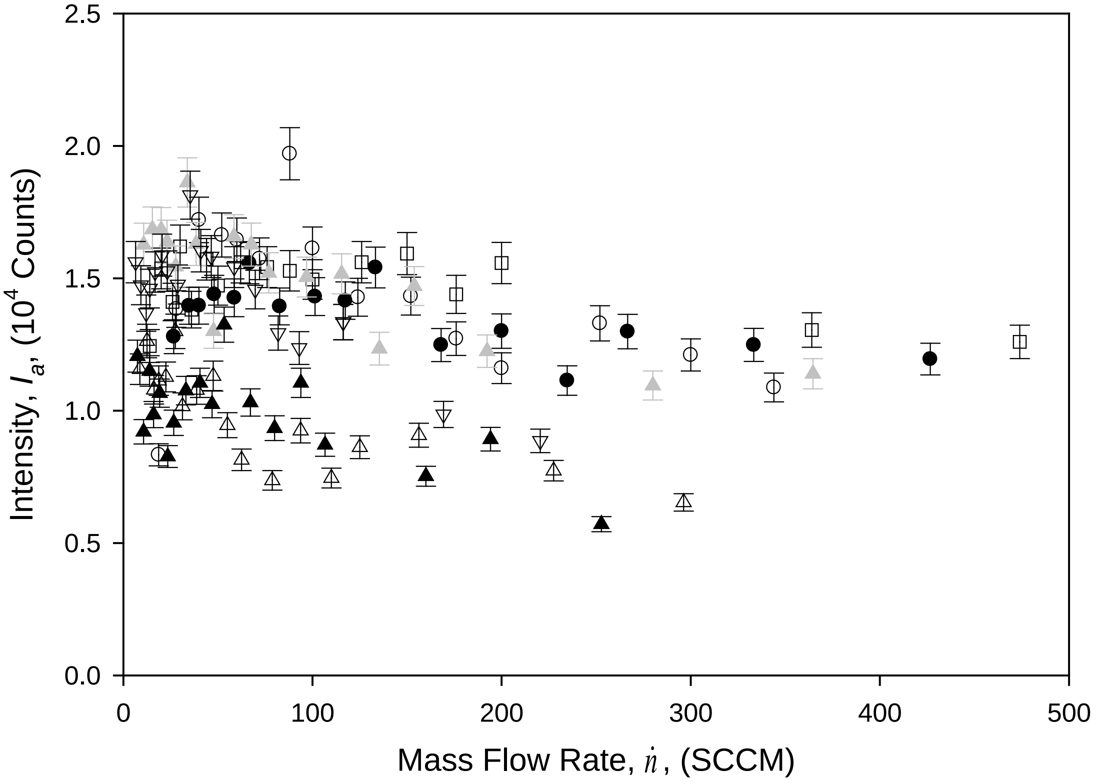

Figure 4.15 Intensity measurement of the $O_2(a)$ emissions versus the mass flow rate: ○ 2 Torr, ● 3 Torr, □ 4 Torr, ▲ 5.2 Torr, △ 6.4 Torr, ▲ 7.5 Torr, ▽ 8.6 Torr.

In order to determine the change in the yield of $O_2(a)$, Y_a, as a function of pressure and residence time, the measured quantities are the intensity of the $O_2(a)$

emissions, I_a, and mass flow rate, $\dot{n}$. The dependence of I_a on the gas temperature, T_g, has been explained, and the effects have been removed from the measured data in order to study the chemical kinetics of the system.

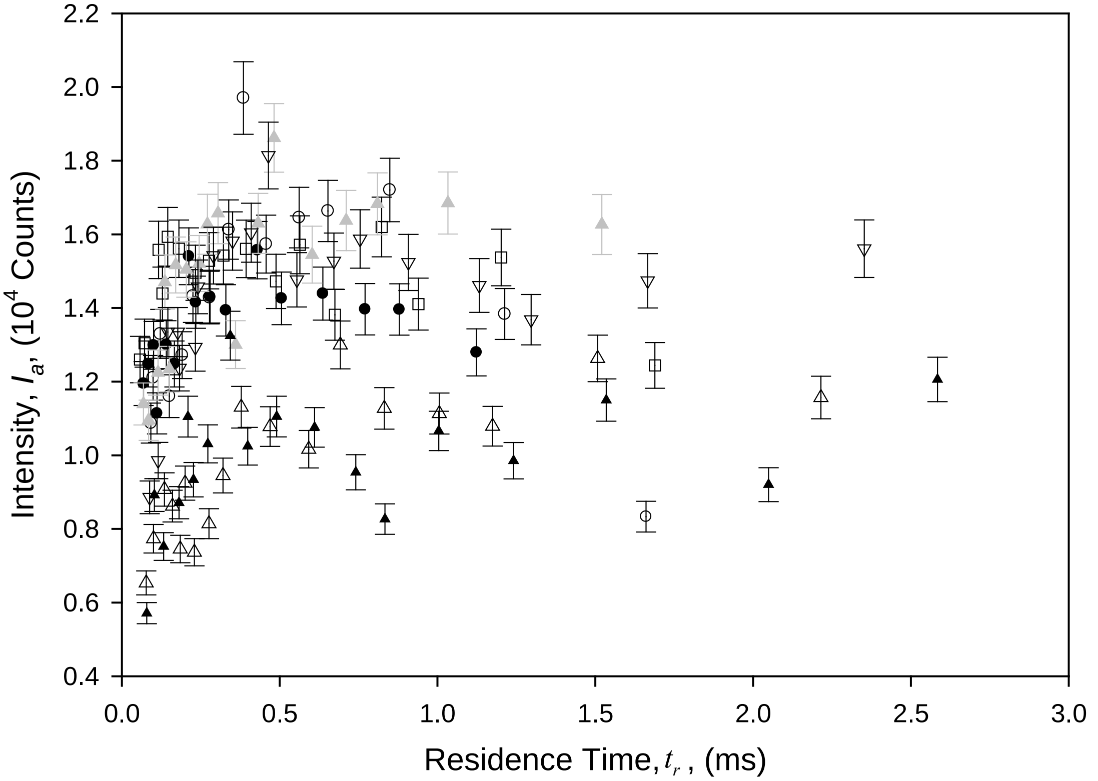

Figure 4.16 Intensity measurement of the $O_2(a)$ emissions versus residence time: ○ 2 Torr, ● 3 Torr, □ 4 Torr, ▲ 5.2 Torr, △ 6.4 Torr, ▲ 7.5 Torr, ▽ 8.6 Torr.

The data, I_a versus the mass flow rate, $\dot{n}$, is shown in Figure 4.15. The intensity of the $O_2(a)$ emissions, I_a, has about a 10% error bound with a decreasing trend as a function of the gas pressure and a slight decrease at higher mass flow rates. The previous analysis of gas temperature is used to map from the mass flow rate, $\dot{n}$, to the residence time, t_r, resulting in Figure 4.16. In Figure 4.16, the high mass flow rates correspond to the largest velocities, which, in turn, become the shortest residence times. The slight change in intensity at the high mass flow rates is more apparent, showing that, before the intensities come to a constant value within the first millisecond of entering the discharge region, the concentration of $O_2(a)$ increases. The reason for measuring the $O_2(a)$ emissions is to study the changes in yield as a function of pressure and velocity, so yield can now be calculated.

4.5.3 Scaling Emission Intensity of $O_2(a)$ to Yield

The intent of this study is to explore the mechanism responsible for limiting the yield of $O_2(a)$ achievable within electric discharges in oxygen gas flows as oxygen partial pressure increases. A mapping of measured $O_2(a)$ emission intensity, I_a, to the absolute concentration of $O_2(a)$, $[O_2(a)]$, is not necessary to determine plasma conditions that maximize $O_2(a)$ production. However, the majority of literature that discusses EOIL systems reports results in terms of the yield of $O_2(a)$.[3, 8, 13, 17] In order to compare the current results to those published in the literature, a scaling term, k_r, will be determined that will enable the comparison of the intensity measurements to the yields reported in the literature.

The parameter energy per particle, ξ_{part}, of the system is commonly used in literature.[7, 16] ξ_{part} is the energy coupled into the gas divided by the number of particles that flow through the plasma volume. Note that the number of particles flowing through the discharge volume is time-dependent.

The coupled power, length of the discharge, radius of the flow tube, flow velocity of the gas, gas stoichiometry, and gas pressure all vary between experiments. By using the parameter, energy per particle, results from a variety of different discharge conditions may be compared. The ξ_{part} for the measurements made in this study may be written as the coupled power times the residence time of the gas divided by the number density of the gas:

$$\xi_{part} = \frac{P_{in} \times t_r}{[O_2(X)]} \tag{4.22}$$

Figure 4.17 shows the $O_2(a)$ emissions, measured in this work, for a plasma, sustained by an electric field oscillating at the same frequency, with the same geometry, and the same flow conditions, as reported by Rakimova.[17] The scaling term, k_r, is determined by comparing the RF results to those by Rakihmova and assuming that concentrations of singlet oxygen will be the same under the same discharge conditions. Note that the inner diameter of the flow tube used in this study is 1 cm, which is 0.05 cm smaller than the flow tube used in Rakimova's work. This discrepancy is because the wall thickness of the flow tubes in the two studies differs.

The $O_2(a)$ emissions were collected for three pressures, 2, 4, and 7 Torr. When measuring the 2 Torr case, the flow tube overheated when the gas flow within the discharge was insufficient to cool the tube. As a result, analyzing the 2 Torr case is difficult, because the gas does not reside in the discharge region for a time long enough to determine a steady-state population for this pressure. However, a scaling term may be determined when using the 4 and 7 Torr measurements.

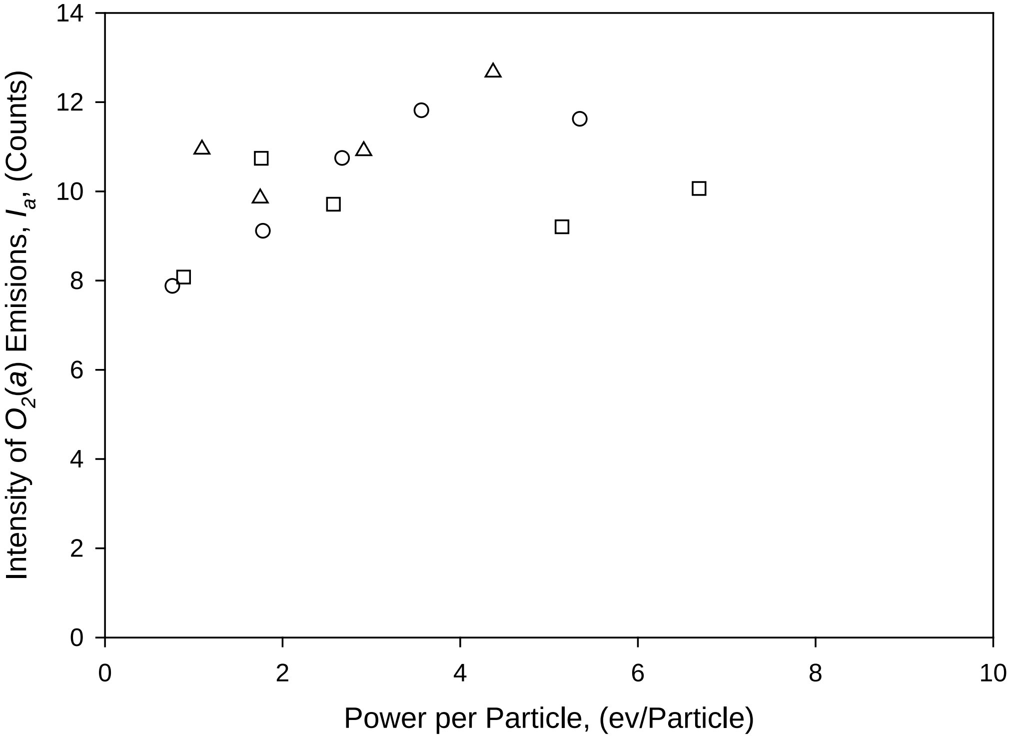

Figure 4.17 Emission intensity of $O_2(a)$ as a function of energy per particle in the current RF discharge. △ 2 Torr, ○ 4 Torr, □ 7 Torr.

The scaling term, k_r, was calculated for the 4 Torr case and was found to be accurate for the 7 Torr results as well, showing that the relationship between I_a and $[O_2(a)]$ is linear over the pressure range 4 – 7 Torr. Discussing these results in terms of yield requires a calibration of the detection system, which results in reporting concentrations with an error greater than 20%. The majority of the arguments included in this work will depend only on the relative changes in concentration.

The yield of $O_2(a)$ in the system is calculated from the intensity of the emissions, the gas temperature, and scaling to results reported by Rakimova[17]:

$$Yield,\ Y_a = \frac{I_a}{[O_2(X)]} \times k_Y \tag{4.23}$$

k_r = Scaling to Rakimova

where I_a is the measured intensity of the emissions; $[O_2(X)]$ is the number density of the ground state oxygen within the flow tube, including the affect of gas temperature. Note that the temperature dependence of the emitter is already built into the yield calculation via the temperature-dependent ground state population results.

The scaling term is determined by comparing the RF results to those by Rakihmova. Both measurements are made using RF discharges, the same deposited energies ranging from 0.5 to 7.5 electron volts per particle. The error bars are representative of the error associated with calibrated optical HPGe detectors used in the literature. There is the possibility of an error being introduced to the results by using this scaling system. However, discussions in chapter 5 are based on the relative change of yield and not the absolute yield. In the discussion of quenching mechanism, the absolute yields will play a significant role only if they are orders of magnitude different from calculated results. It is unlikely that the system is giving results below 5% yields or greater than 15% yields.

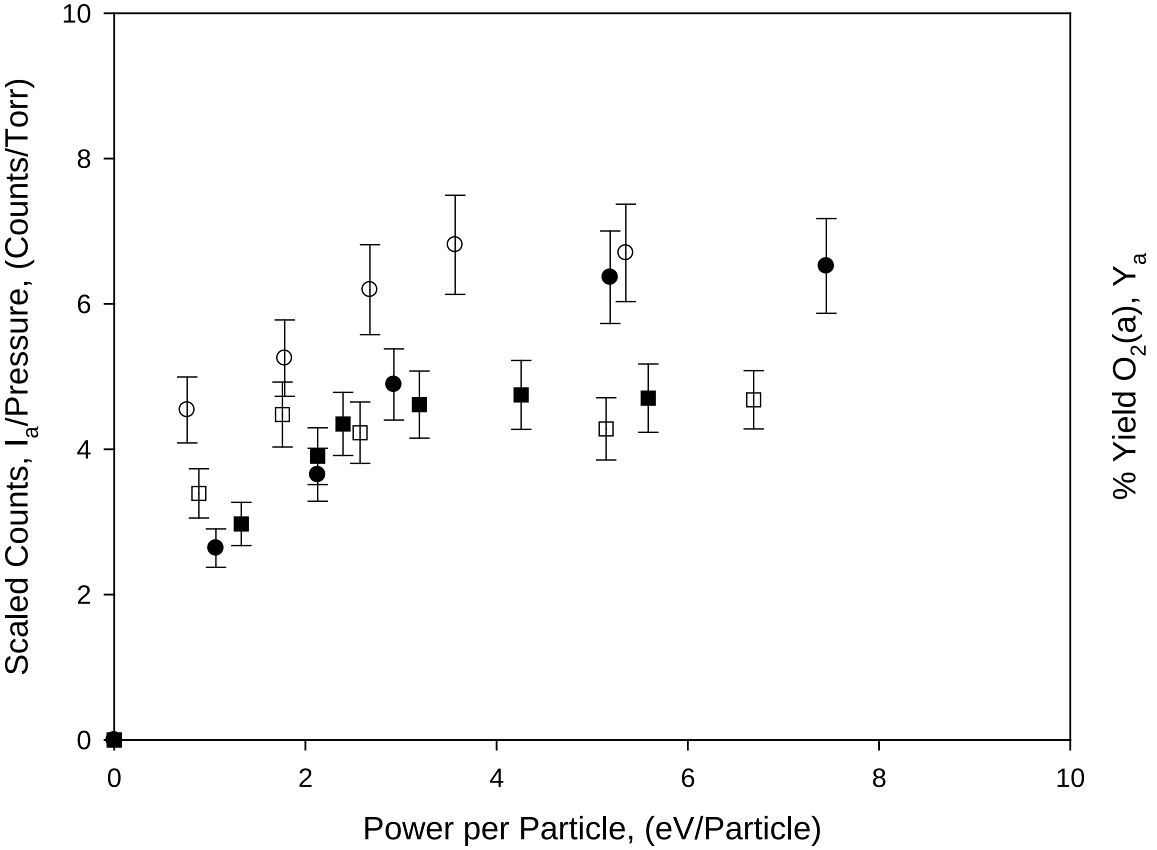

Figure 4.18 Yield as a function of energy per particle in an RF discharge, as reported by Rakimova (solid points) and this work (hollow points). ○ 4 Torr, ● 4 Torr Rakimova, □ 7 Torr, and ■ 7 Torr Rakimova.[17]

Mapping the I_a measurements to yields allows comparing these results to other published works, as well as comparing them to computer-simulated concentrations. Besides $O_2(a)$, electrons and atomic oxygen are expected to have significant concentrations within the glow discharge. The atomic oxygen density is determined using the actinometry technique, which is discussed in Section 4.7. The electron density of the glow discharge is determined by a computer model. The specifics of the computer model used to simulate the oxygen discharges in this study are discussed in Section 4.6.

4.6 Results of Simulations

Current systems that model electric discharges in oxygen include a large number of pathways for creating and destroying species within the discharge. These numerical models yield results which fail to reproduce pressure trends in $O_2(a)$ concentrations. Determining means to correct models is complicated by the extensive kinetic packages implemented in these models. In this study, we seek to understand why the $O_2(a)$ yield decreases as a function of the oxygen pressure within the gas flow. The roles of electrons and atomic oxygen in the destruction of $O_2(a)$ are of particular interest to the EOIL community. In order to understand the chemical kinetics, a simulation involving only the essential chemical kinetics is developed. In this section, the streamlined simulation used in this study is described.

4.6.1 Simplified Analytic Expression of Kinetics

The reactions included in the analytic representation of the system are shown in Table 2.1. The electron density in the system, at steady-state, is determined primarily by direct ionization of ground state molecular oxygen (reaction 3) and recombination of electrons with positive molecular ions (reaction 5):

$$\begin{aligned}
&e^- + O_2(X) \xrightarrow{k_{ion}} O_2^+ + e^- + e^- \\
&e^- + O_2^+ \xrightarrow{k_{rec}} O_2(X) \\
&e^- + O_2(X) \xrightarrow{k_{attach}} O^- + O \\
&e^- \xrightarrow{k_{diff}} \text{Diffusion from Discharge}
\end{aligned} \tag{4.24}$$

Electron loss is dominated by attachment thereby eliminating any change in the electron density due to collisions at the wall. The relative rates will be calculated later.

O-atoms are generated by the electron impact of ground state oxygen (reactions 13-15) and destroyed by recombination at the walls (reaction 19):

$$\begin{aligned}
&e^- + O_2(X) \xrightarrow{k_O} O(^3P) + O(^3P) + e^- \\
&e^- + O_2(X) \xrightarrow{k_O} O(^3P) + O(^1D) + e^- \\
&O(^3P) + O(^3P) \xrightarrow{k_{Wall}} O_2(X)
\end{aligned} \tag{4.25}$$

The concentration of $O_2(a)$ is determined by direct electron impact with ground state molecular oxygen (reaction 10) and the inverse reaction, as determined by using detailed balance (reaction 17):

$$\begin{aligned}
&e^- + O_2(X) \xrightarrow{k_{a+}} O_2(a) + e^- \\
&e^- + O_2(a) \xrightarrow{k_{a-}} O_2(X) + e^-
\end{aligned} \tag{4.26}$$

The principal species involved in a glow discharge are ground state oxygen, the $O_2(a)$ singlet delta molecular oxygen state, the $O(^3P)$ atomic state, and electrons. The kinetic energy of the electrons is determined by the reduced effective electric field. The negative ions are destroyed primarily by ionic recombination (reaction 21):

$$O^- + O_2^+ \xrightarrow{k_{Orec}} O_2(X) \tag{4.27}$$

This streamlined set of rates is used in conjunction with the power balance equation (Equation 4.33) to describe the system, assuming that steady-state has been reached:

$$\left[O_2(a)\right]_{ss} = \frac{k_{a+}\left[e^-\right]_{ss}\left[O_2(X)\right]_{ss}}{k_{a-}\left[e^-\right]_{ss} + \Gamma_a} \tag{4.28}$$

$$\left[e^-\right]_{ss} = \frac{k_{ion}\left[O_2(X)\right]_{ss} - k_{att}\left[O_2(X)\right]_{ss} - k_{diff}}{k_{rec}} \tag{4.29}$$

$$\left[O^{-}\right]_{ss} = \frac{k_{attach}\left[O_2(X)\right]_{ss}\left[e^{-}\right]_{ss}}{k_{Orec}\left[O^{-}\right]_{ss}} \tag{4.30}$$

$$\left[O(^3P)\right]_{ss} = \frac{k_{O+}\left[e^{-}\right]_{ss}\left[O_2(X)\right]_{ss}}{k_{Wall}} \tag{4.31}$$

$$\left[O_2(X)\right]_{ss} = \left[O_2(X)\right]_{ss} - \left[O_2(a)\right]_{ss} - \frac{\left[O(^3P)\right]_{ss}}{2} \tag{4.32}$$

$$k_L(\mathrm{E_{eff}/N})\left[e^{-}\right]_{ss}\left[\mathrm{O_2(X)}\right]_{ss} = \frac{P_{in}}{V} - \frac{A\,v}{V}\left(\Delta\varepsilon_o \frac{\left[\mathrm{O}\left(^3\mathrm{P}\right)\right]_{ss}}{2} + \Delta\varepsilon_a\left[\mathrm{O_2(a)}\right]_{ss}\right) \tag{4.33}$$

where $k_L(E_{eff}/N)$ is the inelastic reaction rate coefficient and is equal to $\sum_i \Delta\varepsilon_i k_i$ given in units of (eV m^3 s^{-1}) where *i* ranges over the reactions 1-16 and $\Delta\varepsilon_i$ is the amount of energy required to excite the i^{th} excited state. Also, $\Delta\varepsilon_o$ and $\Delta\varepsilon_a$ are the energy required to dissociate $O_2(X)$ into two ground state O-atoms and the excitation of $O_2(X)$ to the $O_2(a)$ state (6.0 eV and 0.98 eV, respectively). The steady-state concentrations of the species are $[O_2(a)]_{ss}$, $[O_2(X)]_{ss}$, $[O(^3P)]_{ss}$, $[O^{-}]_{ss}$, and $[e^{-}]_{ss}$. The Γ_a is the pseudo-first order decay rate used to compare the analytic expression of the $O_2(a)$ concentration to the measured intensities. Γ_a is used in Equation 4.28 instead of guessing at a possible dominant destruction method of the $O_2(a)$ state. By fitting the streamlined equation to the measured $O_2(a)$ data, as will be shown in section 4.8.1, the behavior of measured data will be used to discuss possible destruction methods. The rate coefficients, k_{a+} and k_{a-}, are production and destruction of the $O_2(a)$ state by electrons. These rate coefficients are a function of the electron temperature, T_e, as defined in Equation 2.8. T_e as a function of the reduced effective E-field is determined by solving the Boltzmann equation. In this work, BolSig+[27] is used to solve the Boltzmann equation, as discussed previously. All of the T_e dependent rate coefficients are determined using the BolSig+ package. Electrons are produced by ionization with a rate coefficient of k_{ion}. Loss mechanisms for the electron density are diffusion, with a rate coefficient of k_{diff}; attachment, with a rate coefficient of k_{att}, and electron recombination with a rate coefficient of k_{rec}. The plasma is assumed to be quasi-neutral, so the positive ion density must be equal to the sum of the negative ion density and electron density. O-atoms are produced by dissociative attachment (reaction 18) and directly by electron impact (reactions 14 and 15). The attachment and dissociation rate coefficients are summed and represented by k_{O+}. At steady-state the negative ions produced by dissociative attachment are considered a source of O-atoms. The destruction of negatively charged atomic oxygen is very fast, ~ 10^{-8} cm^{-3} s^{-1}, and results in negligibly small populations. This assertion will be discussed later in this section. The dominant loss mechanism for O-atoms is recombination at the walls of the flow tube, k_{wall}. From Gordiets et al., the radially averaged rates for wall loss can be expressed as[18]:

$$k_{Wall} = \left(\frac{\Lambda^2}{D} + \frac{2r}{v_{th}\gamma_O} \right)^{-1} s^{-1} \tag{4.34}$$

where Λ is the characteristic diffusion length; D denotes the diffusion coefficient; r is the radius of the cylindrical flow tube; v_{th} is the thermal velocity; and γ_O is the probability of reaction at the wall. For the pressure range studied, $\Lambda^2/D < 2r/v_{th}\gamma_O$. This assertion is based on the following approximated calculation:

First, from Perram et al.,[72, 73] $\Lambda = r/\sqrt{\phi}$, where $r = 0.005$ m, and ϕ is the unitless diffusion parameter for a cylinder = (2.4048).^{2} Therefore, $\Lambda = 2.079 \times 10^{-3}$ m. Also, D is a Fick diffusion coefficient, which, from Yolles et al.,[84] is equal to 2.7×10^{-5} (m^2 s^{-1}) for molecular oxygen and $O_2(b)$ at a pressure of 1 atm and 300 K. For this study the gas in the discharge region is at 1200 K and from Wilke and Lee[85] $D \;\alpha\; T_g^{3/2}$. Therefore at 4 Torr and 1,200 K, $D = (760/4)(1200/300)^{3/2}\,2.7 \times 10^{-5}$. Using these nominal values, the diffusion-limited portion of the wall rate is $\Lambda^2/D = 1.06 \times 10^{-4}$ s. So, for the wall reaction term, $2r/v_{th}\gamma_O$, the velocity of the particles in the gas is defined as $v_{th} = \sqrt{8k_B T_g/\pi m} = 1256$ m/s at a temperature of 1,200 K. From Gordiets et al.,[18] $\gamma_O \approx 0.98 \times e^{-1780/T_{Wall}}$ is the probability of O-atoms reacting at the wall surface and is equal to 0.01877 at 450 K. Therefore,

$$\frac{2r}{v_{th}\gamma_O} = \frac{2 \times 0.005}{1256 \times 0.01877} = 4.24 \times 10^{-4} \text{ s.}$$

So, the statement that $\Lambda^2/D < 2r/v_{th}\gamma_O$ is valid. Therefore, the wall rate may be written as:

$$k_{Wall} = \frac{v_{th}\gamma_O}{2 \times r} \tag{4.35}$$

The system of steady-state relationships, equations 4.28 to 4.33, is solved using a Mathematica code. The inputs to the Mathematica code are: (1) the rates, as determined by the BolSig+ package; (2) the gas temperature; and (3) the velocity of the gas flow. The measured data and simulated results are shown in Figure 4.19. The $[O_2(a)]$ comes to steady-state in less than 0.5 ms, and the steady-state value is inversely proportional to the pressure in the gas flow.

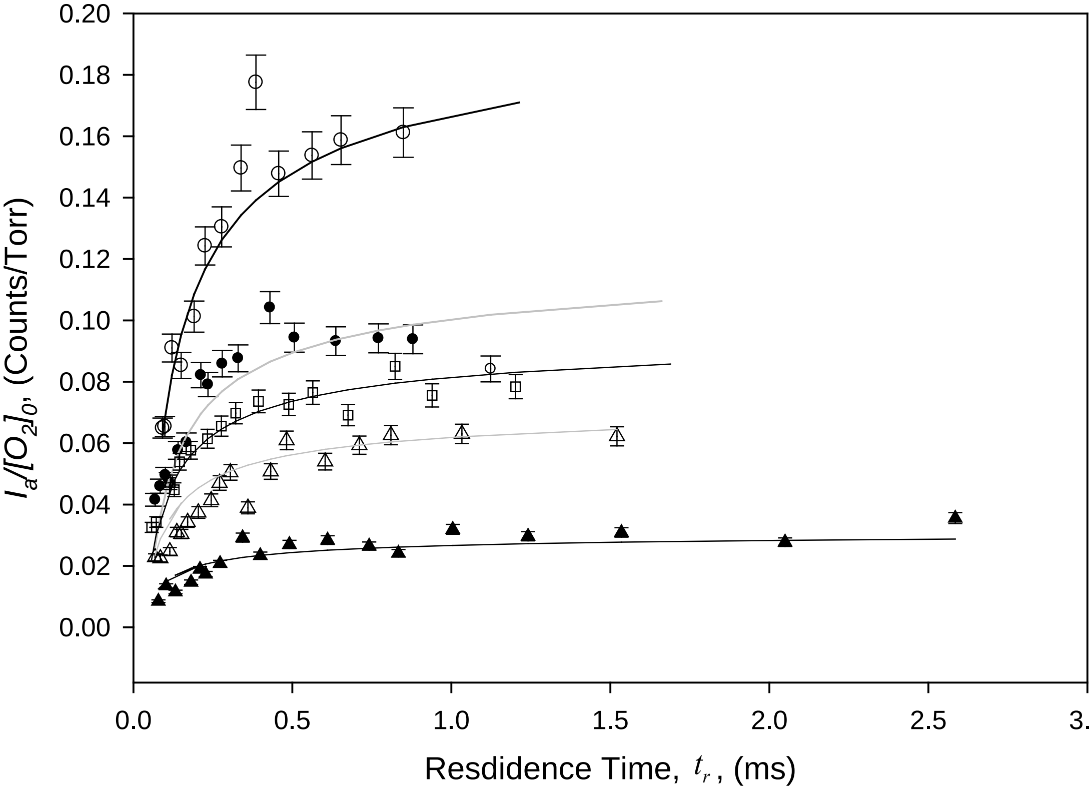

Figure 4.19 Analytic model of the yield of $O_2(a)$ gives a value for Γ_a, which, on average, is 6,000 s^{-1}: ○ 2 Torr, ● 3 Torr, □ 4 Torr, △ 5.2 Torr, ▲ 7.5 Torr, and — theoretical fits from Equation 4.28 at each pressure.

The streamlined set of equations, 4.28 through 4.33, is a small subset of the rate packages used by the majority of the groups publishing in the field.[7, 17, 74] Note that Ionin asserts that a unified set of agreed upon rates is needed in current rate packages.[40] Therefore, the legitimacy of this method will be established by comparison to published results. The two main results used for comparison are those published by Stafford and

Kusher[4] and Rakimova et al.[17] The Stafford[7] paper reports the simulated concentrations of a capacitively coupled RF discharge sustained in a 3 Torr pure oxygen flow. The length of the discharge region is 20 cm; the diameter of the flow tube is 4.83 cm; the gas flow velocity is 1,000 cm/s; and the deposited power is 0.5 W/cm^3.

The results of the streamlined simulation will be compared to the simulated results for O-atoms, $O_2(a)$, electron density, electron average energy, and the E/N of the system. The results reported by Rakimova[17] are for a capacitively coupled RF discharge in pure oxygen of pressures ranging from 2 to 20 Torr. The length of the discharge is approximately 3 cm, the radius of the flow tube is 0.55 cm, the gas flow velocity is 630 cm/s, and the coupled energy ranges from 0 to 1,200 J/mmol or 0 – 12 eV.

In Figure 4.20, the reduced effective electric field, E/N, is plotted versus the flow velocity of a gas for a range of pressures. The E-field is oscillating at a frequency of 2.45 GHz, and the gas flow is pure oxygen. For each pressure, the value of E/N changes by 25% over the range of flow velocities, while the average value of E/N for the pressures changes by a factor of 3.

T_e drives many of the rates included in the model and is determined by the average kinetic energy, ε_{avg}, of the electrons. ε_{avg} as a function of E/N is an output of the BolSig+ code. If these values match those of other reported works, then the rate package included in BolSig+ is adequate, and the E/N values determined within the model are representative of the reported work.

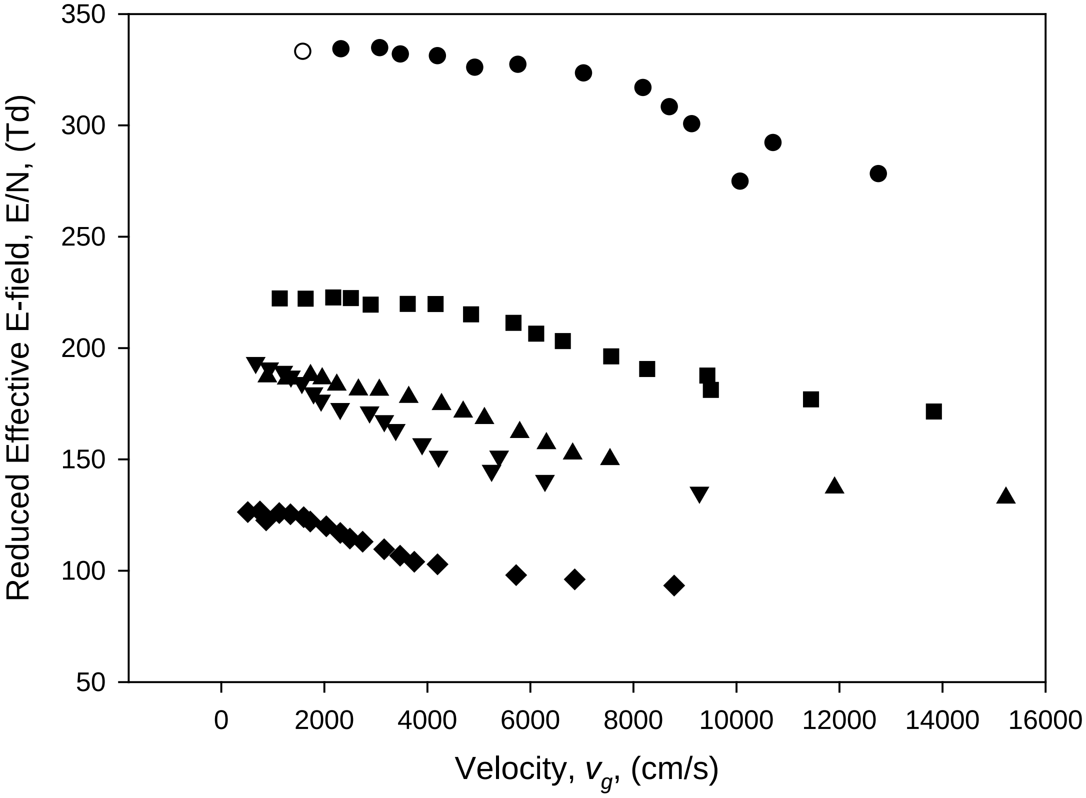

Figure 4.20 E/N as a function of gas flow velocity for 2.45 GHz discharge study performed in this work: ● 2 Torr, ■ 3 Torr, ▲ 4 Torr , ▼ 5.2 Torr, ♦ 7.5 Torr.

Figure 4.21 shows the average electron energies, ε_{avg}, calculated for three different discharges. The simulation presented in this work has been applied to each system. Those results are shown in black. The values published by Stafford[7] and Rakimova[17] are the open points.

The comparison to the Stafford model is excellent, with the values differing only by 0.05 eV. The simulated Rakimova energies range from 3.2 to 2.6 eV, and the analytic simulation ranges from 3.36 to 3.0 eV.[32] Both models predict ε_{avg} values, which decrease as a function of pressure. The simulations reported by Rakimova[17] and

Stafford[7] use Boltzmann solvers developed by those research groups, as opposed to the BolSig+ package used in this study.

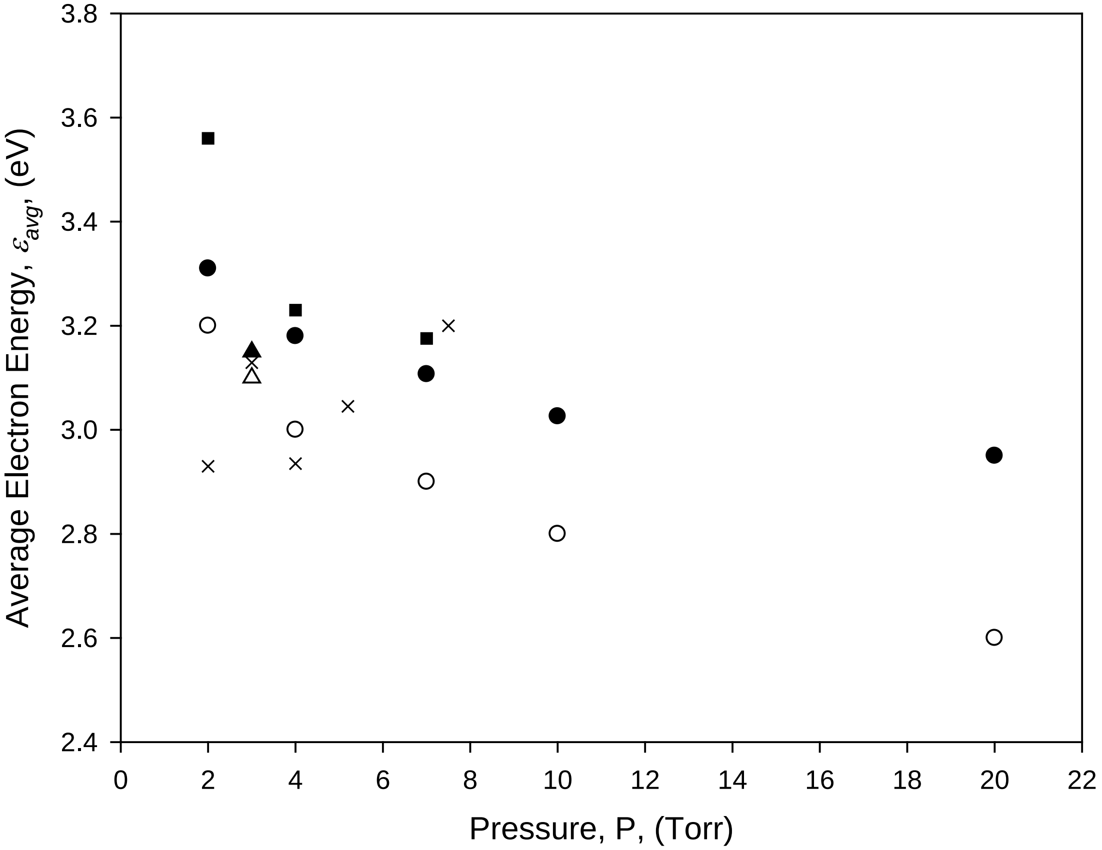

Figure 4.21 Simulated results for average electron energy by ○ Rakimova[17]; ● this work simulation of Rakimova conditions; △ Stafford[7]; ▲ this work simulation of Stafford conditions; ■ this work RF conditions; X this work μ-wave.

The less than 10% error in the absolute values of the electron energies is most likely a consequence of the different Boltzmann solvers used, as well as the different rate packages. The calculated reduced electric field, E/N, for the work reported by Stafford is shown in Figure 4.22.[7]

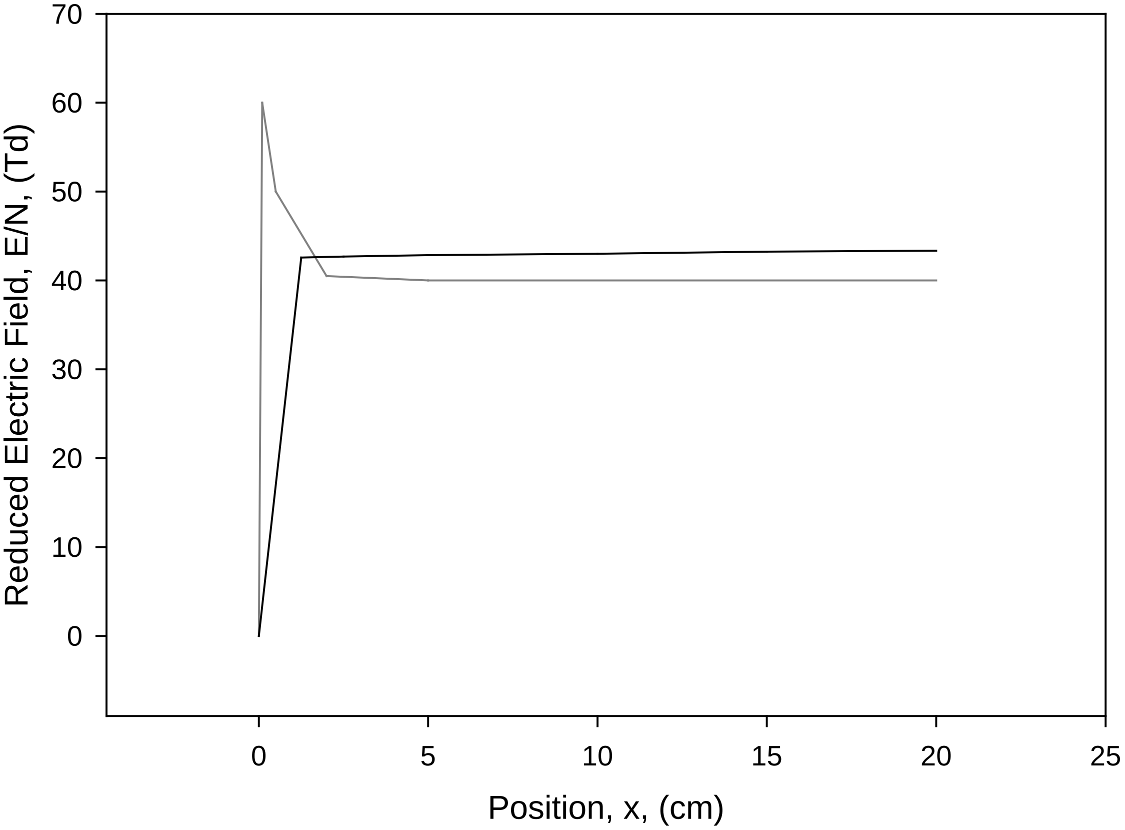

Figure 4.22 Comparison of steady-state E/N as a function of position. (—) this work, (—) Stafford.[7]

The reduced electric field as a function of position is shown in Figure 4.22 and is compared to the reported results of Stafford.[7] The spike in Stafford's E/N is due to his simulation's prediction that the discharge needs a much higher electron density than the results determined by the steady-state model. As a result, Stafford's model predicts a sharp spike in the E/N at the start of the discharge region. In the streamlined model developed for this work, the position, x, within the discharge is not included. Instead, change in distance is modeled by a change in the residence time or gas flow velocity. Hence, a small distance is a short residence time or a large velocity. From Equation 4.33, at large velocities, the energy lost to excited species is significant. Therefore, this term in the power balance equation dominants the values of E/N and therefore the electron temperature. The dominance of the velocity related term explains the change in the discharge conditions at high velocities, short dwell times, or small positions within the discharge. By solving the system of equations at steady state the concentrations vary smoothly as the velocity changes and therefore there is no spike in the E/N at entrance into the discharge. This simulation is appropriate for this work because the discharge is turned on minutes before the measurements are made allowing the discharge to light, thereby eliminating any transient energetics which are included within time dependent models.

Figure 4.23 shows the comparison of the simulated concentrations of O-atoms and $O_2(a)$ (using the Stafford-Kushner model versus the streamlined model), as the gas travels through the discharge region (starting at 0 cm and ending at 20 cm). The conditions used in the streamlined model are the same as those simulated by Stafford and Kushner.[7] The modeled system is an RF discharge operating in pure oxygen. The flow tube has a radius of 4.83 cm, the discharge length is 20 cm, the gas flow velocity is 1,000 cm/s, and the temperature is 400 K, in the discharge. Note that the radius of the flow tube in the Stafford system is 4.83 cm as opposed to the 0.5 cm radii used in this work and the Rakimova study. The large radius increases the value of the volume term in Equation 4.33 thereby decreasing the power loading. Reduced power loading will decrease the rate at which species increase. This explains why the excited specie concentrations continue to change in Figures 4.23 and 4.24 while the E/N is constant.

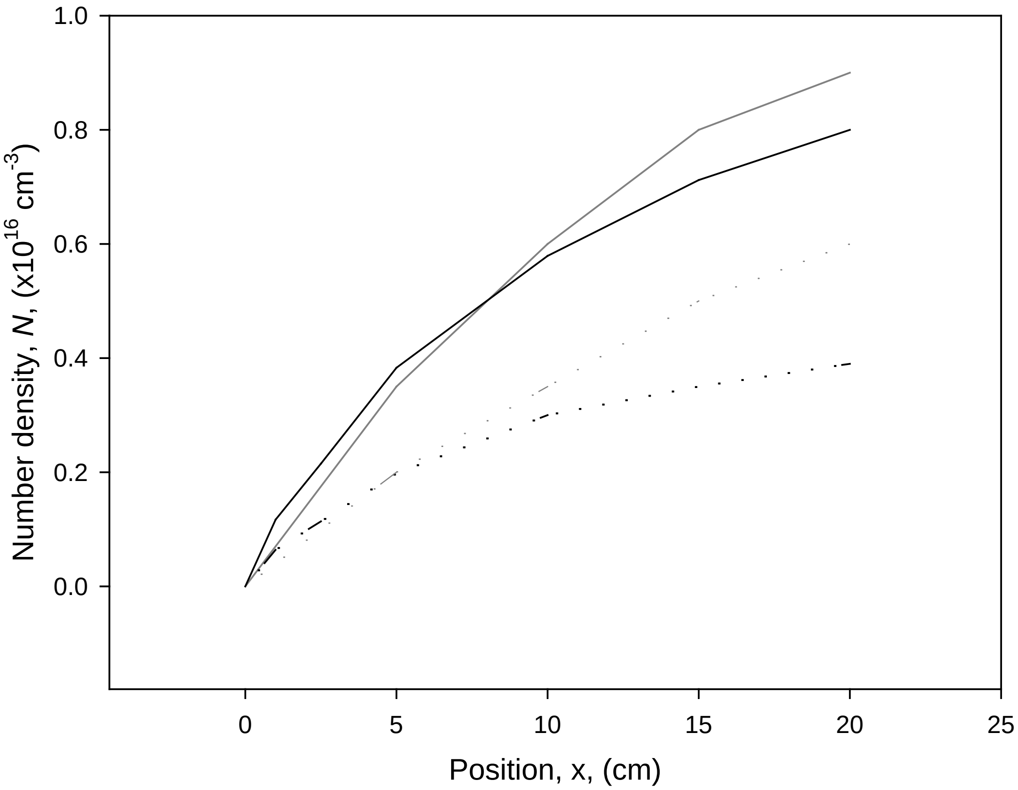

Figure 4.23 Comparison of O-atom and $O_2(a)$ concentrations as a function of position. (RF discharge, 3 Torr, Pin = 0.5 W/cm^3, l = 20 cm, r = 4.83 cm, v_g = 1000 cm/s.) (—) this work O-atoms, (—) Stafford O-atoms,[7] (- -) this work $O_2(a)$, (- -) Stafford $O_2(a)$.[7]

The functional form of the simulations is very similar with a small difference in the rate of curvature. The differences in curvature are related to the destruction and creation pathways included in the Stafford-Kushner model which are not included in the streamlined model. The concentrations at the exit of the discharge are within a factor of 2 making the overall agreement of these models acceptable. The electron densities produced by the two models are also compared.

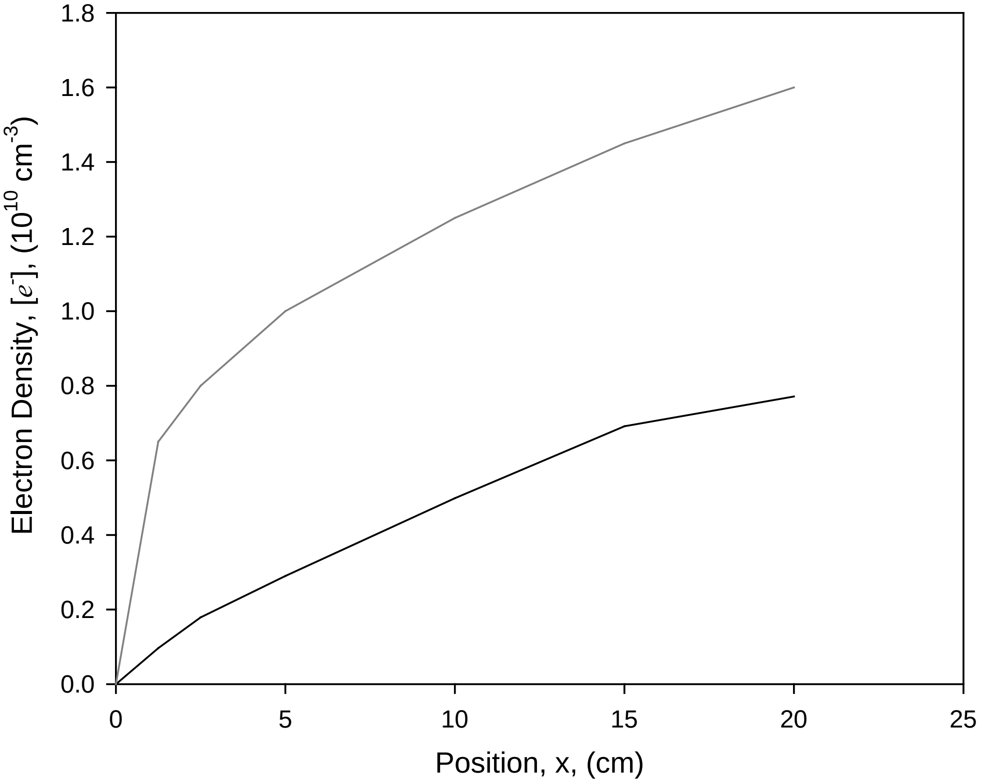

Figure 4.24 Comparison of electron density as a function of position. (RF discharge, 3 Torr, Pin = 0.5 W/cm^3, l = 20 cm, r = 4.83 cm, v_g = 1000 cm/s.) (—) this work, (—) Stafford.[7]

In Figure 4.24, the Stafford results are reported in gray, while the model presented in this study is shown in black. The overall shapes of the two curves are once again very similar; the only difference between the two models is the resultant absolute concentrations, which differ by only a factor of 3.5 or less.

Within this work the steady state value of the electron density is determined using Equation 4.29. Using this equation, electrons are removed from discharge region by dissociative attachment, recombination, and diffusion. If diffusion is the dominant loss mechanism of electrons within the plasma, then the EEDF could be affected by electron collisions at the wall. Using Table 2.1at 4 Torr, T_g = 1,185 K, T_e = 3.2 eV, and a tube radius of 0.5 cm, nominal values for the electron loss reaction rates in Equation 4.29 are:

$$k_{attch} = 1.9 \times 10^{-11}\ cm^3 s^{-1}$$
$$k_{rec} = 1.6 \times 10^{-8}\ cm^3 s^{-1}$$

and the loss rates are:

$$k_{attch} \times [O_2(X)] = 7.6 \times 10^5\ s^{-1}$$
$$k_{rec} \times [e^-] = 50\ s^{-1}$$
$$k_{diff} = 2.7 \times 10^4\ s^{-1}$$

where a nominal ground state concentration of $4 \times 10^{16}\ cm^{-3}$ is used. The electron concentration of $5 \times 10^9\ cm^{-3}$ is used from Rakimova,[17] shown in Figure 4.25. Diffusive losses for electrons is $k_{diff} = D/\Lambda^2 (1+40\ T_e\ (293/T_g))$. The rate of dissociative attachment is an order of magnitude larger than the diffusive losses and therefore the affects of electrons colliding at the wall will not significantly affect the EEDF. In Figure 4.25, simulated electron densities for a number of RF discharges are reported as a function of pressure.

The electron number densities simulated by Rakimova decrease as pressure decreases, while those calculated in this work increase as pressure is lessened. There is some disagreement in the literature as to the behavior of electron densities as a function of pressure.[7, 17, 73, 74] Many studies that report an increase in [e^-] with increasing pressure are performed at a much lower pressure, less then 500 mTorr, and suggest that the direct relationship between electron density and pressure stops or is reversed at higher pressures.[76] The rationale for a decrease in [e^-] as a function of pressure is straight-forward and addressed below.

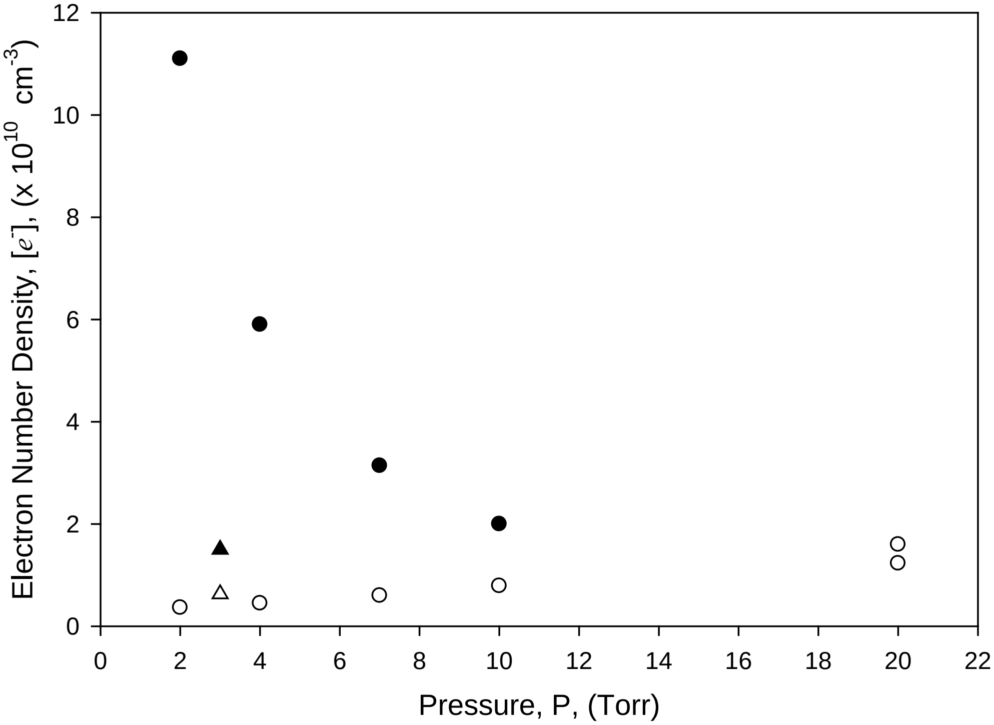

Figure 4.25 Simulated results for [e^-] by ○ Rakimova,[17]● this work (Rakimova conditions), ▲ Stafford,[7] △ this work (Stafford conditions).

4.6.2 Decrease of Electron Number Density as a Function of Pressure

The electron number density, as presented in this work and Rakimova's work, is determined by solving a number of coupled differential equations. Neither study includes a measurement of the electron density. Both models assume that the plasma fills the cross-sectional area of the flow tube in the discharge region. This assumption ignores the tendency of the plasma to concentrate into a toroidal shape, at a higher pressure. (This phenomenon is caused by the reduction in the mean free path of the electrons.) As such, the electron number densities determined by both models are flawed. It is the intent of this section to present material that suggests the feasibility of an inverse relationship between electron density and gas pressure in the flow.

From Figure 4.26, it is apparent that the ionization rate is strongly dependent on the average energy of the electrons. From Figure 4.21, both models simulating the Rakimova geometry show a 10% decrease in ε_{avg} with pressure. From Figure 4.24, the ionization rate increases from a value of $2 \times 10^{10} cm^3 s^{-1}$ at 3 eV to $11 \times 10^{10} cm^3 s^{-1}$ at 3.3 eV. Dissociative attachment, the dominant loss mechanism for electrons, does not change dramatically as will be discussed later in this section. Therefore, it is expected that the electron density will decrease as the pressure of the gas increases. However, Rakimova's work shows an increase in electron density as the gas pressure increases. The source of

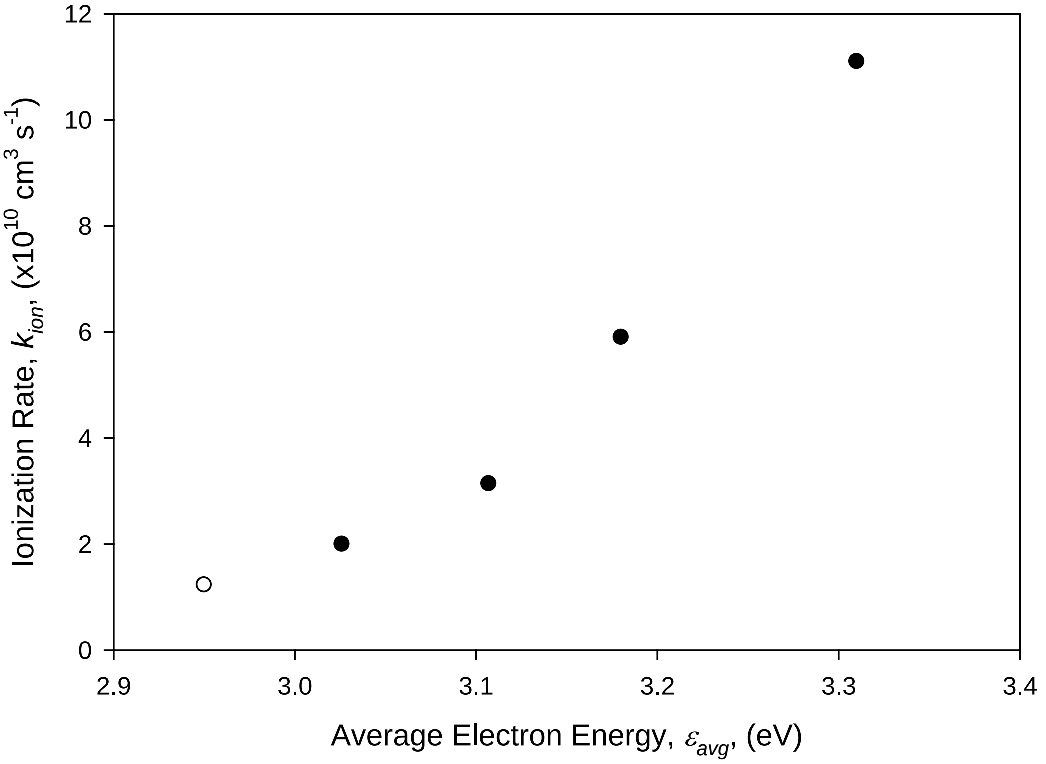

Figure 4.26 Ionization rate, k_{ion}, as a function of the electron temperature, as determined using the BolSig+ model, for a μ-wave discharge at 4 Torr.

electrons at a higher pressure, as reported by Rakimova,[17] is a collisional detachment of electrons from negative ions. The O^- population is produced by attachment and quenched by collisions with O-atoms, $O_2(a)$, and positive ions. Therefore, an increase in the number of collision partners logically results in an increase in detachment.

The mechanism for detachment is shown below:

$$O^- + M \rightarrow O + M + e^- \tag{4.36}$$

where M represents any collision partner in the gas flow. From this expression it may be surmised that as the gas pressure in the flow is increased, and subsequently the number density of collision partners increase, that the electron concentration in the flow will increase. However, to increase [e^-], [O^-] must be the same order of magnitude as [e^-] at lower pressures that will serve as a reservoir of electrons that may be depleted as pressure is increased. Examination of the second order effects of the negative ion density on the electron density follows.

In Figure 4.27, the rate of production of O^- within an RF discharge is shown for a range of average electron energies. The typical ε_{avg} for an RF discharge at pressures over 1 Torr is approximately 3.2 eV. From the chart below, the value is approximately $k_{attch} =$ 2x10^{-11} cm^3 s^{-1}, assuming an upper limit for E/N as 60 Td or ε_{avg} = 4 eV. In order to examine the upper limit of the negative ion concentration, the higher E/N will be used.

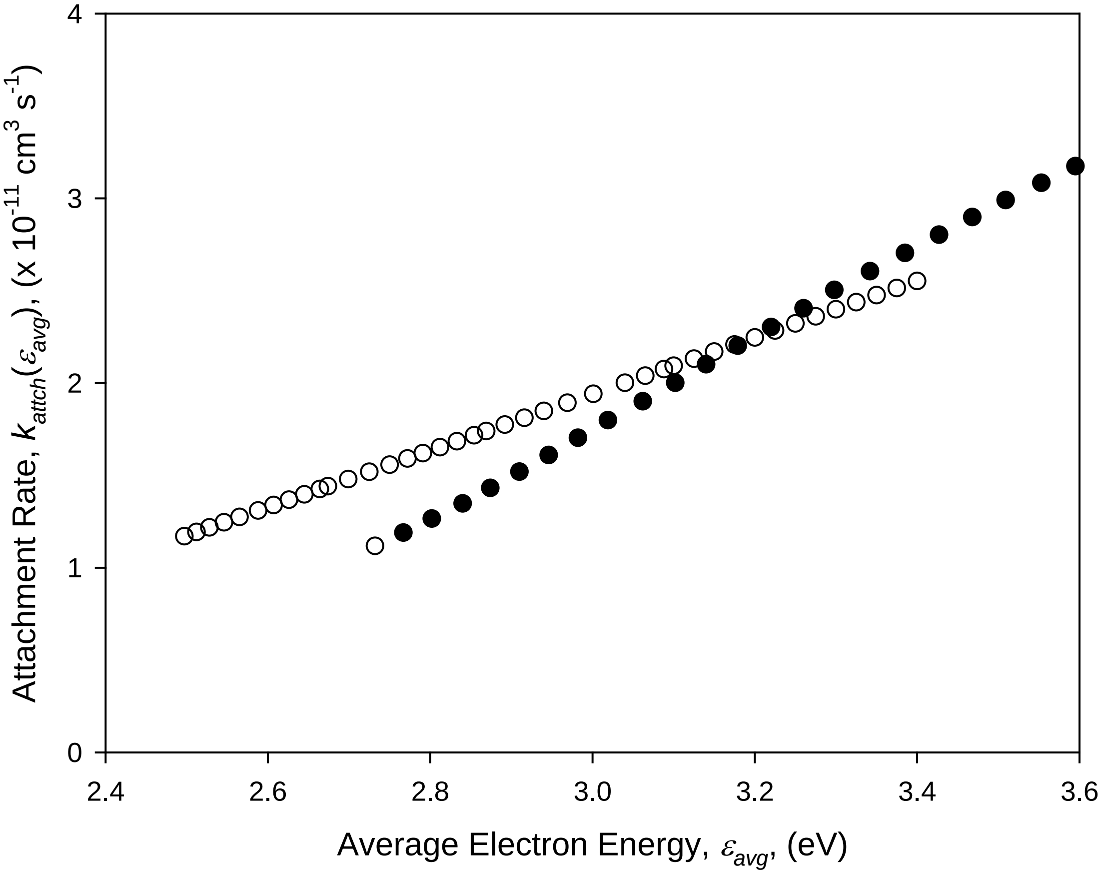

Figure 4.27 Attachment rate in cm^3 s^{-1} plotted versus average electron energy (eV). ● μ-wave. ○ RF.

The solution to the concentration of O^- within the discharge, assuming quasi-neutral discharge at steady-state, having a gas temperature of 1,000 K, is governed by the reactions below:

$$\left[O^-\right]_{ss} = \frac{k_{attch}\left[e^-\right]_{ss}\ \left[O_2(X)\right]_{ss}}{k_{rec}\left[O_2^+\right]_{ss} + k_{aneg}\left[O_2(a)\right]_{ss} + k_{Oneg}\left[O\right]_{ss}} \tag{4.37}$$

$$\left[O^-\right]_{ss} \approx \frac{3\times10^{-11}\left[10^{10}\right]\ \left[10^{16}\right]}{2.98\times10^{-8}\left[10^{10}\right]\ +1.2\times10^{-9}\left[10^{15}\right]+8\times10^{-10}\left[10^{15}\right]} \tag{4.38}$$

$$\left[O^-\right]_{ss} \approx \frac{4\times10^{15}}{1.2\times10^{6}} \approx 3\times10^{9} \tag{4.39}$$

The approximate value for the $[O^-]_{ss}$ value is roughly an order of magnitude smaller than the electron density. This approximate value was calculated assuming a large value for the attachment rate and that both the $O_2(a)$ and O-atom population are 1%. With a large ε_{avg}, production is at a maximum, and, with small concentrations of O and $O_2(a)$, quenching of O^- is small regarding actual plasma conditions. Even after assuming artificially large production terms and small quenching terms, the O^- population could only reach 10% of the electron density. If all of the O^- present within the discharge is collisionally relaxed, producing free electrons, then the total increase in the electron density would be 10%. As the pressure increases from 2 to 20 Torr, the ε_{avg} decreases from 3.2 to 2.6 eV, causing a reduction in the ionization rate of greater than 50%. Therefore, including the 50% decrease in electron density caused by reduction in the rate of ionization and the 10% increase due to increased detachment, the overall change to the electron density as pressure increases should be a reduction of 40%.

4.7 O-atoms within the Discharge

One of the major differences in the effluence of a chemically driven SOG and a SOG driven by an electric discharge is the production of atomic oxygen. As shown in Figure 2.5, the EEDF within a discharge has a high-energy tail, hence, there are a finite number of electrons with enough energy to dissociate an oxygen molecule. Also, if significant percentages of metastable states, such as $O_2(a)$, are maintained in the discharge, then these excited states will also be dissociated by electrons with energies less than 6.0 eV,[28] which is the energy necessary to dissociate an oxygen molecule. O-atoms are also created by dissociative attachment, reaction 2, which has a threshold energy of approximately 3 eV. O-atoms introduce reaction pathways that do not exist in the chemistry based oxygen-iodine laser system and may reduce the $O_2(a)$ population and I* concentration. If O-atoms reach a significant population, they could influence the EEDF and change the reaction rates determined by using the BolSig+ code in a pure oxygen gas flow. In order to verify that the O-atom concentration is small enough not to affect the EEDF, O-atom concentrations have been measured. Note that the effect of O-atoms on the EEDF has been added to the BolSig+ model, assuming that the O-atom concentration makes up less than 10% of the discharge. (The assumption that O-atom concentration is less than 10 % will be validated by actinometry measurements in section 4.7.1.) This has been accomplished by adding O-atom cross-sections, from Laher et al.,[84] to the BolSig+ library, scaling the cross-sections to reflect that [O] = 10% of $\left[O_2(X)\right]$ and recalculating the EEDFs. The result is that there is less than a 3% change in the production rate of $O_2(a)$. Because the error in the determination of yield is approximately 20%, it will be assumed that the change in the rate is negligible if the population of O-atoms is less than 10%.

Measurement of the O-atom population is accomplished by using the established method of actinometry, which was discussed in Section 2.8. Measured populations for this study's microwave discharge will be discussed in the contexts of existing literature, and any ramifications will be examined.

4.7.1 Actinometry

From Pagnon,[38] the [O] may be determined from the ratio of $I_{0844nm}/I_{Ar750nm}$ by the relationship shown in Section 2.8, Equation 2.30. The emissions of I_o and I_{Ar} that result from a microwave discharge operating at 85 W, 800 SCCM, and 10% argon in the flow are measured and shown in Figures 4.28 and 4.29. The emission from the argon centered at 750.4 nm is the result of the transition, $^2P_{1/2}$ *4p* (0.99eV) - $^2P_{1/2}$ *4s* (0.87eV).

The peak centered at 751.5 nm is a result of the transition from $^2P_{3/2}$ *4p* (0.97eV) - $^2P_{3/2}$ *4s* (0.85eV). The measurements in this work show that O-atoms make up less than 5% of the gas flow in an apparatus with a radius of 0.5 cm for a μ-wave discharge, Figure 4.30. The Rakhimova measure shows that O-atoms make up about 5% of the gas flow in a RF discharge.[17] The argon emission line is at 750.4 nm, and the atomic oxygen line at 844.6 nm are the primary lines used for the actinometry detection method. Using the actinometry technique, the degree of dissociation, as measured by Ivonov,[77] is 2%. The streamlined model predicts a value of 5% under the Ivonov conditions. Other reported yields of O-atoms are: Stafford 20%,[7] Sharma 0.2%,[78] Rakihmova 5%,[17] and 5 ± 0.5% in this study.

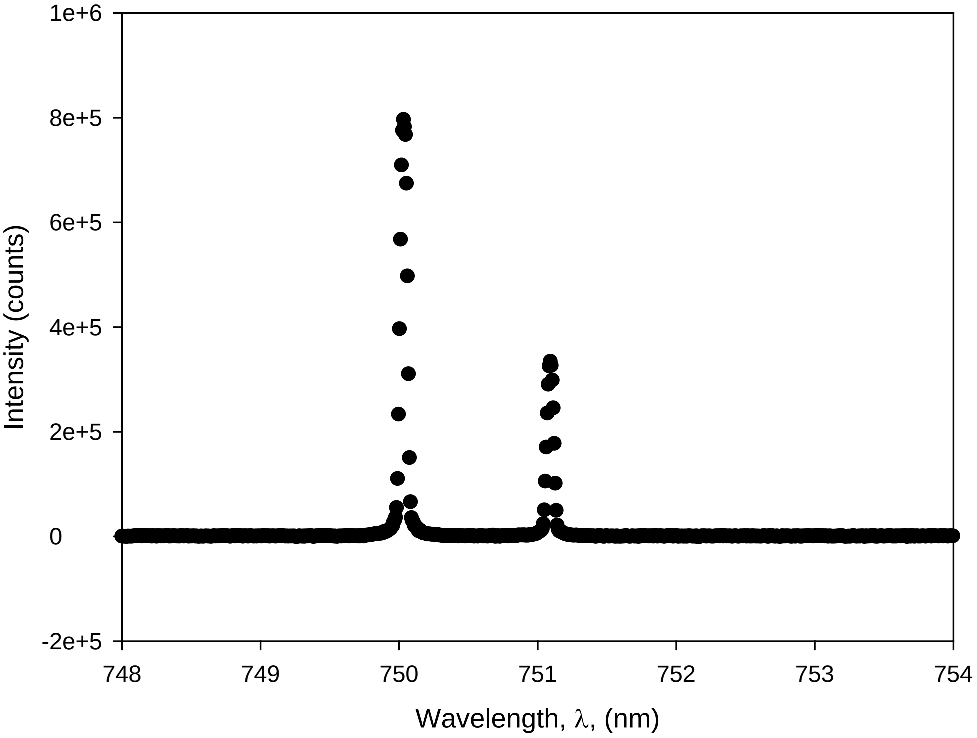

Figure 4.28 Emissions of argon from the electric discharge.

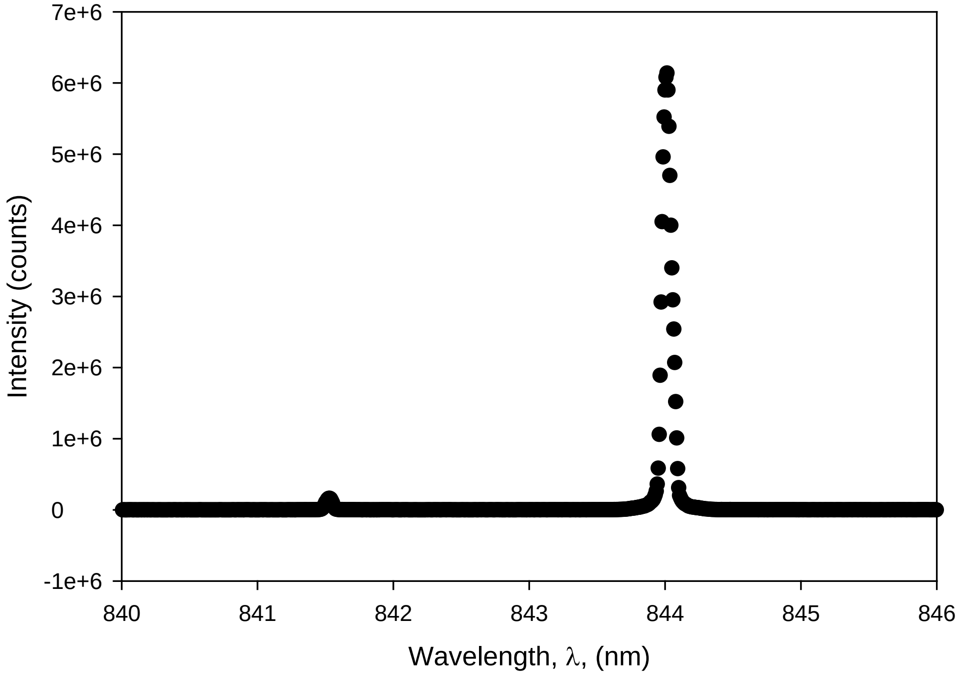

Figure 4.29 Emission from O-atoms centered at 844 nm.

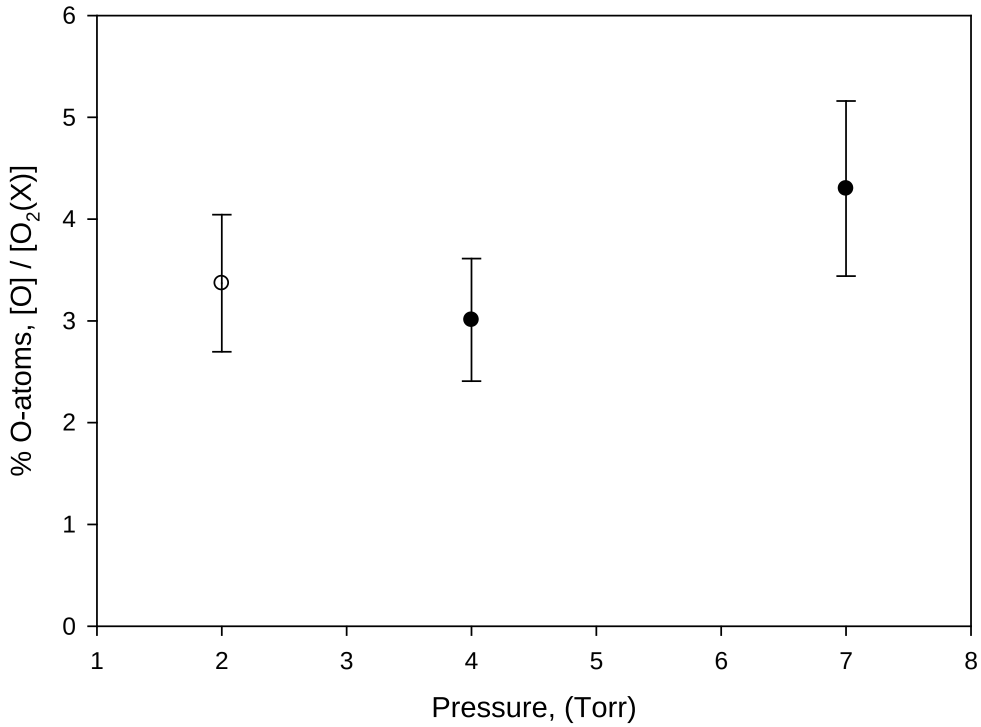

Figure 4.30 Measured percentage of the gas flow, which is made up of O-atoms within a 2.45 GHz discharge at three pressures, 2, 4, and 7 Torr.

The actinometry measurement agrees with the simulated results, as well as those reported in the literature for similar discharge conditions. As previously mentioned, it will be assumed that a yield of O-atoms, less than 10%, will have no effect upon the electron energy distribution. Therefore, the BolSig+ results are accurate for the continued simulation of this work.

4.8 Results and Discussion of O_2(a) Data

The results found from the literature (shown in Figure 2.14) and the measurements in this work (shown in Figure 4.18) both exhibit a decrease in the yield of $O_2(a)$ as pressure increases. In order to describe the behavior of the reduction of the

$O_2(a)$ concentration, a pseudo-first order decay rate, Γ_a, has been introduced to the steady-state solution of the $O_2(a)$ excited state. The behavior of Γ_a will be used to asses a destruction mechanism for the $O_2(a)$ state.

4.8.1 Inclusion of Pseudo-First Order Decay Rate

The concentration of $O_2(a)$ as a function of gas pressure and flow velocity has been measured by monitoring the optical emissions centered on 1260 nm. The yields calculated from these measurements show an inverse relationship to the oxygen pressure within the flow. The steady state equation used to describe the $O_2(a)$ concentration within the discharge includes a pseudo-first order decay rate. Obtaining values of Γ_a using the steady state equation in combination with the yields of $O_2(a)$, will permit an assessment of the destruction mechanisms of $O_2(a)$ within the discharge. Calculation of the first-order decay rate for a range of flow velocities and gas pressures follows.

In Equation 4.28, the steady-state solution of $O_2(a)$ includes a pseudo-first order decay rate denoted by the symbol Γ_a. The values of Γ_a are determined by solving the steady-state equation for Γ_a:

$$\Gamma_a = \frac{k_{a+}\left[e^-\right]_{\mathrm{ss}}\left[O_2(X)\right]_{ss}}{\left[O_2(a)\right]_{ss}} - k_{a-}\left[e^-\right]_{ss} \tag{4.40}$$

Note that the fraction $\left[\mathrm{O_2(X)}\right]_{\mathrm{ss}} / \left[\mathrm{O_2(a)}\right]_{\mathrm{ss}}$ is present in Equation 4.40. This value is the inverse of the yield of $O_2(a)$, Y_a, which is determined from the measured intensity of the $O_2(a)$ emissions, I_a:

$$Y_a = \frac{[O_2(a)]_{ss}}{[O_2(X)]_{ss}} = \frac{I_a}{[O_2(X)]_{ss}} \times k_Y \qquad (4.41)$$

Using equations 4.28 through 4.33, there is a system of six equations with seven unknown values, including Γ_a as an unknown. By including Equation 4.41 as the solution for the steady-state value of $O_2(a)$, the system of equations may be used to obtain values of Γ_a.

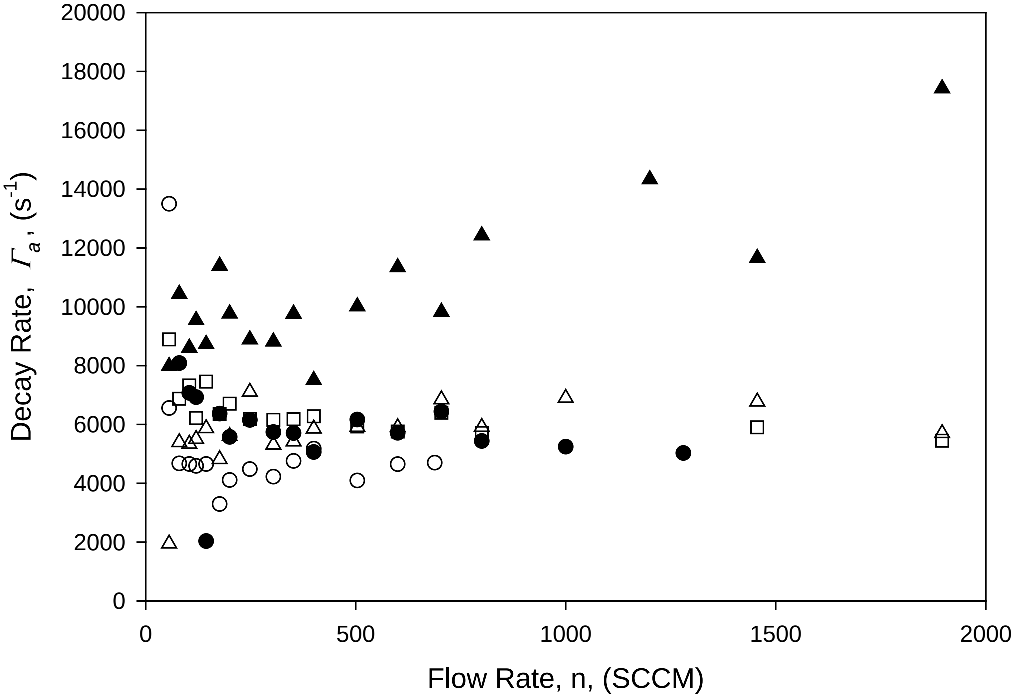

Figure 4.31 **Γ_a as calculated for each datum measured with a μ-wave discharge as a function of flow rate for the pressures: ○ 2 Torr, ● 3 Torr, ☐ 4 Torr, △ 5.2 Torr, ▲ 7.5 Torr.**

Figure 4.31 shows the values of Γ_a determined for pressures ranging from 2 to 7.5 Torr and mass flow rates varying from 10 to 1,800 SCCM. By averaging the value of Γ_a over the range of flow velocities, an average value of Γ_a is calculated for each pressure. These average values vary with pressure, as shown in Figure 4.32. The average values of gamma, ${}^{avg}\Gamma_a$, are near 6,000 s^{-1} for μ-wave discharges, with the exception of the values for 2 Torr and 7.5 Torr.

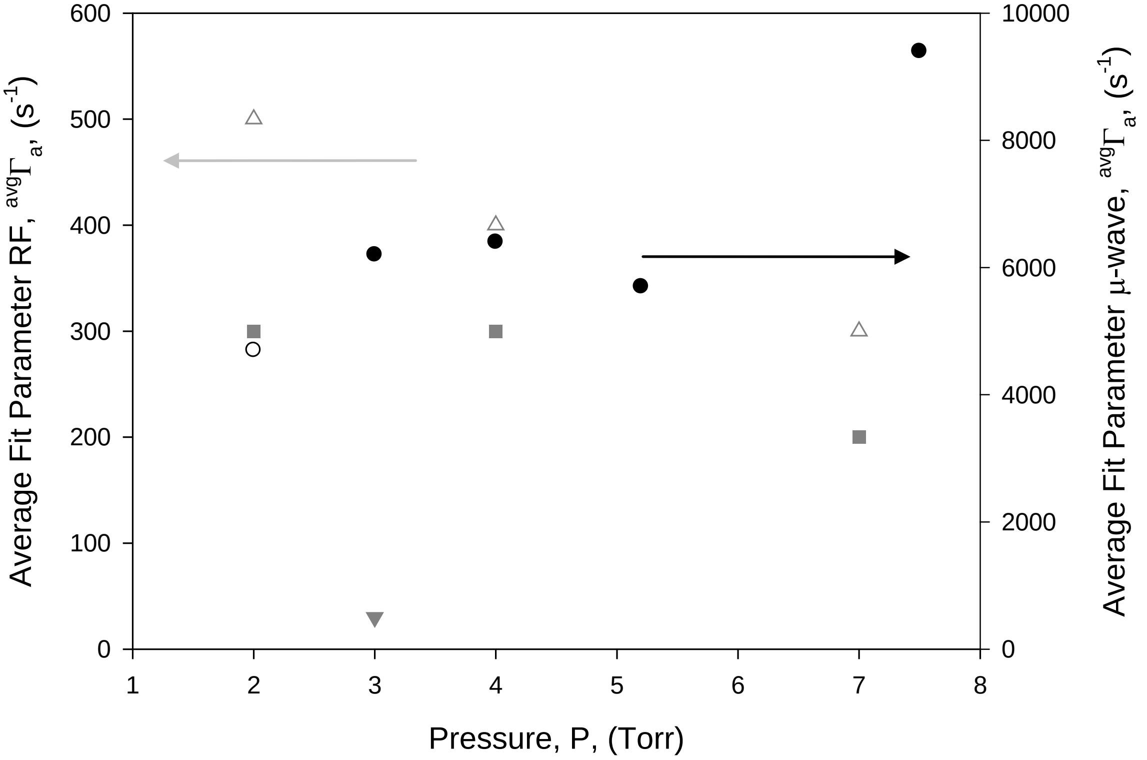

Figure 4.32 Average value of Γ_a as a function of pressure. ● μ-wave conditions for 2-7.5 Torr, △ RF conditions (this work), ■ RF conditions (Rakimova),[17] and ▼ RF conditions (Stafford).[7]

Figure 4.32 shows that the decay rate for RF discharges is an order of magnitude less than those values calculated for microwave discharges. This relationship is telling with regard to any suggested mechanism. The behavior of Γ_a as a function of flow velocity, E-field oscillating frequency, and gas pressure will be used to examine candidate kinetic mechanisms responsible for limiting the yield of $O_2(a)$.

By changing the frequency of the oscillating field from a microwave frequency to RF, the average electron energy, ε_{avg}, changes by 0.2 eV or less, as shown in Figure 4.21.

The small change in ε_{avg} has a relatively minor effect upon most of the reaction rate coefficients in this energy region, as shown in shaded areas of Figures 2.6 and 2.7. A closer look at the rates important to production and destruction of electrons is shown in Figure 4.33.

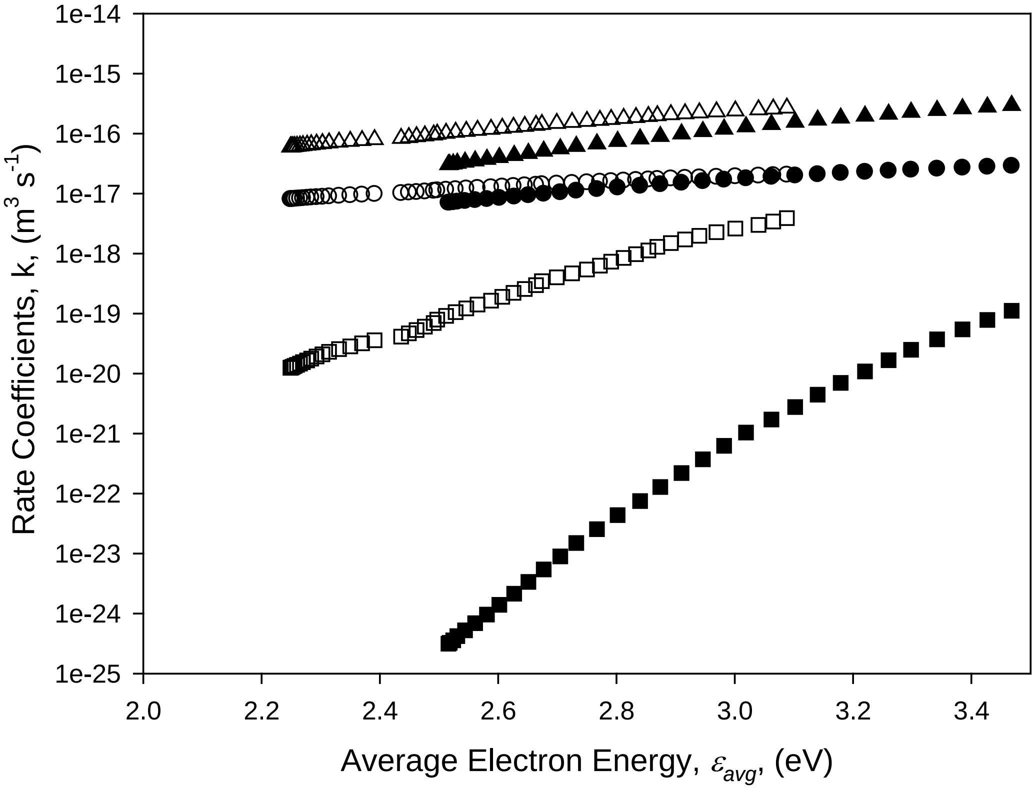

Figure 4.33 Reaction rate coefficients at 3 Torr for ○ dissociative attachment μ-wave, ● dissociative attachment RF, △ dissociation μ-wave, ▲ dissociation RF, □ ionization μ-wave, ■ Ionization RF (from BolSig+).

However, the ionization rate, k_{ion}, varies strongly as a function of ε_{avg} in this energy region. As shown in Figure 4.33, this rate increases by an order of magnitude or greater when changing from RF to μ-wave frequencies. Because there is an order of magnitude difference in Γ_a between the RF and microwave discharges, the mechanism responsible for quenching $O_2(a)$ is probably related to the ionization rate and, most likely, the electron density. In Figure 4.34, the k_{ion} at 4 Torr is shown for both RF and microwave frequency electric field, as determined by using the BolSig+ code.

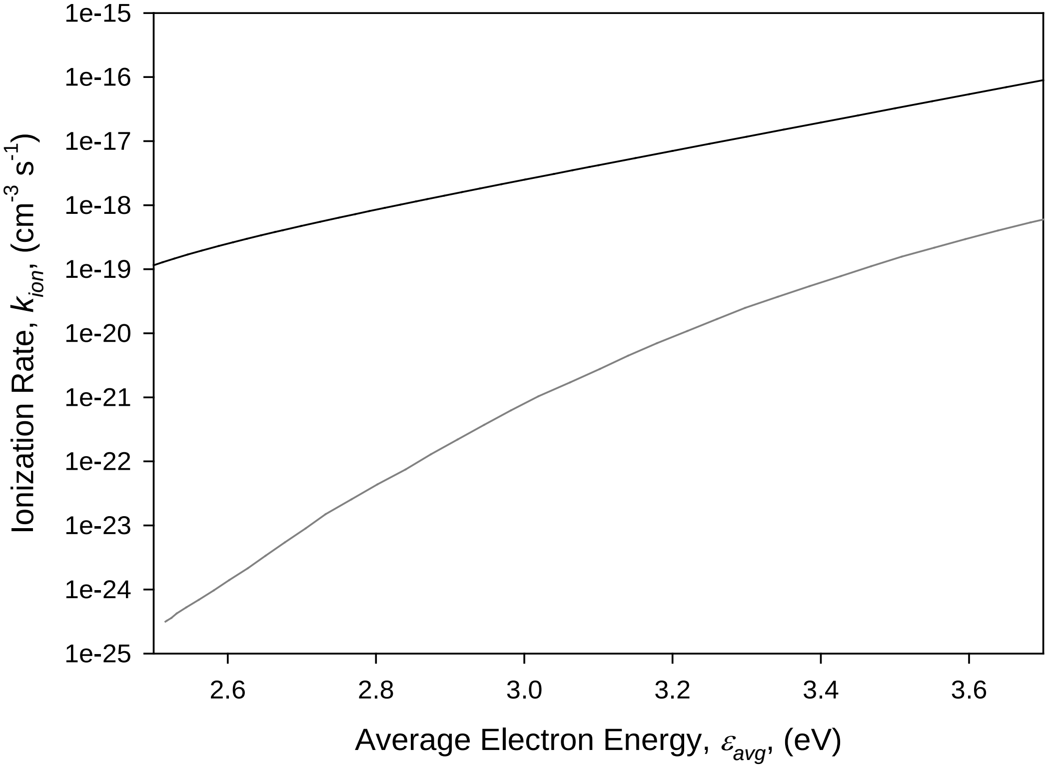

Figure 4.34 Ionization rate versus average electron energy for ▬ μ-wave frequency and ▬ RF discharges at 4 Torr, T_g = 1,100 K (from BolSig+).

The dimensions of the discharge used to produce Figure 4.34 are a flow tube diameter of 1 cm, the length of the discharge region of 3.2 cm, and the average electron energy ranges from 2.5 to 3.7 eV, which is the range of ε_{avg} studied in this work.

Figure 4.35 shows the near linear dependence of the pseudo-first order decay rate divided by the steady-state concentration of oxygen in the ground state, $\Gamma_a / [O_2(X)]_{SS}$, on the $\left[e^{-}\right]_{ss}$. This argues for a quenching mechanism that is dependent on $\left[e^{-}\right]_{ss}$ multiplied by $\left[O_2(X)\right]_{ss}$.

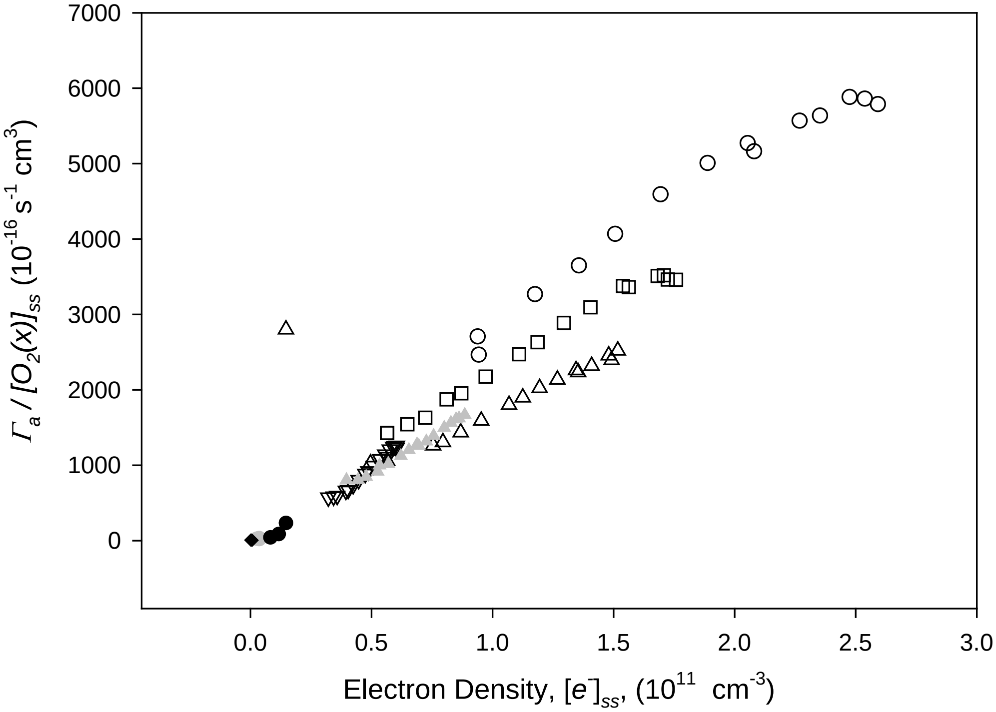

Figure 4.35 Relation of Γ_a / $[O_2(X)]_{ss}$ versus $[e^-]_{ss}$. ○ 2 Torr, □ 3 Torr, △ 4 Torr, ▲ 5 Torr, ▽ 7 Torr, ● current work RF 2, 4, and 7 Torr, ♦ Stafford RF[7], ♦ Rakimova RF. [17]

The electron densities are determined by using the streamlined computer simulation, using equations 4.28 through 4.33. From the near linear relationship shown in Figure 4.35, the dominant mechanism for limiting the $\left[O_2(a)\right]_{ss}$ must be of the form:

$$\Gamma_a = \Sigma_a \left[e^{-}\right]_{ss} \left[O_2(X)\right]_{ss} \tag{4.42}$$

where Σ_a is the rate coefficient required for this reaction mechanism. As governed by the power balance equation, Equation 4.33, the $\left[e^{-}\right]_{ss}$ and $\left[O_2(X)\right]_{ss}$ are inversely related, making their product invariant with residence time.

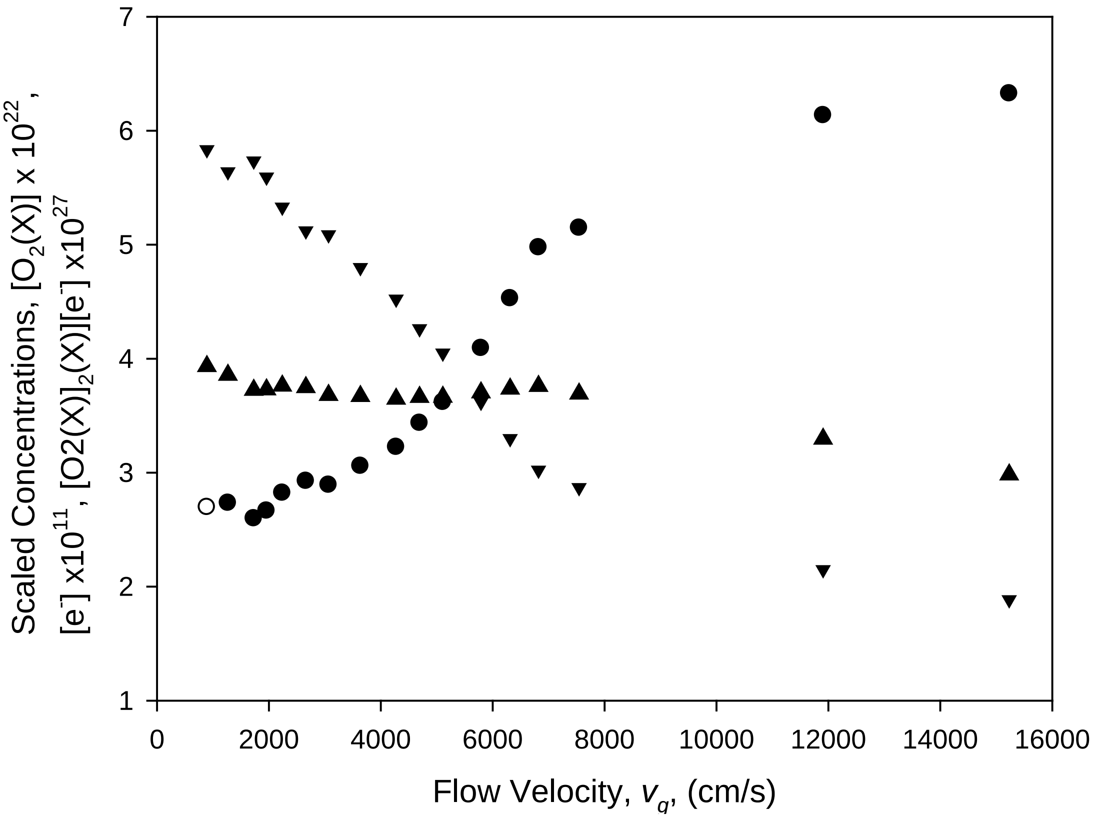

Figure 4.36 The ground state and electron densities are shown in the plot above, including the product of the two concentrations as a function of flow velocity at 4 Torr. ● [$O_2(X)$],▼ [e^-], ▲ [$O_2(X)$] · [e^-].

The relationship between the electron density and ground state density is shown in Figure 4.36. Two key characteristics of the dominant quenching mechanism of $O_2(a)$ have been identified. First, $\Gamma_a/[O_2(X)]_{SS}$ is linear with electron concentration, and second, Γ_a in an RF field is significantly smaller than in the presence of a microwave frequency field. These characteristics are used to explore possible mechanisms responsible for destroying $O_2(a)$.

4.8.2 Brief Synopsis of Results

A systematic study of microwave discharges has been performed through the pressure range of 2 to 7.5 Torr in pure oxygen flows. Both RF and μ-wave frequencies have been studied. Optical spectroscopy has been used to monitor the change in the $\left[O_2(a)\right]$, $\left[O_2(b)\right]$, and $\left[O\right]$ concentrations as a function of pressure and gas flow velocity. A technique involving spectroscopy, gas flow velocity, and careful analyses of the gas temperature has been developed and used to observe the excited species directly within the discharge region. In the literature, experimental measurements of excited effluent from discharges are typically performed many centimeters downstream of the discharge. When optical diagnostics are used immediately outside of the discharge or within the discharge, the intensity of the emissions is strongly affected by the gas temperature. Because of this dependence, an elegant method has been developed to precisely determine the temperature of the gas in the discharge region.

The gas temperature measurements reported in this work have been extracted from the rotational energy distribution of the excited $\left[O_2(b)\right]$ state. The resolution of the $\left[O_2(b)\right]$ spectral data reported in this study has a resolution of 0.01 nm, while the most precise resolutions reported in the literature is 0.04 nm. Higher resolution spectra allow the determination of the gas temperature to a higher degree of precision. Typical errors in reported gas temperatures for this study are 5% or less, whereas errors in gas temperature reported in the literature are typically 10% or greater. Because the gas temperature influences the intensity of the emissions from all of the measured species, higher precision temperature determination results in higher precision density measurements. The high-resolution gas temperature measurements performed in this study improve the quality of the reported data by approximately 10% throughout this work.

The primary purpose of the gas temperature measurement is to obtain an accurate measurement of $\left[O_2(a)\right]$ using optical intensities. An understanding of the gas temperature also permits a brief commentary upon thermal transport within the discharge and the affects it has upon EOIL systems. The steady state temperature, T_{ss} = 1182 ± 10, is significantly lower than anticipated if heat transfer to the wall or flow of excited species out of the discharge is not considered. The fit result $f = 0.17 \pm 0.02$ implies most of the discharge power does not raise the gas temperature. The analysis presented in Appendix B indicates that significant power is transferred to the reactor walls via atomic oxygen reactions. The reactor wall requires active cooling with compressed air to prevent glass softening. Indeed, thermal control and surface reactions appear important in most EOIL demonstrations.

$\left[O_2(a)\right]$ emission intensity measurements made within the discharge region have been reported. Four atomic species present in the electric discharges emit in the same spectral region, from 1,250 to 1,300 nm, as the $\left[O_2(a)\right]$ state. These atomic emissions are from high-energy, 13 eV, or ionic O-atoms, which are not observed downstream of the discharge but have sufficient concentrations within the discharge region. By using a computer model, the intensity contributions of these emissions are separated from the reported $\left[O_2(a)\right]$ emission intensities. Using the computer model allows $\left[O_2(a)\right]$ intensity measurements made directly inside the discharge region to reflect the concentration of the $\left[O_2(a)\right]$ state without introducing errors that result from changes in the atomic oxygen. Using the model to reproduce the $\left[O_2(a)\right]$ emissions permitted the identification of both the 0-0 and 1-1 vibrationally excited transition of $\left[O_2(a)\right]$. The intensity of the 1-1 transition is sufficient to determine a temperature that agrees well with the rotational temperatures reported. Identification of these emissions within the discharge has not been previously reported.

The interpretation of the measured $\left[O_2(a)\right]$ yield, using a streamlined, nearly analytic model, cast new light on the determination of the kinetics within the electric discharge. Over the range of pressures studied, the values of Γ_a are invariant as a function of the flow velocity of 800 to 15,000 cm/s. The quenching rate at μ-wave frequency field oscillations ranges from Γ_a = 4,000 to 9,000 s^{-1}, while the values range from Γ_a = 400 to 600 s^{-1} for RF fields. The only rate that changes significantly between the two different field oscillation frequencies is the rate of ionization.

From the steady-state simulation, it has been determined that the product of $\left[e^-\right]\times\left[O_2(a)\right]$ is approximately constant. As the velocity of the gas is increased, the temperature of the gas in the flow decreases. The concentration of $O_2(X)$ is inversely related to the temperature of the gas and, hence, changes dramatically as the residence time of the gas is changed. This requires a subsequent change in the electron density. The primary kinetic pathway that changes as the velocity changes is the ionization rate. As the concentration of the ground state increases, the ionization rate drops; therefore, the electron density drops, allowing the product of the two species to remain constant over a large range of discharge conditions.

V Discussion

Through this comprehensive study of the behavior of excited species within an electric discharge of flowing oxygen in both RF and μ-wave frequency E-fields, a few truths may be stated. First, the intensity of the $O_2(a)$ emissions, I_a, obtains a steady-state value after residing within the discharge region for approximately 0.3 ms. This residence time corresponds to 3 eV/ particle, consistent with the observations of Rakhimova.[17] The modeled results of Stafford and Kushner[7] suggest that the $O_2(a)$ concentration peaks at 6 eV/ particle and is limited by the dissociation of the ground state oxygen. When O-atom concentrations make up more than half the flow and the ground state concentrations diminish, then the production of $O_2(a)$ by Reaction 10 of Table 2.1 is reduced. However, the measured results of $O_2(a)$ in this study and Rakhimova's study[7] reach a steady value at a lower energy deposition than predictions,[17] suggesting there is a mechanism for quenching $O_2(a)$ that is not currently included in simulations. This destruction pathway will limit power scaling in EOIL systems, because, when increasing deposited energy, higher yields of $O_2(a)$ will not be obtainable, presumably because the quenching species will also be created at a higher concentration.

Secondly, it is observed in a large number of different studies that the yield of $O_2(a)$, Y_a, decreases as the pressure of oxygen is increased within the discharge. However, high yields of $O_2(a)$ have been achieved at high total gas pressures when the partial pressure of oxygen was small. This result further identifies the destruction mechanism as being tied to the existence of oxygen within the gas flow. Hence, the destruction mechanism is not related to collisions with the carrier gas, argon, or an excited species of argon.

A steady-state description of the $O_2(a)$ concentration has been used to further describe the behavior of the destruction term of $O_2(a)$, which is seen in Equation 4.28. The resulting values of the quenching term, Γ_a, do not change significantly over the pressure range, 2 to 10 Torr, and residence time, 0 to 3 ms. Therefore, whatever mechanism results in the destruction of the $O_2(a)$ within the discharge must also remain unaffected by changes in the gas pressure and flow velocity of the gas. The magnitude of Γ_a for the μ-wave case is 6,000 s^{-1}. Because Γ_a must be the product of a rate coefficient and the concentration of the quenching species, the magnitude of Γ_a restricts reactions that may be responsible for the observed behavior of $O_2(a)$. For instance, a species that makes up 10% of the gas flow at 2 Torr and a steady state gas temperature of 1200 K has a concentration of approximately 1 x 10^{16} cm^{-3}. In order for the product of the destructive species and the reaction rate coefficient to equal 6,000 s^{-1}, the rate coefficient of this reaction must be 6 x 10^{-13} cm^3 s^{-1}. Furthermore, the Γ_a values derived from the RF measurements are 500 s^{-1}. In summation, the quenching mechanism must be invariant to changes in pressure and flow velocity, while changing by an order of magnitude when the frequency of the E-field is changed from 2.45 GHz to 13.56 MHz.

The criteria for the quenching mechanism of $O_2(a)$ is very specific, many species commonly thought to limit the production of $O_2(a)$ within the discharge do not meet these criteria. There is one relationship that does meet the criteria. $\left[e^{-}\right]\times\left[O_2(X)\right]$ is invariant with respect to gas pressure and flow velocity. Also, the ionization rate changes by an order of magnitude between RF and μ-wave frequencies. Furthermore, the reactions responsible for reducing the electron density, namely, recombination, diffusion, and dissociative attachment, do not change significantly when the frequency of the E-field changes. Note that the dominant loss mechanism of electrons is dissociative attachment. Dissociative attachment has a rate that is an order of magnitude larger than diffusive losses under the conditions studied in this work. Under these conditions the electron densities will not be affected by interactions at the wall. Because the electron production rate decreases by an order of magnitude and the loss rates do not, it is reasonable to expect the electron density to decrease by an order of magnitude when the frequency of the E-field changes. So, if the concentration of the excited species, [*M*], responsible for quenching $O_2(a)$, is dependent on the product of $\left[e^{-}\right]\times\left[O_2(X)\right]$, then it should be invariant with pressure and gas flow velocity, making it a prime suspect for quenching $O_2(a)$, providing the reaction rate and concentration are large enough.

5.1 Evaluation of $O_2(a\ ^1\Delta)$ Destruction Mechanisms

In Table 5.1, six candidate reactions are listed that may be the dominant destruction pathway of the $O_2(a)$ state. Reactions 22-25 are mentioned by Stafford as possible dominant quenching reactions. Reaction 26 is deactivation by direct electron impact, which is included for completeness. The final reaction (reaction 27) is a new candidate for quenching of $O_2(a)$ introduced in this work.

Table 5.1 Possible quenching reactions responsible for limiting Y_a.

Reaction Number	Reaction	Reaction Rate Coefficient cm^3 s^{-1}	Ref
22	$[O_2(a)]+[O_2(X)]\rightarrow 2[O_2(X)]$	$k_{O2x}=3.0\times10^{-18}e^{-200/T_g}$	29
23	$[O(^3P)]+[O_2(a)]\rightarrow O+[O_2(X)]$	$k_{aO}=2.0\times10^{-16}$	30
24	$[O(^3P)]+[O_2(X)]+[O_2(a)]\rightarrow[O(^3P)]+$	$k_{3body}=1.0\times10^{-32}$ cm^6 s^{-1}	17
25	$[O_3]+[O_2(a)]\rightarrow[O_3]+[O_2(X)]$	$k_{aO3}=2.0\times10^{-11}e^{-2840/Tg}$	29
26	$[e^-]+[O_2(a)]\rightarrow[e^-]+All$	$k_{ae}\approx f(\varepsilon_{avg})\times10^{-10}$	Scaled
27	$[O_2(v)]+[O_2(a)]\rightarrow[O_2(b)]+[O_2(X)]$	$k_v\approx4\times10^{-10}$	This Work

Table 5.2 Concentrations for relevant species determined by streamlined code.

Major Species	μ-wave (cm^{-3}) @ 2 - 7.5 Torr, and 20 (cm s^{-1})	RF (cm^{-3}) @ 4 Torr and 20 (cm s^{-1})
[O_2(X)]	$1.1\times10^{16}-5.8\times10^{16}$	4.6×10^{16}
[O_2(a)]	$1.6\times10^{15}-7.5\times10^{14}$	5.4×10^{15}
[O(^{3}P)]	$1.3\times10^{16}-3.1\times10^{15}$	1.8×10^{15}
[O_3]	1×10^{12}	1×10^{12}
[e^-]	$2.4\times10^{12}-2.1\times10^{11}$	1.2×10^{11}
[O_2(ν)]	2×10^{14}	4.6×10^{13}

Table 5.3 Destruction rates for relevant reactions determined by streamlined code.

Reaction Number	Collision Partner	Expected Γ_a s^{-1} RF	Expected Γ_a s^{-1} μ-wave
22	O_2(X)	0.1	0.1
23	O-atoms	0.16 – 0. 54	1.6 – 2.6
24	O(^{3}P) + O_2(X)	1.6 - 5.4	16 - 26
25	O_3	~3	~30
26	e^-	0.7 - 2	4 - 25
27	O_2(v)	100 - 700	1000 - 9000

The experimental data argue for a quenching term that has a value of $\sim 6\times10^{3}$ s^{-1} for μ-wave conditions and a value of $\sim 3\times10^{2}$ s^{-1} for RF conditions. The difference between the RF and μ-wave cases involves different gas temperatures, T_g; electron temperatures, T_e; and the expected concentration of the quenching species. The expected values of quenching rates for the reactions in Table 5.1 are reported for both μ-wave and RF conditions in Table 5.2.

Table 5.1 includes approximate values for reactions 22-27, which all destroy the $\left[O_2(a)\right]$ state. The values shown in Table 5.2 are approximated for a typical 4 Torr discharge, where the gas temperature is 1,000 K, flow velocity is 20 cm/s, and the flow tube diameter is 1 cm. From Table 5.1, reaction rates 22-26 are too slow by at least an order of magnitude to explain the observed yields of $O_2(a)$. A more in-depth discussion of each reaction follows.

5.1.1 $O_2(X)$ Collisionally Quenching $O_2(a, {}^1\Delta)$

The collision partner with the highest concentration is ground state oxygen. If collision relaxation of $O_2(a)$ with $O_2(X)$ (reaction 22) is the dominant quenching mechanism of the $O_2(a)$ concentration, then the decay rate would have the form:

$$\Gamma_a = k_{O_2x}\left[O_2(X)\right] \tag{5.1}$$

The reaction rate k_{O_2x}, shown in Table 4.1 and quoted from Atkinson,[29] has a value of 3×10^{-18} cm^3 s^{-1} or less for all gas temperatures. As shown in Table 4.2, combining this with the average value for $[O_2(X)]$, approximately 10^{17} cm^{-3}, it is calculated that the value of Γ_a for this reaction would be approximately 0.1 s^{-1}. This value is much too small to explain the large amount of quenching observed in this study. Furthermore, the amount of $O_2(X)$ in the gas flow does not change significantly from the RF case to the μ-wave case. Therefore, this reaction does not explain the difference in the decay rate, Γ_a, between the RF and μ-wave discharges. Ground state molecular oxygen does not strongly quench the $O_2(a)$ state and does not exhibit the needed behavior as a function of discharge frequency. Because there is not a significant change in the destruction rate between the μ-wave and RF case using this mechanism, this reaction cannot be the dominant reaction limiting the concentration of $O_2(a)$ within electric discharges.

5.1.2 O-atom Collisionally Quenching $O_2(a, {}^1\Delta)$

The possibility that O-atoms are responsible for limiting $O_2(a)$ is feasible for a number of reasons. O-atoms are not created in a conventional COIL SOG; they are resistant to recombination; they are predicted to make up at least 10% of the gas flow in the discharge;[7, 17] and they look to have the correct functional dependence on the electron and ground state concentrations, as shown in Equation 4.31:

$$\left[O({}^3P)\right] = \frac{k_{O+}[e^-]\ \left[O_2(X)\right]}{k_{Wall}} \tag{5.2}$$

The rate for O-atom collisionally quenching the $O_2(a)$ state (reaction 23) is reported in Table 4.1 and is:

$$k_{aO} = 2.0 \times 10^{-16}\ \text{cm}^3\ \text{s}^{-1} \tag{5.3}$$

In order for this reaction to obtain a value of Γ_a of approximately 1,000 s^{-1}, the concentration of O-atoms must be on the order of 10^{20} cm^{-3}. Because there are only 10^{17}

cm^{-3} oxygen molecules in the gas flow, this explanation is impossible at the pressures studied in this work. Although O-atoms meet many of the criteria for being the dominant quenching mechanism within the electric discharges, the rate of the reaction is not fast enough to describe the data.

5.1.3 O_3 Collisionally Destroying $O_2(a\ ^1\Delta)$

Ozone is a very reactive species that is generated within the discharge and is not present in conventional COIL systems. Because ozone reacts so quickly, small amounts of it within the gas flow may have significant effects on the makeup of the gas. It is also this reactivity that limits ozone to making up approximately 0.001% of the gas flow. The mechanisms likely to dominate the production of ozone within the discharge are shown below:

$$\begin{aligned}
&[O]+[O_2(X)]+[M]\xrightarrow{k_{O3+}}[O_3]+[M] && k_{O3+}=2.0\times10^{-35}\ \text{cm}^6\ \text{s}^{-1}\\
&[O^-]+[O_2(a)]\xrightarrow{k_{O-a}}[O_3]+[e^-] && k_{O-a}=3.0\times10^{-10}\ \text{cm}^3\ \text{s}^{-1}\\
&[O_3]+[O_2(a)]\xrightarrow{k_{O3a}}2[O_2(X)]+O && k_{O3a}=3.0\times10^{-12}\ \text{cm}^3\ \text{s}^{-1}
\end{aligned}\tag{5.4}$$

Ozone is offered as the mechanism responsible for the limitation of $\left[O_2(a)\right]$ within the electric discharge studied by Stafford.[7] According to Stafford:

$$\begin{aligned}
&[O_3]\approx10^{12}\ \text{cm}^{-3}\\
&[O_3]k_{O3a}\approx10^{12}\left(3.0\times10^{-12}\right)=3.0s^{-1}
\end{aligned}\tag{5.5}$$

Using the ozone concentrations reported by Stafford[7] of 10^{12} cm^{-3} and then using the rate of k_{O3a} provided by Stafford,[7] the value of Γ_a would be approximately 3 s^{-1}. By using the Stafford model, it has been predicted that up to 30% yields are achievable using an

RF discharge.[7] However, the measured yields reported by Rakimova,[17] as well as this work, are less than 10% yields. It would appear that the Stafford model does not compare well to measured yields. Therefore, it is likely that another mechanism besides quenching by ozone is responsible for limiting Y_a in the experimental apparatus.

The production pathway of ozone is rich. So, making a definitive statement concerning the pressure dependence of ozone is very complicated. Therefore, eliminating ozone as a possible candidate for the quenching mechanism based on pressure dependence, changes with flow velocity, or dependence on gas temperature is not possible.

The production term of ozone is dependent on O-atom concentration, so it is expected that, as electron density increases and, subsequently, the O-atom population increases, ozone population should increase. Therefore, an ozone-dependent decay term, Γ_a, is expected to scale properly as the discharge is changed from RF to μ-wave. It is unlikely that a large enough quantity of ozone is realized within the gas flow in order for it to dominate the quenching of $O_2(a)$ within the discharge.

5.1.4 O(^{1}D) as Destruction Mechanism O$_2$(a $^1\Delta$)

The $O(^1D)$ state, like ozone, is a very reactive species that does not occur in a conventional COIL system but is produced in significant quantities within an electric discharge sustained in oxygen gas. Also, like ozone, the fast reaction rates of this excited state of atomic oxygen with both the wall and other species within the discharge keep its concentration small. The role played by $O(^1D)$ is contentious within the literature.

Despite the uncertainty in the kinetics mechanism, the following discussion assesses the potential for $O(^1D)$ as a dominant $O_2(a)$ deactivation partner.

In the literature, Kushner's research groups refer to $O(^1D)$ as a source of $O_2(a)$.[79] Kushner's model does not include a reaction between $O_2(a)$ and $O(^1D)$, which quenches or pools the $O_2(a)$ state. However, the research group that includes Ionin[74] is currently using the reaction rate given below:

$$\left[O_2(a)\right]+\left[O(^1D)\right]\rightarrow\left[O_2(X)\right]+\left[O(^3P)\right],\; k_{-a1D}=1\times10^{-11}cm^{-3}s^{-1} \tag{5.6}$$

This reaction rate is quoted from the paper by Doroshenko et al.[80] However, this reaction rate is not used by Stafford,[7] Rakimova,[17] Hicks,[57] or Hill.[55] Hence, for the remainder of this analysis, it will be assumed that this reaction may be neglected.

The approximate concentration of $O(^1D)$ is calculated assuming that the source of $O(^1D)$ is direct electron impact with ground state oxygen (reaction 14) and is destroyed collisionally by O-atoms (reaction 30):

$$\left[O(^3P)\right]+\left[O(^1D)\right]\rightarrow\left[O(^3P)\right]+\left[O(^3P)\right],\; k_{O1D}=8.0\times10^{-12}cm^{-3}s^{-1} \tag{5.7}$$

Therefore, the change to the concentration of $O(^3P)$ as a function of time is described by the differential equation:

$$\frac{d\left[O(^1D)\right]}{dt}=k_{1d+}[e][O_2(X)]-k_{O1d}\left[O\left(^3P\right)\right]\left[O\left(^1D\right)\right]-k_{o21d}[O_2(X)]\left[O\left(^1D\right)\right]. \tag{5.8}$$

Assuming steady-state and values for the rates and electron concentration, from a 4 Torr gas flow at 20 cm/s, the concentration of $O(^1D)$ is approximately:

$$\left[O\left({}^{1}D\right)\right]_{SS}=\frac{k_{1d+}[e][O_2(X)]}{k_{o21d}[O_2(X)]}=\frac{k_{1d+}[e]}{k_{o21d}}=\frac{\left(7\times10^{-11}\right)\left(2.3\times10^{12}\right)}{\left(2.6\times10^{-11}\right)}=1.2\times10^{13}cm^{-3}.$$

(5.9)

The calculation of the source terms for $^1\Delta$ and $^1\Sigma$ (reactions 32 and 31) are shown below:

$$\left[O_2(X)\right]+\left[O({}^1D)\right]\rightarrow\left[O_2(a)\right]+\left[O({}^3P)\right],\ k_{a1D}=1.6\times10^{-12}e^{-67/T_g}cm^{-3}s^{-1} \quad (5.10)$$

$$\left[O_2(X)\right]+\left[O({}^1D)\right]\rightarrow\left[O_2(b)\right]+\left[O({}^3P)\right],\ k_{b1D}=2.56\times10^{-11}e^{-67/T_g}cm^{-3}s^{-1} \quad (5.11)$$

using this steady-state value for [$O({}^1D)$]. The resultant Γ_a is calculated with the reaction for $O({}^1D)$ as a source of $O_2(a)$ subtracted from the quenching reaction. So, [$O({}^1D)$]$_{ss}$ = 1.2×10^{19}, k = ($1 \text{ X } 10^{-17}$ - 1.5×10^{-18}) = 8.5×10^{-18}, which implies that Γ_a = 102.

This value for gamma is an order of magnitude that is too small. Furthermore, the functional form of the $O({}^1D)$ steady-state concentration is also linearly dependent on the electron density:

$$\left[O\left({}^{1}D\right)\right]=\frac{k_{1d+}[e][O_2(X)]}{k_{o21d}[O_2(X)]}=\frac{k_{1d+}[e]}{k_{o21d}} \quad (5.12)$$

Hence, this mechanism for gamma will linearly depend on the gas pressure. Because the product of the reaction rate and steady-state concentration are not sufficient enough to obtain a Γ_a of 1,000, and because this reaction would yield a gamma that depends on the gas pressure, $O({}^1D)$ is not the primary quenching mechanism for $O_2(a)$. It should be noted that the wall rate for relaxation of $O({}^1D)$ is approximately 1×10^5 s^{-1}. If the quenching of $O(^1D)$ is dominated by the wall and not the reaction with the ground state, then the concentration of this reactant would be independent of the background gas concentration, thereby meeting this observed criteria for the quenching mechanism of $O_2(a)$. However, the reaction rates in Equations 5.10 and 5.11 are well known and when combined with the a nominal value of the ground state concentration of ~10^{16} cm^{-3} result in a destruction rate of ~10^5 s^{-1}. A nominal wall rate is on the order of 10^3 s^{-1} which is two orders of magnitude smaller than the collisional destruction rate of $O(^1D)$. Thus the dominant destruction method of $O(^1D)$ is by collisions with ground state and therefore will be dependent upon the electron concentration as shown in Equation 5.12. Hence the destruction of $O_2(a)$ by collision with $O(^1D)$ does not fit the measured data.

5.1.5 Removing Power Loading Effects

Because of the different plasma geometries and production methods studied herein, the power loading of the plasmas varies between the different measurements. In order to remove any power loading effects from the results in Figure 5.1, Γ_a is divided by the power loading term, which is the left-hand side of Equation 4.33. At sufficiently slow flow velocities, Equation 4.33 may be written as:

$$k_L\left[e^-\right]_{ss}\left[O_2(X)\right]_{ss} \approx \frac{P_{in}}{V} \tag{5.13}$$

This expression for power loading is used in Figure 5.1 to put the decay rates determined from Stafford,[7] Rakimova,[17] and this work on the same footing. In Figure 5.1, it is observed that all the values of Γ_a appear to fall on a single line once power loading is removed from their values. Figure 5.1 also shows the expected functional forms of reactions 24, 26, and 27. A discussion of these three reactions follows.

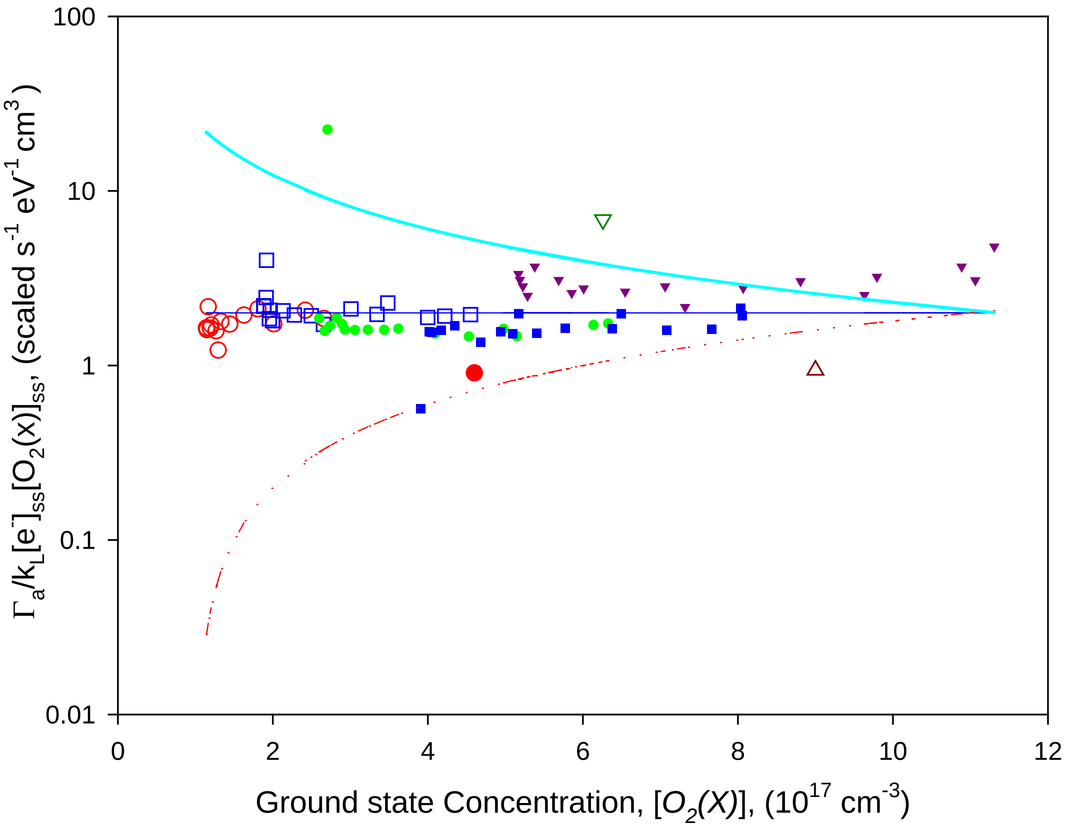

Figure 5.1 Relation of Γ_a / $[O_2(X)]$ versus $[O_2(X)]$. ○ 2 Torr, □ 3 Torr, ● 4 Torr, ■ 5 Torr, ▼ 7 Torr, ▽ current work RF 4 Torr, ● Stafford RF[7], △ Rakimova RF[17]. Expected Γ_a for — $O_2(v)$ Reaction 27, — electrons Reaction 26, and – three-body Reaction 24.

5.1.5.1 e^- as the Dominate Destruction Mechanism of $O_2(a\,^1\Delta)$

The rates of electrons reacting with the $O_2(a)$ state, such as reaction 26, are not studied exhaustively in the literature. Therefore, values for these reactions are scaled from the values of the electron interactions with the ground state.[7] In this study, the absolute value of this rate will not be important to the conclusions. The absolute value will be assumed to be of the same order of magnitude as other reaction rates within the plasma, and its trend as a function of pressure, gas flow velocity, and E-field frequency will be used as determining factors for the conclusion of this paper.

As seen in Figure 5.1, the electron-dependent, power loading corrected, pseudo-first order decay term, shown in gray, decreases as the ground state concentration is increased. This does not match the measured results, which are not dependent on the ground state concentration. Therefore, this quenching mechanism may be eliminated from consideration based on the trend of this line, as well as having too small of an absolute value, as reported in Table 5.2.

5.1.5.2 Three-Body Recombination

The three-body reaction is included in the results of Rakimova[17] and is highly defended as the current solution to resolving the difference between current models and measurements.[74] The rate of this reaction is not well understood and has been determined on the basis of matching simulated $\left[O_2(a)\right]$ to experimentally measured $\left[O_2(a)\right]$. The reported value for the three-body reaction is on the order of 10^{-32} cm^6 s^{-1}. Using this value for the three-body reaction at a gas pressure of 4 Torr, and assuming that O-atoms make up approximately 10% of the gas flow, the following value of Γ_a is obtained:

$$\begin{aligned} &[O]+[O_2(a)]+[O_2(X)]\xrightarrow{k_{3Body}}[O\ ]+2[O_2(X)] \\ &k_{3Body}=3.0\times10^{-32}\ \text{cm}^6\ \text{s}^{-1} \end{aligned} \tag{5.14}$$

$$\begin{aligned}\Gamma_{3Body} &= k_{3Body}[O][O_2(X)]\ \text{s}^{-1} \\ \Gamma_{3Body} &\approx \left(3.0\times10^{-32}\right)\ \left(1.0\times10^{16}\right)\ \left(1.0\times10^{17}\right) \approx 10\ \text{s}^{-1}\end{aligned} \tag{5.15}$$

The work reported by Rakimova is based on the results of an RF discharge.[17] Therefore, the expected value of gamma is approximately 100 s^{-1}. The rate of the reaction, shown in Equation 5.15, is dependent on the O-atom concentration. As shown in Equation 4.31, O-atoms scale directly with electron density; therefore, this reaction will scale by an order of magnitude when changing from μ-wave to RF discharges. The scaling by an order of magnitude from μ-wave to RF discharges makes the three-body reaction rate a prime candidate for explaining the observed behavior of Y_a. Not only is the reaction rate too small; this mechanism is not independent of the ground state concentration, as shown in Figure 5.1. The power loading corrected value of Γ_a for the three-body reaction is shown as a dashed black line in Figure 5.1. This term predicts correct values at higher pressures, but it diverges from the required values at lower pressures. Therefore, another mechanism is sought after to describe the measured data.

5.1.5.3 Vibrationally Excited Oxygen

Vibrationally excited molecular oxygen is produced within electric discharges by direct electron impact, as seen in Table 2.1, reactions 3-9:

$$[e^-]+[O_2(X)]\xrightarrow{k_v}[e^-]+[O_2(v)] \tag{5.16}$$

The sum of reaction rates 3-9, as determined for a 4 Torr microwave discharge, using the BolSig+ code, is:

$$k_v \approx 4\times10^{-10}cm^3s^{-1} \tag{5.17}$$

The vibrationally excited states of oxygen are quenched by both atomic oxygen and ground state oxygen at the rate of 1.4 x 10^{-14} cm^3 s^{-1}, as reported by Atkinson.[29] The rate of destruction of vibrationally excited oxygen via these methods is approximately:

$$k_{v-} \times \left[O_2(X)\right] = \left(1.4 \times 10^{-14}\right)\left(1 \times 10^{17}\right) = \left(2.8 \times 10^{3}\right) s^{-1} \tag{5.18}$$

The reaction of vibrationally excited oxygen at the wall is fast. The wall rate is calculated using the same form as discussed in Section 4.6.1, Equation 4.31:

$$k_{Wall} = \frac{v_{th}\gamma_0}{2r} \tag{5.19}$$

For vibrationally excited oxygen, $\gamma_0 = 0.2$, as reported by Stafford.[7] Therefore, the expected rate of $O_2(v)$ destruction at the wall is 24,000 s^{-1}. Destruction at the wall is larger than destruction by O-atoms and molecular oxygen by an order of magnitude.

Using the production rate by direct electron impact and destruction at the wall, the expected steady-state value of vibrationally excited molecular oxygen is:

$$\left[O_2(v)\right]_{ss} = \frac{k_{v1-}\left[e^-\right]_{ss}\left[O_2(X)\right]_{ss}}{k_{Wall}} \tag{5.20}$$

Using average values for a microwave discharge at 4 Torr,

$$\left[O_2(v)\right]_{ss} = \frac{\left(4 \times 10^{-10}\right)\left(3 \times 10^{11}\right)\left(4 \times 10^{16}\right)}{2.4 \times 10^{4}} = 2 \times 10^{14} cm^{-3} \tag{5.21}$$

If Γ_a is determined by reaction 27, then Γ_a would have the form:

$$\Gamma_a = k_{va}\left[O_2(v)\right] \tag{5.22}$$

Because $[O_2(v)]_{ss}$ is expected to have the value of 2 x 10^{14} cm^{-3}, for Γ_a to have a value of 6,000 s^{-1} for a microwave discharge, the value of k_{va} must be 3 x 10^{-11} cm^3 s^{-1}. The required value of k_{va} is within the limits of the gas kinetic rate. However, this reaction rate is five orders of magnitude faster than quenching by atomic oxygen (reaction 46) and, therefore, not likely. But, if this quenching rate was believable, then the concentration of vibrationally excited oxygen does fit the other required conditions mentioned in this study.

If it is assumed that all excited species within the discharge eventually relax back to the ground state and that, while relaxing to the ground state, these species populate a vibrationally excited state, then there could be significant secondary sources of $O_2(v)$. If it could be presumed that the $[O_2(v)]_{ss}$ could obtain a value approaching 10% of the gas flow, then the reaction rate would be sufficiently large enough to explain the values of Γ_a at 5 x 10^{-12} cm^3 s^{-1}. While this rate is still faster than most reactions between two neutrally charged species, it is on the same order of magnitude as ozone reactions.

Vibrationally excited oxygen is a plausible candidate for quenching the $O_2(a)$ in the EOIL system. The $O_2(v)$ state is well populated in the EOIL SOG and does not exist in the COIL SOG. It trends correctly with the change in the SCCM in the measured data. Most importantly, because of the dependence on the electron concentration, as shown in Equation 4.42, this reaction explains the large difference in gamma between the RF and μ-wave E-fields.

5.2 Dominant Destruction Pathway

The concentration of singlet delta oxygen in microwave discharges of pure oxygen reaches a steady value within a 1 ms discharge residence time, independent of discharge pressure. Also, the corresponding yields decrease inversely with pressure. A steady-state analysis of the kinetics is adequate to explain the observations, assuming only electron excitation of $O_2(a)$, the inverse super-elastic process, and an unspecified third channel for $O_2(a)$ destruction. The pseudo-first order decay rate for the unspecified process is about 6,000 s^{-1} in the microwave discharge, independent of pressure and flow rate. The same rate in the RF discharge is much slower, 300 to 500 s^{-1}. Modeled electron number density is also considerably less in the RF discharge. As a whole, the results suggest a $O_2(a)$ removal process that is: (1) rapid compared to the super-elastic rate; (2) induced by a species generated by electron kinetics; and (3) a second order reaction.

A steady-state analysis has been presented of many species potentially responsible for the destruction of $O_2(a)$ within the discharge. It has been argued that the collision partner must be dependent on the product of the electron and oxygen ground state concentrations. A brief look at the steady-state concentrations of likely collision partners is shown below:

$$\left[O\left({}^1D\right)\right]=\frac{k_{1d+}[e^-][O_2(X)]}{k_{o21d}[O_2(X)]}=\frac{k_{1d+}[e]}{k_{o21d}}$$

$$\left[O(^3P)\right] = \frac{k_{O+}[e^-]\ \left[O_2(X)\right]}{k_{Wall}}$$

$$\left[O_2(v)\right]_{ss} = \frac{k_{v1-}\left[e^-\right]_{ss}\left[O_2(X)\right]_{ss}}{k_{Wall}}$$

All of the steady-state concentrations are directly related to the electron density and, therefore, are expected to exhibit the order of magnitude change as the E-field frequency is changed. However, many collision partners, such as $O(^1D)$, are not directly dependent upon the product, $\left[e^-\right]\times\left[O_2(X)\right]$, and, therefore, would not exhibit the flat response as a function of gas pressure and flow rate. In these steady-state representations, it may be seen that both the $O(^3P)$ and $O_2(v)$ states have the correct dependence.

Even though O-atoms have the correct behavior versus E-field, pressure, and flow velocity, the expected value of Γ_a is not sufficient enough to explain the behavior of $O_2(a)$. As seen in Table 5.3, the expected Γ_a for the O-atoms is two orders of magnitude too small. The reaction rate between O and $O_2(a)$ is well known; so, it is highly unlikely that quenching of $O_2(a)$ by O-atoms is responsible for limiting the population within the discharge. However, other excited species that are dependent on O-atoms but have much faster reaction rates with $O_2(a)$ could maintain the correct independence of pressure and flow rate and provide plausible reaction pathways for the destruction of $O_2(a)$.

The reaction rates governing the behavior of $O_2(v)$ are not as well understood as those for O-atoms. The source terms for $O_2(v)$ within the discharge are not well determined. Direct electron impact with $O_2(X)$ creating $O_2(v)$ is included within the BolSig+ package; however, there are many different pathways in which $O_2(v)$ could be created within the discharge. O-atoms recombining at the wall of the flow tube could return to the gas flow in the form of $O_2(v)$. Any excited molecular species, $O_2(b)$ or $O_2(A)$, that is collisionally quenched within the discharge could also form $O_2(v)$ while losing its energy and relaxing back to the ground state. O_3 and higher energy atomic oxygen species could also contribute. If these pathways contribute significantly to the concentration of $O_2(v)$ within the discharge, then the proposed reaction rate would not need to be so large, making this destruction mechanism more palatable.

VI Conclusions

The directed energy community has been pursuing a laser-based weapon system since the lasing concept was first demonstrated. After the Airborne Laser Lab (ALL) successfully destroyed multiple airborne targets in 1983, the concept of an ABL weapon appeared to be on the horizon. The current ABL system employs a COIL that suffers from an extensive logistics trail. Using an EOIL eliminates the logistical limitations. Existing EOIL systems have achieved laser powers of 102 W, but scaling to kilowatts seems to be limited by the pressure dependence of the $O_2(a)$ yield. Determining the chemical kinetics responsible for limiting the yield is paramount to finding a means to increase the yield as a function of pressure or determine a different means to scale laser power.

A systematic study of microwave discharges has been performed through the pressure range of 2 to 10 Torr in pure oxygen flows. Gas temperatures of 300 to 1,200 K have been determined to a higher resolution than previously reported in the literature, subsequently increasing the accuracy of the reported concentrations, by 10%. A theoretical description of the gas temperature allows the determination of the fraction of discharge energy coupled into gas heating (15 to 30%). The simulation of $O_2(a)$ molecular emissions and O-atom species, which emit in the same spectral region, allows concentration measurements to be made directly inside the discharge region. From the measured changes in $O_2(a)$ concentrations, a pseudo-first order decay rate has been determined. The change in the decay rate as a function of gas flow velocity, gas pressure, and electric field frequency has determined that a second order term directly related to electron concentration is responsible for quenching the $O_2(a)$ state. Many reaction pathways are considered; however, no clear quenching mechanism sufficiently describes the observations.

The gas temperature measurements reported in this work have been extracted from the rotational energy distribution of the excited $O_2(b)$ state. The resolution of the $O_2(b)$ spectral data reported in this study is 0.01 nm, while the most precise resolution reported in literature is 0.04 nm. Higher resolution spectra allow the determination of the gas temperature to a higher degree of precision. Typical errors in reported gas temperatures for this study are 5% or less, whereas errors in gas temperature reported in the literature are typically 10% or greater. Because the gas temperature influences the intensity of the emissions from all of the measured species, higher precision temperature determination results in higher precision density measurements. The high-resolution gas temperature measurements performed in this study improve the quality of the reported data throughout this work by approximately 10%.

This study also includes a theoretical description of the gas heating used to extract the fraction of discharge power coupled into gas heating. Using the presented method to determine fractional power coupled to heating was applied not only to the measurements made by this group but also those reported by UIUC.[5] The importance of these results is related to the efficiency of a proposed weapon system using an electrically driven SOG. The 17% of discharge power that is coupled into gas heating will not be available to pumping energy useful to the laser weapon system. From the calculations in Appendix

B, in a typical microwave discharge at 2 Torr of oxygen, 66% of the power is removed from the discharge by atomic oxygen, and only 1% of the power is removed by the $O_2(a)$ excited state of oxygen. This effect may ultimately limit the usefulness of an EOIL system for weapons applications.

Measured emissions intensity of $O_2(a)$ are also affected by variations in the gas temperature. An increase in the gas temperature decreases the emitting species concentration. If the effect of gas temperature is not included in the analysis of these emissions, then one cannot determine whether the change in concentration was caused by chemical kinetics.

$O_2(a)$ emission intensity measurements made within the discharge region have been reported. Four atomic species present in the electric discharges emit in the same spectral region, from 1,250 to 1,300 nm, as the $O_2(a)$ state. These atomic emissions are from high-energy or ionic O-atoms, which are not observed downstream of the discharge but have sufficient concentrations within the discharge region. By using a computer model, the intensity contributions of these emissions are separated from the reported $O_2(a)$ emission intensities. Using the computer model allows $O_2(a)$ intensity measurements made directly inside the discharge region to reflect the concentration of the $O_2(a)$ state without introducing errors that result from changes in the atomic oxygen. Other studies in the literature report yields above 30% but laser powers of μ-watts. This may be the result of extracting $O_2(a)$ concentrations from spectral emissions, including emissions from O-atoms. Identification of these emissions within the discharge has not been previously reported.

The interpretation of the measured $O_2(a)$ yield, using a streamlined, nearly analytic model, cast new light on the determination of the kinetics within the electric discharge. The quenching rate at μ-wave frequency field oscillations ranges from Γ_a = 4,000 to 9,000 s^{-1}, while the values range from Γ_a = 400 to 600 s^{-1} for RF fields. The only rate that changes significantly between the two different field oscillation frequencies is the rate of ionization. This result leads directly to the determination that the $O_2(a)$ quenching mechanism must be related to the ionization rate. It is a small step from this result to the assertion that electron number density must be important to the quenching term.

Quenching of the $O_2(a)$ state by direct impact with electrons does not explain the acquired data. As shown in Table 4.2, the expected rate of quenching the $O_2(a)$ state by collisions with electrons is two orders of magnitude smaller then required to explain the data. Also, the quenching rate is invariant as the flow velocity changes, whereas electron density changes linearly with gas flow velocity. Therefore, direct collisions with $O_2(a)$ and electrons is not responsible for destroying the $O_2(a)$. The product of electron number density and ground state oxygen concentration is constant as a function of the gas flow, as determined by the power balance equation. There are two reactions that are dependent on the product of electron number density and the ground state concentration, which will limit yield in the correct manner to explain the measured results.

The two reactions proposed to explain the pressure dependence of the $O_2(a)$ quenching are dependent on the electron density in different ways. The three-body reaction reported by Rakimova is appropriate if it is assumed that the electron density increases as the pressure of the oxygen is increased. If the electron density follows the trend in average electron energy and decreases with pressure, then the $O_2(v)$ quenching mechanism proposed in this work is the remaining explanation to the limit in $O_2(a)$ yield. This new quenching mechanism may present the community with the new focus in which scaling of an EOIL system to powers required for weapons applications is realized.

This work points to the $O_2(v)$ as a possible quenching mechanism of $O_2(a)$. In order to determine the validity of this mechanism, the concentration of $O_2(v)$ within the gas flow should be verified. Optical detection of $O_2(v)$ is complicated, because the energy separation of the excited states does not produce photons that are easily distinguishable from thermal emissions. The primary quenching rate of $O_2(v)$ is the wall rate, as discussed in Section 4.9.4.3. Therefore, the term, Γ_a, should be dependent on changes to the surface area of the discharge region.

In conclusion, a large step was made towards a field-ready system in switching to an oxygen-iodine laser. However, in choosing the chemistry based laser system, a logistics issue was introduced. Using an EOIL on the airframe may be the solution if scaling to kW laser powers is realized. In this work, it is argued that power scaling is a complicated endeavor that involves complicated chemical kinetics involving a second order quenching of the $O_2(a)$ state used as the energy reservoir for oxygen-iodine laser systems.

Appendix A

Section A.1 Determination of Laminar Flow

The oxygen gas flow is assumed to be a laminar flow throughout the calculations in the document. This assumption is based on the calculation of the Reynolds number of the experimental apparatus. Reynolds numbers of less then 500 are generally considered to be of a laminar type.[40] The Reynolds number is defined as:

$$\mathrm{Re} = (\rho v_g D) \big/ \mu \tag{A.1}$$

where ρ is the density of the gas; v_g is the velocity of the gas flow; D is the diameter of the flow tube; and μ is the dynamic viscosity of the fluid. The dynamic viscosity of the fluid is a function of the gas temperature, T_g, as shown below:

$$\mu = \mu_0 \left(\frac{T_0 + C_0}{T_g + C_0} \right) \left(\frac{T_g}{T_0} \right)^{3/2} \tag{A.2}$$

where μ_0 is the reference viscosity at the reference temperature T_0; T_g is the temperature of the gas flow; and C_0 is Sutherland's constant for the gaseous material in question.

For the specific case of oxygen flowing in a 1 cm diameter flow tube, with a gas temperature of 1,000 K (as used in this study), the value of the Reynolds number is:

$$\mathrm{Re} = 0.0082 \tag{A.3}$$

where the density of oxygen, ρ, is 0.3899 kg/m^3,[40] and velocity is 100 m/s. The value of the dynamic viscosity is calculated using values of: reference viscosity, μ_0, is 20.18 N s / m^2;[40] reference temperature, T_0, is 292.25 K; Sutherland's constant, C_0, is 127 K[40]; and the gas temperature, T_g, is 1,000 K. This yields a value for the dynamic viscosity of 47.5 N s / m^2. The value of the Reynolds number is well below 500, where a gas flow transitions from a laminar. Therefore, it is a good assumption that this flow is laminar.

Section A.2 Thermodynamic Evaluation of the System

The derivation of the energy equation shown in Section 2.5 will be discussed in this section. The expression will be derived from the first and second laws of thermodynamics. The form of the solution is similar to the energy balance equations found in Stafford and Kushner,[7] Rakimova,[17] and Kays and Crawford.[40]

Starting with the first law of thermodynamics, assuming that work performed by the system is dW, defined as *PdV*:

$$dQ = dE + PdV \qquad \text{(A.4)}$$

where *Q* is the heat added to the system; *E* is the total energy of the system; *P* is the pressure in the system; and *V* is the volume of the system. This law states that the heat either removed from or deposited into the system must go to mechanical work, expanding the volume of a container, or be deposited in the internal energy of the system. The work done by the expansion of the gas is obtained by assuming that the change in the volume may be calculated using the equation:

$$\mathrm{V = A\ z} \qquad \text{(A.5)}$$

where the change in the value of z is determined by the change in the velocity of the gas flow, and, therefore, the expression is:

$$\mathrm{z = t_0\ v_g} \qquad \text{(A.6)}$$

where $A = \pi r^2$ is the area of the flow tube; t_0 is the time it takes the gas to travel an arbitrary distance (in this case, the length of the discharge assuming constant flow velocity of 100 m/s); and v_g is the velocity of the gas. Combining equations A.5 and A.6 with the ideal gas law and mass conservation law, the change in energy and work is calculated, as the temperature changes from 300 to 1,200 K. The volume change, dV, is 2.4×10^{-6} m^3, and the pressure is equal to 533 N/m^2 at 4 Torr, which results in a change of 1.2×10^{-3} J or 1.5% of the total power. For the remainder of the calculation, this small amount of power loss will be ignored.

So, the first law of thermodynamics is reduced to the expression:

$$dQ = dE\ . \qquad \text{(A.7)}$$

If it is assumed that the volume is filled with pure oxygen, then the total energy of the gas flow takes the form of either kinetic energy of the gas or into the internal energy of the oxygen molecule. Therefore, the first law may be written as:

$$dQ = dE = N\left(C_p dT_g + \frac{1}{2}m\left(dv\right)^2\right) \qquad \text{(A.8)}$$

If the gas within the discharge is assumed to be of uniform temperature, then a simple convective heat transfer coefficient is defined as:

$$\dot{q}_0'' = -h_T(T_g - T_0) \qquad \text{(A.9)}$$

where $\dot{q}_0''$ is the heat flux in (J s^{-1} m^{-2}); h_T is the heat transfer coefficient in joules per second per meter squared per Kelvin; T_0 is the temperature of the wall; and T_g is the temperature of the gas. The wall of the gas flow tube maintains a temperature just above room temperature of approximately 400 K. The energy lost from the gas to the flow tube wall occurs over the surface area of the discharge, *S*. This is also known as Newton's Law of Cooling. The incremental change in the internal energy of the gas, *dE*, is:

$$dE = dU = fP_{in} - Sh_T(T_g - T_0) \qquad \text{(A.10)}$$

where $f\,P_{in}$ is the fractional power coupled into heat. From Equation A.7, the incremental change in the energy of the system must equal a change in the total heat of the system, *dQ*, and the following relationship may be written:

$$N\left(C_p dT_g + \frac{1}{2}m\left(dv\right)^2\right) = fP_{in} - Sh_T(T_g - T_0) \qquad \text{(A.11)}$$

This relationship shows that a fraction of the power coupled into the gas which is thermally conducted to the walls of the flow tube. The remaining energy is coupled into the excited molecular states of oxygen, as well as an overall change in the flow velocity of the gas.

The mass of molecular oxygen is 32 amu. The change in the gas velocity due to measured changes in the gas temperature is determined to be 10 meters per second or less. Using this result for the change in velocity, the kinetic energy associated with velocity of the gas is:

$$N\frac{1}{2}m\left(dv\right)^2 \approx 0.03J \qquad \text{(A.12)}$$

Therefore, the contribution of change in kinetic energy to the internal energy of the system will be ignored, and Equation A.11 becomes:

$$NC_p dT_g = fP_{in} - Sh_T(T_g - T_0) \qquad \text{(A.13)}$$

This is the form of the energy conservation equation, which is used in Section 2.5.

Appendix B

The theoretical treatment of the plasma within this study dictates that the power coupled from the electric field into the plasma is divided among elastic and inelastic collisions of the electrons with ground state oxygen. After steady-state is achieved within the discharge, taking about 1 ms, 17% of the power has been coupled into heating the gas in the discharge; 4% has been coupled into the ionization of the gas; 17.4% has been coupled into excited species of oxygen; and the remainder has been lost to the walls and dissipated by forced convective cooling into the surrounding air. Determination of these percentages follows.

The percentage of power coupled into excited species is determined by the concentrations calculated from the measured concentrations of O-atoms, using actinometry, and $O_2(a)$, by scaling to the Rakimova data, and in combination with the simulated results presented in this work.

The amount of power convectively removed from the discharge region, P_M, is calculated as:

$$P_M = Av\Delta E\left[M\right] \tag{B.1}$$

where A is the cross-sectional area of the flow tube; v is the velocity of the flowing gas; ΔE is the energy used to form the excited state; and $[M]$ is the concentration of the excited species, M, at steady-state, in the gas flow.

Nominal values for the excited species are taken from Table 5.2: Oxygen atoms 5% = $1.3\times10^{16}\,cm^{-3}$, $O_2(a)$ 2% = $1.6\times10^{15}\,cm^{-3}$. The energy required to form the excited state, $O_2(a)$, is 1 eV. Atomic oxygen is primarily produced within the discharge via two pathways (reactions 13 and 14):

$$\begin{aligned} &e^- + O_2(X) \xrightarrow{k_{OP+}} O(^3P) + O(^3P) + e^- \\ &e^- + O_2(X) \xrightarrow{k_{OD+}} O(^3P) + O(^1D) + e^- \end{aligned} \tag{B.2}$$

Reaction 13 results in the production of two oxygen atoms in the ground state and requires 6 eV. The result of Reaction 14 is one O-atom in the ground state and one O-atom in the ^{1}D excited state which requires 8.4 eV. At the electron temperature in which this study occurs (approximately 3 eV), the reaction rate coefficients of these two reaction pathways are about the same. Therefore, the energy required to generate a pair of oxygen atoms from an oxygen molecule in the ground state is an average of these two energy pathways and is equal to 7.2 eV. For energy conservation to hold when two oxygen atoms recombine at the wall of the flow tube, forming a ground state oxygen molecule, the energy deposited to the wall will be 7.2 eV. Also, the amount of energy carried out of the discharge region by atomic oxygen is also 7.2 eV per pair.

Using Equation B.1 and the transitional energies previously discussed, the amount of energy removed from the discharge by energetic species in the gas flow will be approximated. If v = 2,000 cm/s, $A = \pi r^2 = \pi\left(0.5\right) = 0.78\ cm^2$, and $Vol = 2.4\ cm^3$, then the convective power loss by atomic oxygen is:

$$\begin{aligned} &Av\Delta E\left[O\right] = \left[0.78\ cm^2\right]\left[2,000\ cm/s\right]\left[1.3\times10^{16}\ cm^{-3}\right]3.6\ eV \\ &P_O = 12 \text{ W} \end{aligned} \tag{B.3}$$

and by $O_2(a)$ is approximately:

$$\begin{aligned} Av\Delta E\left[O_2\left(a\right)\right] &= \left[0.78\ cm^2\right]\left[2{,}000\ cm/s\right]\left[1.6\times10^{15}\ cm^{-3}\right]1.0\ eV \\ P_{O2a} &= 1\ \text{W} \end{aligned} \tag{B.4}$$

Energy is also deposited collisionally at the walls by excited species. The majority of the energy deposited at the wall by excited species is carried by atomic oxygen. The thermal transfer due to O-atoms recombining at the surface of the wall may be determined using the wall rate in reaction 19 and the approximation of the concentration of O-atoms. Therefore, using the wall rate, the power transferred to the flow tube walls by this reaction may be calculated as:

$$\begin{aligned} k_{Wall}\left[O\right]Vol\Delta E &= \left[1600\ s^{-1}\right]\left[1.3\times10^{16}\ cm^{-3}\right]\left[2.4\ cm^3\right]3.6\ eV \\ P_{OW} &= 43\ \text{W} \end{aligned} \tag{B.5}$$

Where *Vol* is the volume of the discharge region. The sum of the power being swept out of the discharge region in the form of the excited species, being collisionally deposited by O-atoms at the walls, and the 17% via heat transfers, accounts for 70 W. 85 W are being coupled into the discharge from the electric field. Therefore, all of the power is not accounted for. However, all of the concentrations within this study are measured by methods that include at least a 20% error. By adding 20% to the concentrations of $O_2(a)$ and O-atoms, the dissipated power becomes 73 W. Furthermore, there are many excited species not accounted for in this power analysis, including the $O_2(A)$ state created by reaction 12 and the vibrationally excited species; so, it is not surprising that the totality of the deposited power is not accounted for.

Bibliography

(1) Missile defense agency website, http://www.mda.mil/system/altb.html.

(2) Bernard and Pchelkin, *Measurement of $O_2(^1\Delta)$ content in the gaseous effluents of a chemical generator,* **Rev. Sci. Instruments, 49**, 794, (1978).

(3) Carroll, D.L., Verdeyen, J.T., King, D.M., Zimmerman, J.W., Laystrom, J.K., Woodard, B.S., Benavides, G.F., Richardson, N.R., Kittell, K.W., and Solomon, W.C., *Studies CW Laser Oscillation on the 1315-nm Transition of Atomic Iodine Pumped by $O_2(a^1\Delta)$ Produced in an Electric Discharge*, **IEEE Journal of Quantum Electronics**, **41**, 10, (2005).

(4) Zimmerman, J.W., Woodar, B.S., Benavides, G.F., Carroll, D.L., Verdeyen, J.T., Palla, A.D., and Solomon, W.C., *Gain and continuous-wave laser power enhancement with a discharge electric oxygen-iodine laser,* **Applied Physics Letters, 92**, 241115, (2008).

(5) Carroll, D.L., Verdeyen, J.T., King, D.M., Zimmerman, J.W., Laystrom, J.K., Woodard, B.S., Richardson, N.R., Kittell, K.W., Kushner, M.J., and Solomon, W.C., *Measurement of positive gain on the 1315 nm transition of atomic iodine pumped by $O_2(a^1\Delta)$ produced in an electric discharge*, **Applied Physics Letters**, **85**, No. 8, 1320-1322 (2004).

(6) Carroll, D.L. , Benavides, G.F., Zimmerman, J.W., Woodard, B.S., Palla, A.D., Verdeyen, J.T., and Solomon, W.C., *Systematic development of the electric discharge oxygen-iodine laser,* **Proc. of SPIE, 7131**, (2010).

(7) Stafford, D. Shane, and Kushner, Mark J., *$O_2(^1\Delta)$ production in He/O_2 mixtures in flowing low pressure plasmas*, **Journal of Applied Physics, Vol. 96**, No. 5, pp. 2451-2465, (2004).

(8) Carrol, David L., and Solomon, Wayne, *ElectriCOIL: An Advanced Chemical Iodine Laser Concept,* Proceedings of the XIII International Symposium on Gas Flow and Chemical Lasers and High Power Laser Conference, Florence, Italy, 18-22 September, **The Int. Soc. For Opt. Eng., Vol. 4184**, (2000).

(9) Fujii, Hiroo, Itami, Shin…Schmiedberger, Josef, *Hybrid oxygen iodine laser with a discharge singlet oxygen generator,* **Proceedings of SPIE, Vol. 4065**, (2000).

(10) Hicks, A., Norberg, S., Shawcross, P., Lempert, W.R., Rich, J.W., and Adamovich, I.V., *Singlet oxygen generation in a high pressure non-self-sustained electric discharge*, **Journal of Physics D: Applied Physics, 38**, p. 3812, (2005).

(11) Hicks, A., Bruzzese, J., Shawcross, P., Lempert, W.R., Rich, J.W., and Adamovich, I.V., *Effect of Nitric Oxide on gain and output power of a non-self-sustained electric discharge pumped oxygen-iodine laser,* **38th AIAA Plasmadynamics and Lasers Conference,** 4236, (2007).

(12) Hicks, A., Utkin, Yu G., Frederickson, K., Lempert, W.R., Rich, J.W., and Adamovich, I.V., *Effect of Nitric Oxide on gain and output power of a non-self-sustained electric discharge pumped oxygen-iodine laser,* **45th AIAA Aerospace Sciences Meeting and Exhibit**, 1191, (2007).

(13) Schmiedberger, J., Hirahara, S., Ichinohe, Y., Suzuki, M., Masuda, W., Kihara, Y., Yoshitani, E., and Fujii, H., *RF Plasma jet generator of singlet delta oxygen for oxygen iodine laser,* **SPIE 4184**, (2001).

(14) Schmiedberger, J., Takashi, S., and Fujii, H., *Improved RF Plasma jet generator of singlet delta oxygen,* **SPIE 3092.**

(15) Touzeau, M., Vialle, M., Zellagui, A., Goussett, G., Lefebvre, M., and Pealat, M., *Spectroscopic Temperature Measurements in Oxygen Discharge,* **J. Phys D: Appl. Phys., Vol. 24**, pp. 41-47, (1991).

(16) Rakhimova, T.V., Kovalev, A.S., Rakhimov, A.T., Klopovsky, K.A., Lopaev, D.V., Mankelevich, Yu A., Proshina, O.V., Branginsky, O.V., and Vasilieva, A.N., *Radio-frequency plasma generation of singlet oxygen in O_2 and O_2:Ar(He) mixtures*, 34th AIAA plasmadynamics and lasers conference, **AIAA 2003-4306**, (2003).

(17) Braginskiy, O.V., Vasilieva, A.N., Kovalev, A.S., Lopaev, D.V., Mankelevich, Yu A., Rakhimova, T.V., and Rakhimov, A.T., *Singlet Oxygen Generation in O2 Flow Excited by RF Discharge: II. Inhomogeneous Discharge Mode: plasma jet*, **Journal of physics D: Applied Physics, 38**, p. 3609-3625, (2005).

(18) Gordiets, B., Ferreira, C.M., Guerra, V.L., Loureiro, JMAH, Nahorny, J., Pagnon, D., Touzeau, M., and Vialle, M., *Kinetic Model of a Low-Pressure N_2-O_2 Flowing Glow Discharge,* **IEEE Transactions on Plasma Science, 23,** 4, (1995).

(19) McDermott, W.E., Pchelkin, N.R., Benard, D.J., and Bousek, R.R., *An Electronic Transition Chemical Laser,* **Applied Physics Letters, 32**, (1978).

(20) Perram, Glen P., and Hager, Gordon D., *The Standard Chemical Oxygen-Iodine Laser Kinetics Package,* AF weapons laboratory report AFWL-TR-88-50, (1988).

(21) Gordiets, B., Ferreira, C.M., Nahorny, J., Pagnon, D., Touzeau, M., and Vialle, M., *Surface Kinetics of N and O atoms in N_2-O_2 Discharges,* **Journal of Physics D: Applied Physics, 29**, 1021-1031, (1996).

(22) Azyazov, V.N., Kabir, Md H, Antonov, I.O., and Heaven, M.C., *Kinetics of* $O_2(a^1\Delta_g)$ *and* $I(^2P_{1/2})$ *in the Photochemistry of* N_2O/I_2 *mixtures,* **Journal of Physical Chemistry A, 111**, pp. 6592-6599, (2007).

(23) Perram, G.P., *Approximate Analytic Solution for the dissociation of Molecular Iodine in the Presence of Singlet Oxygen,* **Int J Chem Kinetics, Vol. 27**, 817-828, (1995).

(24) Rawlins, W.T., Lee, S., Kessler, W.J., Oakes, D.B., Piper, L.G., and Davis, S.J., *Spectroscopic Studies of a Prototype Electrically Pumped COIL System*, **SPIE Paper: 5334-12**, SPIE Photonics West, 25-29 January, (2004).

(25) Wiley Encyclopedia of Electrical and Electronics Engineering, Vol. 3, John G. Webster ed., p. 280, (1999).

(26) Truesdell, K.A., Helms, C.A., Frerking, S., and Hager, G.D., **Proc. SPIE 3092**, 676, (1997).

(27) Hagelaar, GJM, and Pitchford, L.C., *Solving the Boltzmann Equation to Obtain Electron Transport Coefficients and Rate Coefficients for Fluid Models*, **Plasma Sources Science and Technology, Vol. 14**, pp. 722-733, (2005).

(28) Phelps, A.V., Technical Report 28, JILA information center, University of Colorado, Boulder, (1985).

(29) Atkinson et al., **J. Phys. Chem. Ref. Data, Vol. 26,** No. 3, (1997).

(30) Herron, J.T., and Green, D.S., **Plasma Chem. Plasma Process, 21**, 459, (2001).

(31) Ikezoe, Y., Matauoka, S., Takebe, M., and Viggian, A., *Gas Phase Ion-Molecule Reaction Rate Constants Through 1986* (Ion Reaction Research Group of the Mass Spectroscopy Society of Japan, Tokyo, 1987).

(32) Aleksandrov, N.L., Kindysheva, S.V., Kosarev, I.N., and Starikovski, A. Yu *Plasma decay in ar and N2:O2:CO2 mixtures at elevated gas temperatures.* **J. Phys. D: Appl. Phys. 41**, (2008).

(33) Sakiyama, Y., and Graves, D.B., *Corona-glow transition in the atmospheric pressure RF-excited plasma needle*, **J. Phys. D: Appl. Phys. 39**, (2006).

(34) Kokkoris, George, Goodyear, Andy, Cook Mike, and Evangelos, Gogolides, *A global model for C4F8 plasmas coupling gas phase and wall surface reaction kinetics*, **J. Phys. D: Appl. Phys. 41**, (2008).

(35) Brown, S.C., and MacDonald, A.D., *Limits for the diffusion theory of high frequency gas discharge breakdown,* **Physical Review, Vol. 76, No. 11**, (1949).

(36) Margenau, H., *Conduction and dispersion of ionized gases at high frequencies,* **Physical Review, Vol. 69, No. 9 and 10**, (1946).

(37) Herzberg, G., **Molecular Spectra and Molecular Structure Volume I : Spectra of Diatomic Molecules,** *Second Edition,* Krieger publishing company, Malabar, Florida, (1989).

(38) Pagnon, D., Amorim, J., Nahorny, J., Touzeau, M., and Vialle, M., *On the use of actinometry to measure the dissociation in O_2 DC glow discharges: determination of the wall recombination probability,* **Journal of Physics D: Applied Physics, 28**, pp. 1856-1868, (1995).

(39) Ivanov, V.V., Klopovsky, K.S., Lopaev, D.V., Rakhimov, A.T., and Rakhimova, T.V., *Experimetnaland theoretical investigation pf oxygen glow discharge structure at low pressures,* **IEEE Trans on Plasma Science, Vol. 27**, No. 5, October, (1999).

(40) Kays, W.M., and Crawford, M.E., Convective Heat and Mass Transfer, 2nd edition, McGraw-Hill Book Company, (1980).

(41) Walkup, R.E., Saenger, K.L., and Selwyn, G.S., *Studies of atomic oxygen in O2 + CF4 RF discharges by two-photon laser induced fluorescence and optical emission spectroscopy*, **Journal of Chemical Physics, 84**, 2668, (1986).

(42) Babic, D., Poberaj, I., and Mozetic, M., *Fiber optic catalytic probe for weakly ionized oxygen plasma characterization*, **Review of Scientific Instruments, 72**, No. 11, p. 4110, (2001).

(43) Bamford, Douglas J., Jusinski, Leonard E., and Bischel, William K., *Absolute two-photon and three-photon ionization cross sections for atomic oxygen,* **The American Physical Society**, (1986).

(44) Bischel, William K., Perry, Bryce E., and Crosely, David, *Detection of fluorescence from O and N atoms induced by two-photon absorption,* **Applied Optics, Vol. 21**, No. 8, 1419, (1982).

(45) Carruth, M.R., Jr., DeHaye, R.F., Norwood, J.K., and Whitaker, A.F., *Method for determination of neutral atomic oxygen flux*, **Review of Scientific Instrumentation, 61**(4), 1211, (1990).

(46) Dilecce, G., and Benedictis, S.De, *Experimental studies on elementary kinetics in N_2-O_2 pulsed discharges,* **Plasma Sources Sci Technol. 8,** pp. 266-278, (1999).

(47) Gomez, S., Steen, P.G., and Graham, W.G., *Atomic oxygen surface loss coefficient measurements in a capacitive/inductive radio-frequency plasma,* **Applied Physics Letters, 81**, No. 1, 9, (2002).

(48) Katsch, H.M., Tewes, A., Quandt, E., Goehlich, A., Kawetzki, T., and Dobele, H.F., *Detection of atomic oxygen: Improvement of actinometry and comparison with laser spectroscopy,* **Journal of Applied Physics**, **88** (11), p. 6232, (2000).

(49) Piper, Lawrence G., and Rawlins, Wilson T., *O-atom yields from microwave discharges in N_2O/Ar Mixtures*, **Journal of Physical Chemistry, Vol. 9**, No. 2, 320, (1986).

(50) Pope, Robert S., *Collisional Effects in the Absorption Spectra of the Oxygen a Band and Nitric Oxide Fundamental Band,* Air Force Institute of Technology, Dissertation, (1998).

(51) Poberaj, I., Mozetic, M., and Babic, D., *Comparison of fiber optics and standard nickel catalytic probes for the determination of neutral oxygen atoms concentration,* **Journal of Vacuum Science and Technology: A**, **20** (1), 189, (2002).

(52) Ricard, A., Monna, V., and Mozetic, M., *Production of O atoms in Ar-O_2 and N_2-O_2 microwave flowing post-discharges,* **Surface and Coatings Technology, 174-175**, pp. 905-908, (2003).

(53) Ricard, A., Gaillard, M., Monna, V., Vesel, A., and Mozetic, M., *Excited species in H_2, N_2, O_2 microwave flowing discharge and post-discharges,* **Surface and Coatings Technology, 142-144,** pp. 333-336, (2001).

(54) Soril, I., and Rocak, R., *Determination of atomic oxygen density with nickel catalytic probe,* **J. Vac. Sci. Tech. A. 18** (2), p. 338, (2000).

(55) Benavides, G.F., Zimmerman, J.W., Woodar, B.S., Carroll, D.L., Verdeyen, J.T., Field, T.H., Palla, A.D., and Solomon, W.C., *Gain and continuous-wave laser power enhancement with a secondary discharge to predissociate molecular iodine in an electric oxygen-iodine laser,* **Applied Physics Letters, 92**, 041116, (2008).

(56) Hill, AE, *Continuous uniform excitation of medium-pressure CO2 laser plasma by means of controlled avalanche ionization*, **Applied Physics Letters, 22**, p. 670, (1973).

(57) Hill. A.E., *The next generation of controlled avalanche discharge laser-including an extension to the electric oxygen iodine laser,* **Proceedings of the International Conference on LASERs**, (2000).

(58) Hicks, A., Norberg, S., Shawcross, P., Lempert, W.R., Rich, J.W., and Adamovich, I.V., *Singlet oxygen generation in a high pressure non-self-sustained electric discharge*, **Journal of Physics D: Applied Physics, 38**, pp. 3812-3824, (2005).

(59) Rawlins, W.T., Lee, S., Kessler, W.J., Oakes, D.B., Piper, L.G., and Davis, S.J., *Spectroscopic Studies of a Prototype Electrically Pumped COIL System*, **SPIE Paper: 5334-12**, SPIE Photonics West, 25-29 January, (2004).

(60) Itami Shin, Nakamura, Y., Nakamura, A., Shinagawa, K., Kihara, Y., Okamura, M., Yoshitani, E., and Fujii, H., *The Development of hybrid oxygen-iodine laser,* **SPIE Vol. 3889**, (2000).

(61) Napartovich, A.P., Deryugin, A.A., and Kochetov, I.V., *Discharge production of the singlet delta oxygen for an iodine laser,* **J Phys D: Appl Phys., 34**, pp. 1827-1833, (2001).

(62) Ionin, A.A., Klimachev, Yu M., Kotkov, A.A., Kochetov, I.V., Napartovich, A.P., Seleznev, L.V., Sinitsyn, D.V., and Hager, G.D., *Non-self-sustained electric discharge in oxygen gas mixtures: singlet delta oxygen production,* **J Phys D: Appl Phys. 36**, pp. 982-989, (2003).

(63) Savin, Yu V, Goryachev, L.V., Adamenkov, Yu A, Rakhimova, T.V., Mankelevich, YuA, Popov, N.A., Adamenkov, A.A., Egorov, V.V., Ilyin, S.P., Kolobyanin, YuV, Kudryashov, E.A., Rogozhnikov, G.S., and Vyskubenko, B.A., *Effective singlet oxygen generator on traveling microwave discharge*, 35th AIAA Plasmadynamics and Laser Conference, **AIAA 2004-2444**, (2004).

(64) Woodard, B.S, Benavides, G.F., Zimmerman, J.W., Carroll, D.L., Palla, A.D., Day, M.T., Verdeyen, J.T., and Solomon, W.C., *Enhancement of Electric Oxygen-Iodine Laser Performance using Larger Mode Volume Resonators,* **Optics Letters. 35**, 10, (2010).

(65) Heaven, M.C., *Recent Advances in the Development of Discharge-Pumped Oxygen-Iodine Lasers*, **Laser & Photonics Review**, (2010)

(66) Zimmerman, J.W., Woodard, B.S., Verdeyen, J.T., Carroll, D.L., Field, T.H., Benavides, G.F., and Solomon, W.C., *Influence of frequency on* $O2(a\,^1\Delta)$ *and oxygen atom production in transverse radio-frequency discharges,* **Journal of Physics D: Applied Physics, 41**, (2008).

(67) Davis, S.J., Lee, S., Oakes, D., Haney, J., Magill, J.C., Paulsen, D.A., Cataldi, P., Galbally-Kinney, K.L., Vu, D., Polex, J., Kessler, W.J., and Rawlins, W.T., *EOIL power scaling in a 1-5 kW supersonic discharge-flow reactor,* **Proc. of SPIE, 6874**, (2010).

(68) Lee, S. WT Rawlins, and SJ Davis. *Catalytically enhanced singlet oxygen for EOIL.* **Proc. of SPIE, 7196**. (2010).

(69) Azyazov, V.N., Mikheyev, P.A., Postell, D., and Heaven, M.C., *$O_2(a^1\Delta)$ Quenching in the $O/O_2/O_3$ System*, **International Symposium on High Power Laser Ablation**, (2010).

(70) Macko, P., and Veis, P., *Time resolved* $O_2\left(b,^1\Sigma_g^+\right)$ *rotational temperature measurements in a low-pressure oxygen pulsed discharge. Simple and quick method for temperature determination,* **J. Phys. D:Appl. Phys. 32,** pp. 246-250, (1998).

(71) Lange, M.A., Pitz, G.A., Smith, B., and Perram, G.P., *Electric discharge pumped oxygen-Iodine laser kinetics,* **Journal of Directed Energy, 1,** pp. 219-232, (2005).

(72) Perram, G.P., Determan, D.A., Dorian, J.A., Lowe, B.F., and Thompson, T.L., *Radial Diffusion Between Coaxial Cylinders and Surface Deactivation of $O_2(b\ ^1\Sigma_g)$*, **SPIE Vol. 1871 Intense Laser Beams and Applications**, p. 181, (1993).

(73) Perram, G.P., Determan, D.A., Dorian, J.A., Lowe, B.F., and Thompson, T.L., *Radial Diffusion Between Coaxial Cylinders and Surface Deactivation of $O_2(b\ ^1\Sigma_g)$*, **Chemical Physics**, **162**, pp. 427-432, (1992).

(74) Ionin, A.A., Kochetov, I.V., Napartovich, A.P., and Yuryshev, N.N., *Physics and engineering of singlet delta oxygen production in low-temperature plasma*, **J Phys A: Appl Phys, 40**, R25-R61, (2007).

(75) Babaeva, Natalia Y., Arakoni, R., and Kushner, M.J., *$O_2(a^1\Delta_g)$production in high pressure flowing He/O2 plasmas: Scaling and quenching,* **Journal of Applied Physics, 101**, 123306, (2007).

(76) Stoffels, E., Stoffels, W.W., Vender, D., Kando, M., Kroesen, GMW, and deHoog, F.J., *Negative ions in a radio-frequency oxygen plasma*, **Physical Review E, 51**, No. 3, (1995).

(77) Ivanov, V.V., Klopovskii, K.S., Lopaev, D.V., Rakhimov, A.T., and Rakhimova, T.V., *Nonlocal nature of the electron energy spectrum in a glow discharge in Pure O_2: II. Actinometry of $O(^3P)$ Atoms in a Plasma at Low Gas Pressures,* **Plasma Physics Reports**, **26** (11), pp. 980-990, (2000).

(78) Shamra, Surendra P., Cruden, B., and Bol'shakov, A.A., *Emission from Oxygen Plasma as a Sterilization Source: An Analysis,* 34th AIAA Plasmadynamics and Lasers Conference, 23-26 June, Orlando, FL, (2003).

(79) Arakoni, Ramesh A., Babaeva, Natalia Y., Kushner, Mark J., **2007 J. Phys. D: Appl. Phys. 40,** 4793.

(80) Doroshenko, V.M., Kudryavtsev, N.N., and Smetanin, V.V., 1992, *Khimiya. Visokikh Energii* **26,** 291.

(81) Braginskiy, O.V., Vasilieva, A.N., Klopovskiy, K.S., Kovalev, A.S., Lopaev, D.V., Proshina, O.V., Rakhimova, T.V., and Rakimova, A.T., *Singlet Oxygen Generation in O2 Flow Excited by RF Discharge: I. Homogeneous Discharge Mode: α-mode*, **Journal of physics D: Applied Physics**, **38**, pp. 3609-3625, (2005).

(82) Cengel, Yunus A., and Turner, Robert H., Fundamentals of Thermal-Fluid Sciences, Second Edition. McGraw-Hill Book Company, (2005).

(83) Laher, R.R., and Gilmore, F.R., *Updated Excitation and Ionization Cross-sections for Electron Impact on Atomic Oxygen*, **Physical Chemical Reference Data, 19**, No. 1, (1990).

(84) Yolles, R.S. and H. Wise, *Diffusion and Heterogeneous Reaction. X. Diffusion Coefficient Measurements of Atomic Oxygen through Various Gases*. **The Journal of Chemical Physics, 48**, No. 11, (1968)

(85) Wilke, C.R. and C.Y. Lee, *Estimation of Diffusion Coefficients fo Gases and Vapors*. **Industrial and Engineering Chemistry**. (1955)

(86) PeakFit, Systat software Inc., 1735 Technology Drive, Suite 430, San Jose, California, 95110, USA. Copyright 2011.

REPORT DOCUMENTATION PAGE

Form Approved
OMB No. 074-0188

1. REPORT DATE *(DD-MM-YYYY)* 22-12-11	**2. REPORT TYPE** Doctoral Dissertation	**3. DATES COVERED** *(From – To)* August 2001 – September 2011

4. TITLE AND SUBTITLE

KINETICS OF THE ELECTRICAL DISCHARGE PUMPED OXYGEN-IODINE LASER

5a. CONTRACT NUMBER

5b. GRANT NUMBER

5c. PROGRAM ELEMENT NUMBER

6. AUTHOR(S)

Lange, Matthew A.

5d. PROJECT NUMBER

5e. TASK NUMBER

5f. WORK UNIT NUMBER

7. PERFORMING ORGANIZATION NAMES(S) AND ADDRESS(S)

Air Force Institute of Technology
Graduate School of Engineering and Management (AFIT/EN)
2950 Hobson Way
WPAFB OH 45433-7765

8. PERFORMING ORGANIZATION REPORT NUMBER

AFIT/DS/ENP/11-S07

9. SPONSORING/MONITORING AGENCY NAME(S) AND ADDRESS(ES)

Air Force Office of Scientific Research
Dr Michael Berman
801 N. Randolh St. Room 732
Arlington, Virginia 22203

10. SPONSOR/MONITOR'S ACRONYM(S)

AFOSR/NL

11. SPONSOR/MONITOR'S REPORT NUMBER(S) 1-703-696-7797

12. DISTRIBUTION/AVAILABILITY STATEMENT

APPROVED FOR PUBLIC RELEASE; DISTRIBUTION UNLIMITED

13. SUPPLEMENTARY NOTES

This material is declared a work of the U.S. Government and is not subject to copyright protection in the United States.

14. ABSTRACT

A systematic study of microwave discharges at 2.45 GHz has been performed through the pressure range of sustainable electric discharges in pure oxygen flows of 2 to 10 Torr. A corresponding study of 13.56 MHz has also been performed at pressures of 2, 4, and 7 Torr. Optical emissions from $O_2(a\ ^1\Delta)$, $O_2(b\ ^1\Sigma)$, and O-atoms have been measured from the center of a μ-wave discharge. Discharge residence times from 0.1 to 5 ms have been reported. The $O_2(b\ ^1\Sigma)$ emissions, with a spectral resolution of 0.01 nm, have been used to measure the temperature of the gas, which typically reaches a steady-state of 1,200 K. The interpretation of the measured $O_2(a\ ^1\Delta)$, yield, using a streamlined, nearly analytic model, cast new light on the kinetics within the electric discharge. The pseudo-first order quenching rate of $O_2(a\ ^1\Delta)$ ranges from 6,000 s^{-1} for μ-wave discharges to 600 s^{-1} for radio frequency (RF) discharges, independent of gas pressure and flow rate. The observations are consistent with a second order reaction channel that is dependent on both the electron and oxygen ground state concentrations. The role of vibrationally excited ground state oxygen is explored and provides a plausible destruction mechanism.

15. SUBJECT TERMS

Discharge, Oxygen, Iodine, Laser, Spectroscopy, Kinetics, Gas Phase

16. SECURITY CLASSIFICATION OF:			**17. LIMITATION OF ABSTRACT**	**18. NUMBER OF PAGES**	**19a. NAME OF RESPONSIBLE PERSON**
a. REPORT	**b. ABSTRACT**	**c. THIS PAGE**			Perram, Glen P. ENP
U	U	U	UU	178	**19b. TELEPHONE NUMBER** *(Include area code)* 937-255-6565 x 4504

Standard Form 298 (Rev. 8-98)
Prescribed by ANSI Std. Z39-18